QUANTUM MECHANISMS OF DENSITY WAVE TRANSPORT

A Dissertation

Presented to

the Faculty of the Department of Physics

University of Houston

In Partial Fulfillment

of the Requirements for the Degree

Doctor of Philosophy

By

Asanga Iroshan Wijesinghe

December 2012

QUANTUM MECHANISMS OF DENSITY WAVE TRANSPORT

Asanga Iroshan Wijesinghe

APPROVED:

Prof. John H. Miller Jr., Chairman
Dept. of Physics

Prof. Gemunu Gunaratne
Dept. of Physics

Prof. Haibing Peng
Dept. of Physics

Prof. Arnold Guloy
Dept. of Chemistry

Prof. Jarek Wosik
Dept. of Electrical & Computer Engineering

Dean, College of Natural Sciences and Mathematics

Acknowledgements

First of all, I would like to express my gratitude to my research advisor, Professor John H. Miller Jr. for getting me started on this interesting research topic and being a wonderful guide throughout my graduate studies. His valuable advice, enthusiastic encouragement, support, experimental and theoretical experience, and also his many useful thoughts have been a great help to me to complete this thesis.

Next, I would like to express my thanks to Dr. Zhongjia Tang from the department of Chemistry for providing single crystals of $NbSe_3$. Without him none of my work would have been possible.

A special thank also goes to Professors Gemunu Gunarathne, Heibing Peng, Arnold Guloy, and Jarek Wosik for their valuable discussions while serving on my thesis committee.

I would also like to thank Dr. Kimal Rajapakshe, Sladjana Maric, Kalyan Sasmal, and Rooplekha Mitra in the HTS, Device application and Nano Biophysics labs for their help in the lab.

On a more personal note, I would like to thank my wife Nelka for her understanding and great support during my dissertation work.

Finally, I would like to thank my whole family and my wife's family for their persistent encouragement and love. Without their support I certainly not be where I am today.

QUANTUM MECHANISMS OF DENSITY WAVE TRANSPORT

An Abstract of a Dissertation

Presented to

the Faculty of the Department of Physics

University of Houston

In Partial Fulfillment

of the Requirements for the Degree

Doctor of Philosophy

By

Asanga Iroshan Wijesinghe

December 2012

Abstract

The non-linear properties observed in charge density wave compounds have been studied for many years. The quasi one-dimensional conductor $NbSe_3$ is particularly important because a small electric field can depin the charge density wave above a threshold field, above which the charge density wave shows non-linear behavior resembling Zener tunneling.

Transport properties of the one-dimensional linear chain compound $NbSe_3$ are measured using dc transport, ac response, pulsed techniques, direct mixing, and harmonic mixing as functions of dc bias voltage, applied frequencies, and in some cases the amplitude of an additional ac signal source.

A phenomenological model, consisting of a shunt resistance in parallel with a tunnel junction capacitor, based on the Hamiltonian tunneling matrix element, is presented as a possible mechanism for correctly describing charge density wave dynamics. Our results appear to be consistent with time-correlated quantum nucleation of solitons and antisolitons. Furthermore, mixing experiment results are also compared with photon-assisted tunneling theory. Numerical calculations obtained from the model accurately reproduce the observed features of charge density wave dynamics. The results reported here thus provide compelling evidence in favor of quantum tunneling as the mechanism for charge density wave depinning and transport.

Contents

List of Figures

List of Tables

Chapter 1

Introduction

Quantum tunneling refers to the quantum mechanical phenomenon where a particle can penetrate, and in most cases, pass through a potential barrier. This barrier is assumed to be higher than the kinetic energy of the particle; therefore, such a motion is not allowed by the laws of classical dynamics. Tunneling phenomenon is the most prominent manifestation of quantum mechanics, and its source lies in the probabilistic behavior imposed by quantum physics. At present, it is known that tunneling is a common phenomena in many area of physics including semiconductor physics, atomic physics, nuclear physics, and cosmology.

The tunneling effect has been traditionally treated by solving the time-independent Schrödinger equation in the continuum part of the spectrum, and then defining either transmission and reflection coefficients suitable for one-dimensional problems or a probability of escape (or penetration) per unit time in two- or three- dimensional situation [1]. The concept of quantum tunneling has undergone several important

advances since the 1960's. The tunneling Hamiltonian framework, originally proposed by Bardeen [2] and further developed by Cohen *et al.* [3], involves matrix elements in the transfer of particles between initial and final wave functions. The utility of the functional tunneling Hamiltonian becomes especially apparent since it permits putting potential energy information in the wave functionals and analyzing the kinetics of the evolution between initial and final wavefunctional states. The tunneling Hamiltonian is extensively used in explaining Josephson's theory of coherent tunneling of superconducting electron pairs through an insulating barrier [4].

Another advance occurred with publication of the now classic "Fate of the False Vacuum" papers [5, 6, 7], discussing quantum instability of a scalar field $\phi(r)$, of energy described by a double-well potential $U(\phi)$. If $\phi(r)$ sits in the higher metastable well ("false vacuum"), it is unstable to decay. This occurs when $\phi(r)$ tunnels into the lower potential well within a localized region of space, nucleating a bubble of "true vacuum" bounded by a domain wall separating it from the false vacuum. Variations of this model have been applied extensively to theories in quantum cosmology, including bubble nucleation of universes [8, 9], tunneling of branes [10], and even repeated tunneling of the universe, to explain the small, positive cosmological constant [11].

The false vacuum decay is a tunneling phenomena in quantum field theory, whose dynamic was first studied by Voloshin, Kovzarev, and Okun [12]. This was further advanced by introducing a method, to calculate the bubble nucleation rate and to describe the dynamics of a nucleated bubble, by Coleman [5], Callen, and Coleman [7]. In quantum field theory, the term "vacuum" refers to a local or global minimum

energy state and the scalar field ϕ has many interpretations, such as the Higgs or inflation field. Nucleation of bubbles in boiling water is, perhaps, the most well known example of thermal decay of the false vacuum. In this case, ϕ can represent the density of water, which is low for the vapor state (true vacuum when the temperature exceeds the boiling point T_b) and high for the liquid state (false vacuum when $T < T_b$). In the examples considered in this work, ϕ represents the phase of a density wave. Applying an external driving force (electric field) alters the potential energy landscape such that the initially lowest energy potential well becomes a metastable state (false vacuum) once the driving force exceeds a critical value. An elongated quasi-one-dimensional (1-D) "bubble of true vacuum," within which ϕ tunnels into the lower potential well, nucleates. The domain walls take the form of topological solitons (charge solitons) at the boundaries of the bubble.

The charge density wave (CDW) is an anisotropic (quasi-1-D) correlated electron-phonon system in which quantum interference between right- and left-moving electron states creates a charge modulation, $\rho(x,t) = \rho_0(x,t) + \rho_1 [\cos 2k_F x - \phi(x,t)]$, along the main axis of the whisker-like crystal. A spin density wave (SDW) is equivalent to two out-of-phase CDW's for the spin-up and spin-down subbands. Although pinned by impurities, a density wave can transport a current if the applied field exceeds a threshold field E_T. The system is described by a periodic pinning potential, idealized as a sine-Gordon potential, $1 - \cos\phi$ in the simplest model.

The interest in CDW's grew dramatically in 1976 when non-linear conductivity was first observed in the transition metal tricalcogenide $NbSe_3$ [13]. The non-linear dc conductivity was the first indication that the CDW could move through the lattice

and transport the charge. This was soon determined by electron, X-ray [14], and NMR [15] measurements, which strongly suggested that the observed nonlinearity was due to collective motion of the CDW. In addition to the non-linear conduction, it was later determined that CDW conduction occures only above a threshold electric field.

A variety of models have been proposed to describe the CDW or SDW dynamical response in the presence of defects. The first and simplest is the single impurity or rigid over-damped oscillator model [16], which describes the CDW as a single particle on a washboard potential. The single particle model can qualitatively predict several phenomena associated with CDW sliding. However, for a quantitative comparison with experimental data, the single particle model is, in most cases, an oversimplification.

A second and most widely studied model is the classical deformable model proposed by Fukuyama, Lee, and Rice [17, 18]. This model is an extension of the rigid model and it assumes that the CDW is an elastic medium that can adjust itself at impurity sites. Two regimes can be identified as the strong-pinning regime, and as the weak-pinning regime. The classification of CDW conductors into weak-pinning and strong-pinning materials has been the subject of intensive research and debate.

The Zener tunneling theory, proposed by John Bardeen [19] in 1979, is based on the experimental observation of a field-activated Zener form $J \approx [E-E_T]\exp(-E_0/E)$ of $NbSe_3$ and TaS_3 in the non-linear dc I-V characteristics. This model uses the small pinning gap in the collective excitation spectrum of the CDW system and invokes photon assisted tunneling to obtain the ac response.

Maki [20] considered a real-space picture, in which 2π-soliton-antisoliton (S-S$'$) pairs nucleate via quantum tunneling. In a related picture, Maiti and Miller [21] considered Zener tunneling of quantum solitons, which are heavily dressed, delocalized particles. Krive and Rozhavsky [22] pointed out the existence of a Coloumb blockade threshold field for the creation of charged S-S$'$ pairs, and later extended this picture to nucleation of soliton-like domain walls [23].

Despite the various successes and failures of each of these two classes of theories in predicting the exact details of various experimental results, they reproduced qualitative features of CDW conduction, threshold field, non-linear conduction, and ac response. In fact, many qualitative features of CDW dynamics seem to be generic to all these models, making it difficult to determine which model is the correct description for CDW transport.

One of the first experimentally observed quantum mechanical phenomena in CDW compounds is the oscillating magnetoresistance in $NbSe_3$, in the presence of small columnar defects, reported by Latyshev *et al.* [24]. The collective response of the CDW to the Aharonov-Bohm flux trapped inside the columnar defects reflected a $h/2e$ periodicity in CDW magneto-conductance. Very recent experiments on TaS_3 rings [25] also observed $h/2e$ oscillations in CDW magneto-conductance. These observations strongly demonstrate the quantum character of the CDW condensate. Moreover, the fact that the period is $h/2e$, rather than $h/2Ne$ as predicted [26] for N parallel chains, suggests that the system behaves as a quantum fluid rather than a

single massive object. Another important observation [27, 28, 29, 30] is that ac conductivity, dielectric response, and mixing are nearly bias-independent below threshold in $NbSe_3$ and TaS_3. These observations contradict classical predictions [31, 32, 33] of increasing or diverging dielectric response.

After several decades and large body of experimentation, theory, and speculation, CDW still continues to attract interest and generate controversy. In spite of that, there is still a debate whether classical mechanics is enough to describe the CDW properties or more advanced quantum mechanical treatment is needed. Recent experiments have shown in favour of quantum character in CDW transport.

The work described in this dissertation is an attempt to accurately explain the CDW transport phenomena using a quantum mechanical treatment. The CDW materials studied in this research are quasi-1-D $NbSe_3$ crystals due to their clean transport properties compared to other compounds. Dielectric, pulse, dc, ac, direct mixing, and harmonic mixing measurements, as functions of dc bias voltages, applied frequencies, and in some cases amplitudes of an additional ac signal source, are performed to characterize the CDW transport properties. A phenomenological quantum model consisting of a shunt resistance in parallel with a tunnel junction capacitor, based on the tunneling Hamiltonian matrix element, is presented as a possible mechanism for correctly describing charge density wave dynamics. Numerical calculations obtained from the model reproduce the observed features of CDW dynamics accuretly. Our results appear to be consistent with time correlated quantum nucleation of solitons and antisolitons. Furthermore, mixing experiment results are also compared with photon assisted tunneling theory. The results reported in this

dissertation thus provide compelling evidence in favour of quantum tunneling as the mechanism for charge density wave depining and transport.

1.1 Outline of the Dissertation

This dissertation is organized as follows.

Chapter 2 introduces background information, including a description, microscopic formation, and conduction mechanism of CDW. It also provides a description of the CDW material, $NbSe_3$.

Chapter 3 reviews the theoretical models that have been proposed to explain the CDW dynamics.

Chapter 4 contains the theoretical basis of the false vacuum theory for creation of soliton-antisoliton pairs. It also presents the phenomenological model as a possible mechanisms for correctly describing CDW dynamics. A comparison of theoritical and experimental results of pulse and current voltage responses are also included in this chapter.

Chapter 5 includes an overview of theoretical basis of the photon-assisted tunneling theory, applied to the CDW system. It also compares the mixing experiment results with photon-assisted tunneling theory.

Finally, Chapter 6 summarizes the results.

Chapter 2

Theoretical Background

2.1 Introduction

Metals may undergo a phase transition to a state exhibiting a new type of electronic order when cooling. For example, iron and nickel become ferromagnetic. In these materials, the exchange interaction causes an alignment of the spins of the conduction electrons, and an ordered state with a nonzero magnetic moment is formed. Other metals, such as aluminum and lead, become superconducting. In a superconductor, electrons of opposite momentum are coupled together into Cooper pairs as a result of their interaction with lattice vibrations. Such Cooper pairs can move through the superconductor without dissipation. A different type of phase transition called charge density wave (CDW) state occurs in a class of metals with a chain crystal structure, namely, quasi-one-dimensional materials, as a consequence of electron-phonon interactions. The resulting state consists of a periodic charge

density modulation accompanied by a periodic lattice distortion, both their periods being determined by the Fermi wave vector k_F. Consequently, both the electron and the phonon spectra are strongly modified by the formation of the CDW.

The purpose of this chapter is to introduce CDW's. CDW conducting materials have been researched extensively since their discovery in 1976 [13]. The interest in this field is due to the complex phenomena exhibited by these materials. A number of excellent reviews have appeared in the literature on this subject [30, 34, 35, 36]. An outline of those reviews is given below. Section 2.2 outlines the introduction about the CDW. Section 2.3 describes the formation of the CDW and section 2.4 explains the Fröhlich theory of CDW conduction. Finally, section 2.5 outlines the materials that show CDW conduction and the material properties that have been used in this work.

2.2 Charge Density Wave

Almost 50 years ago, Rudolph Peierls [37] and H. Fröhlich [38] independently suggested that a coupling of the electron and phonon systems in a one-dimensional metal is unstable with respect to a static lattice deformation of wavevector $Q = 2k_F$. CDW is a type of coupled electron-phonon instability found in quasi-low dimensional materials when cooled below a characteristic transition temperature, known as the Peierls temperature. Below the Peierls transition temperature (T_P), CDW in one-dimension can simply be described as a periodic distortion of a quasi-one-dimensional lattice, which is accompanied by a periodic modulation of the electron density. A spin

density wave (SDW) is closely related, and can be thought of as two CDW's for the spin-up and spin-down electrons that are 180^0 out-of-phase. Figure 2.1 illustrates a one-dimensional metal with lattice spacing a_0 distorted below the Peierls transition temperature T_P, introducing new periodicity $2a_0$, in to the lattice. In Fig. 2.1, wavelength of the modulated charge, λ_{CDW}, is four times the original lattice spacing a_0. In $NbSe_3$, λ_{CDW} is only approximately four times the lattice constant. In reality it is incomensurate with the lattice, such that $\lambda_{CDW} \neq na_0$ (n being an integer). This feature contributes to the fact that CDW's in this material tend to be very weakly pinned.

The modulation of the electron charge density depicted in Fig. 2.1 can be written as

$$\rho(x) = \rho_0 \cos(Q \cdot x + \phi(x)) \tag{2.1}$$

where ρ_0 is the amplitude of the modulated electron density, $Q = 2k_F$ is the wavevector of the modulation, k_F is the Fermi wavevector, $\phi(x)$ is the local phase of the modulation wave with respect to the lattice, and x is the distance along the one-dimensional chain. Similarly, The lattice distortion can be written as

$$u(x) = u_0 \cos(Q \cdot x + \phi(x)) \tag{2.2}$$

where u_0 is the amplitude of the lattice distortion with respect to the unperturbed ionic position. The distortions are usually quite small with atomic displacements about 1 % of the interatomic spacing and the conduction electron density varies by several percent [39].

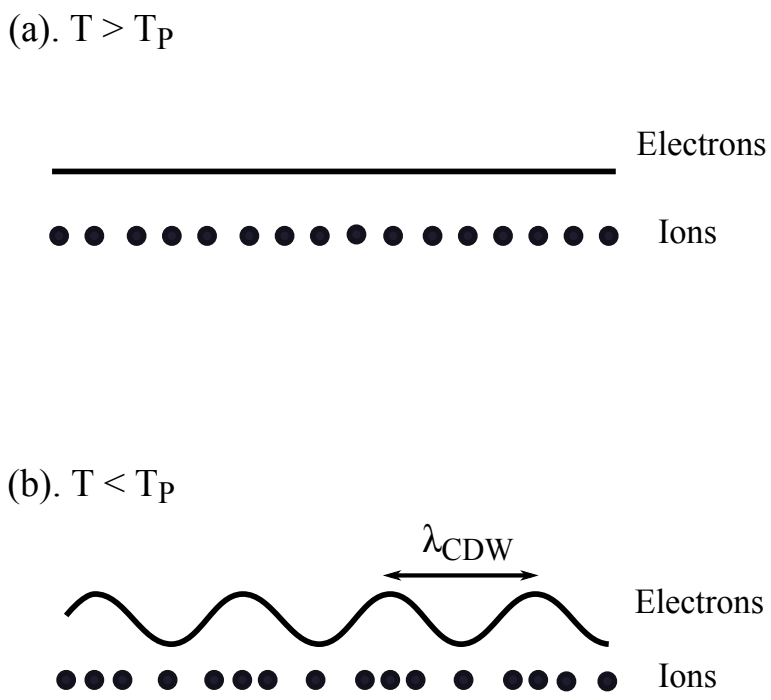

Figure 2.1: Formation of charge density wave (CDW) state in a one-dimensional metal. The dots represent the position of the metal ions and the solid lines represent the spatial variation of the charge density. (a) $T > T_P$ in the metallic state without the presence of CDW. The metal ions are evenly spaced and the electron charge density is uniform. (b) $T < T_P$ in the CDW state. The ions are displaced and electron density is periodically varying.

2.3 Charge Density Wave Formation

While CDW formation also occurs in materials with two- and three-dimensional band structure, it is predominantly a one-dimensional phenomena. The basic concept regarding the CDW formation was first proposed by Peierls in 1954 [37], where he considered a system of free electron gas coupled to the underlying lattice in one-dimension, and concluded that the system is not stable at low temperature, as it favors a new ground state displaying a static periodic lattice distortion and a modulation of the conduction electron density.

The key reason for the occurence of a CDW formation is the low dimensionality of the materials, where electron-phonon interactions, random pining potentials, and fluctuation effects are critical to the stability of the system.

2.3.1 Instability in a One-dimensional Electron Gas

The reduction of phase space from three-dimensions to one-dimension has several important consequences. Both interaction effects and random potentials have a more profound effect in one-dimension than in higher dimensions. Thermal fluctuations in the system are also very important. In order to understand the CDW formation, let's consider the response of a one-dimensional free electron gas to a time independent potential at zero temperature. The Fermi surface of the one-dimensional electron gas consists of two points, one at $+k_F$ and the other at $-k_F$, for an extremely anisotropic metal, two sheets, a distance of $2k_F$ apart. The particular topology of the Fermi surface leads to a response to an external perturbation, which is dramatically

different from that obtained in higher dimension. The response of an electron gas to the time independent potential $\phi(r)$,

$$\phi(r) = \int \phi(q) e^{iqr} dq, \tag{2.3}$$

is usually treated within the frame work of linear response theory. The rearrangement of the charge density, expressed in terms of an induced charge $\rho^{ind}(r)$,

$$\rho^{ind}(r) = \int \rho^{ind}(q) e^{iqr} dq, \tag{2.4}$$

is related to $\phi(r)$ expressed in the Fourier space,

$$\rho^{ind}(q) = \chi(q)\phi(q). \tag{2.5}$$

Here q is the wave vector and the proportionality $\chi(q)$ is the so-called Lindhard response function, which is given in d dimensions by,

$$\chi(q) = \int \frac{dk}{(2\pi)^d} \frac{f_k - f_{k+q}}{\epsilon_k - \epsilon_{k+q}}, \tag{2.6}$$

where $f_k = f(\epsilon_K)$ is the Fermi distribution function. For a one-dimensional Fermi electron gas at zero temperature, the particular topology of the Fermi surface leads to an electronic dispersion $\epsilon_k - \epsilon_F = \hbar\nu_F(k - k_F)$ where ϵ_F is the Fermi energy and ν_F is the Fermi velocity. The Lindhard response function is found to be

$$\chi(q) = -e^2 N(\epsilon_F) ln \left| \frac{q + 2k_F}{q - 2k_F} \right| \tag{2.7}$$

where $N(\epsilon_F)$ is the density of states at the Fermi level. The response function evaluated for all q values for a one-dimensional (1-D) metal is displayed in Fig. 2.2 together with that for the two-dimensional (2-D) and three-dimensional (3-D) electron gas.

In the 1-D case, the response function diverges at $q = 2k_F$, in 2-D, the first derivative exhibits a discontinuity at $2k_F$, while in a 3-D system, the response function is continuous even in the first derivative. It can be seen that the Lindhard response function dramatically depends on the dimensionality of the system.

The divergence of the Linhard response function at $q = 2k_F$ is due to particular topology of the Fermi surface. While Fermi surface of a free electron gas is a sphere in the 3-D case, it becomes a circle in 2-D and in the 1-D case, it consists only of two points at $+k_F$ and $-k_F$. This implies that a single wavevector $q = 2k_F$ pairs up all states on either side of the two parallel Fermi surfaces. Such a condition is usually called as "perfect nesting". Since all real materials are 3-D, the shape of the Fermi surface is of fundamental importance in determining whether $\chi(q)$ will diverge. A 3-D Fermi surface will still exhibit a 1-D character if the Fermi surface can be spanned or nested by the wavevector $Q = 2k_F$. Figure 2.3 illustrates the concept of a nested Fermi surface for a real quasi-1-D material along with one-, two-, and, three-dimensional electron gas.

The finite temperature dependence of the Linhard response function can be obtained using the Fermi function for $T \neq 0$ in Eqn. (2.6). At finite temperature the numerator gives,

$$\frac{1}{\exp(-\epsilon_k/k_BT)+1} - \frac{1}{\exp(\epsilon_k/k_BT)+1} = \tanh\frac{\epsilon_k}{2k_BT}. \tag{2.8}$$

Then, Eqn. (2.6) becomes

$$\chi(q = 2k_F, T) = -e^2N(\epsilon_F)\int_0^{\epsilon_0/2k_BT}\frac{\tanh x}{x}dx. \tag{2.9}$$

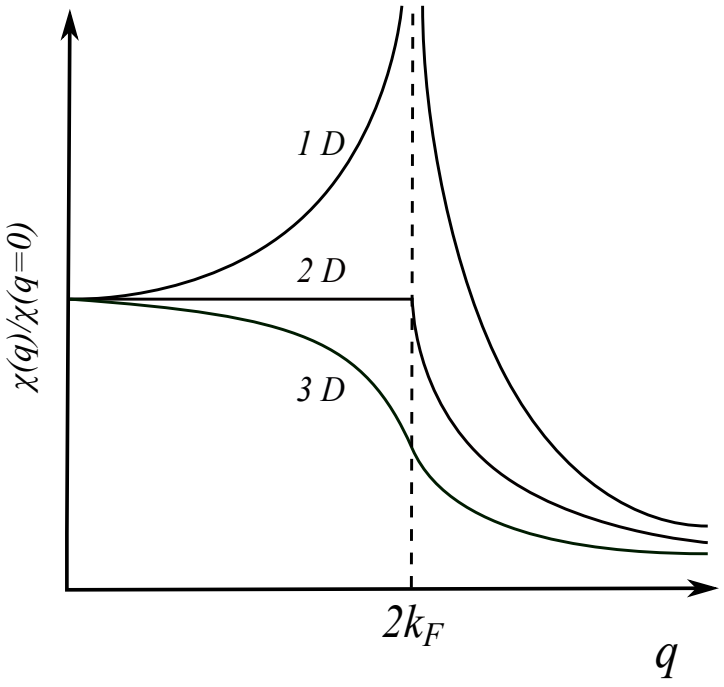

Figure 2.2: Lindhard response function for a one-dimensional (1-D), two-dimensional (2-D), and three-dimensional (3-D) free electron gas at zero temperature as a function of the wave vector q. The response function varies smoothly at $2k_F$ for a 3-D system. In 2-D, the first derivative exhibits a discontinuity at $2k_F$, while in a 1-D system, the response function diverges at $2k_F$.

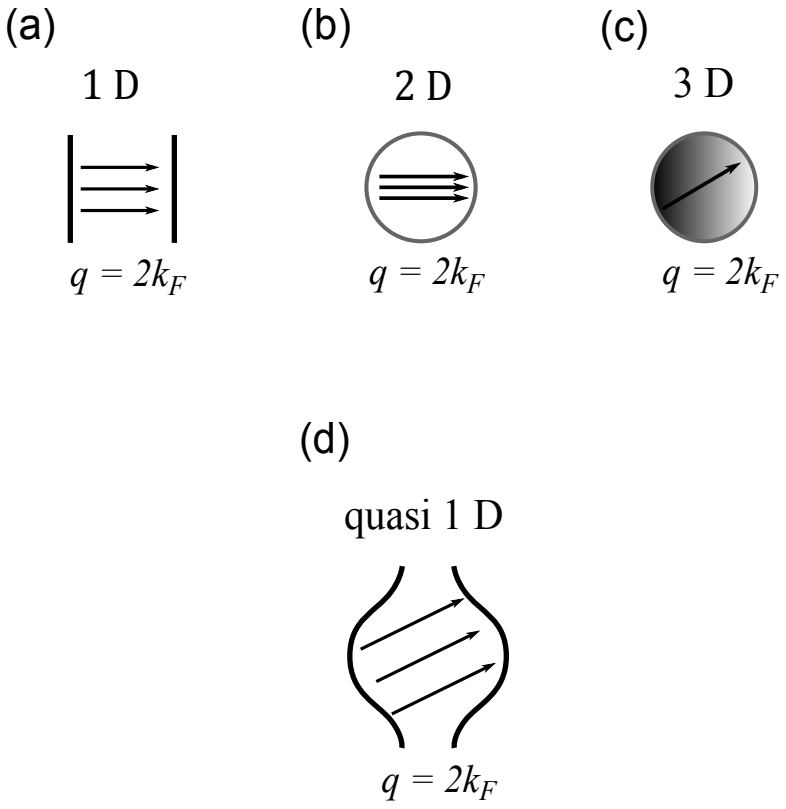

Figure 2.3: Fermi surface topology for one-, two-, three-, and quasi-one-dimensional free electron gas. The arrow indicates the wavevector. (a) Perfect nesting in 1-D electron gas. (b) Nesting in 2-D electron gas. (c) Nesting in 3-D electron gas. (d) Nesting in quasi-1-D free electron gas. Perfect nesting still exists for small dispersion in one direction.

The integral can be readily evaluated giving

$$\chi(q = 2k_F, T) = -e^2 N(\epsilon_F) ln \frac{1.14\epsilon_0}{k_B T}. \tag{2.10}$$

Here ϵ_0 is an arbitrary chosen cutoff energy which is usually taken to be equal to the Fermi energy ϵ_F. The temperature dependence of $\chi(2k_F)$ is approximated as $\chi(2k_F) \approx \ln(1/k_B T)$. This implies that $\chi(2k_F)$ diverges logarithmically with decreasing temperature.

2.3.2 Peierls Transition and Charge Density Wave Formation

In order to describe the transition to a charge density wave ground state, let's consider a one-dimensional electron gas coupled to the underlying chain of ions through electron-phonon coupling. This weakly coupled electron-phonon system can be described by the second quantized Hamiltonian [40] proposed by Fröhlich, which is given by,

$$H \;=\; H_{el} + H_{ph} + H_{el-ph} \tag{2.11}$$

where the first term

$$H_{el} = \sum_k \epsilon_k {a_k}^\dagger a_k \tag{2.12}$$

describes the Hamiltonian of the unperturbed electron gas, where ${a_k}^\dagger$ and a_k are the electron creation and annihilation operators for the electron states with energy ϵ_k. The second term

$$H_{ph} = \sum_q \hbar\omega_q {b_q}^\dagger b_q \tag{2.13}$$

describes the lattice vibration and ${b_q}^\dagger$ and b_q are the phonon creation and annihilation operators for the phonons characterized by the wavevector q, while ω_q represents the normal mode frequencies of the ionic mass. The third term

$$H_{el-ph} = \sum_{k,q} g_q {a_{(k+q)}}^\dagger a_k ({b_{-q}}^\dagger + b_q) \tag{2.14}$$

describes the electron-phonon interaction with coupling constant g_q.

In the case of a one-dimensional electron gas, the coupled electron-phonon system is unstable and this instability has fundamental consequences for both the lattice and the electron gas. The effect of electron-phonon interaction on the lattice vibrations can be described by establishing the equation of motion of the normal coordinates Q. For small amplitude displacements,

$$\ddot{Q}_q = -\left[{\omega_q}^2 - \frac{2g^2\omega_q}{\hbar}\chi(q,T)\right] Q_q. \tag{2.15}$$

The above equation of motion gives a renormalized phonon frequency

$$\omega_{ren,q}^2 = \omega_q^2 - \frac{2g^2\omega_q}{\hbar}\chi(q,T). \tag{2.16}$$

For a one-dimensional electron gas, the Lindhard susceptibility $\chi(q,T)$ has its maximum value at $q = 2k_F$. Consequently, the reduction, or softening of the phonon frequencies will be most significant at these wavevectors. This softening of the $2k_F$ phonon is called Kohn anomaly [41]. The phonon frequency for $q = 2k_F$ becomes

$$\omega_{ren,2k_F}^2 = \omega_{2k_F}^2 - \frac{2g^2 n(\epsilon_F)\omega_{2k_F}}{\hbar} ln\left(\frac{1.14\epsilon_0}{k_B T}\right). \tag{2.17}$$

With decreasing temperature, the renormalized phonon frequency goes to zero.

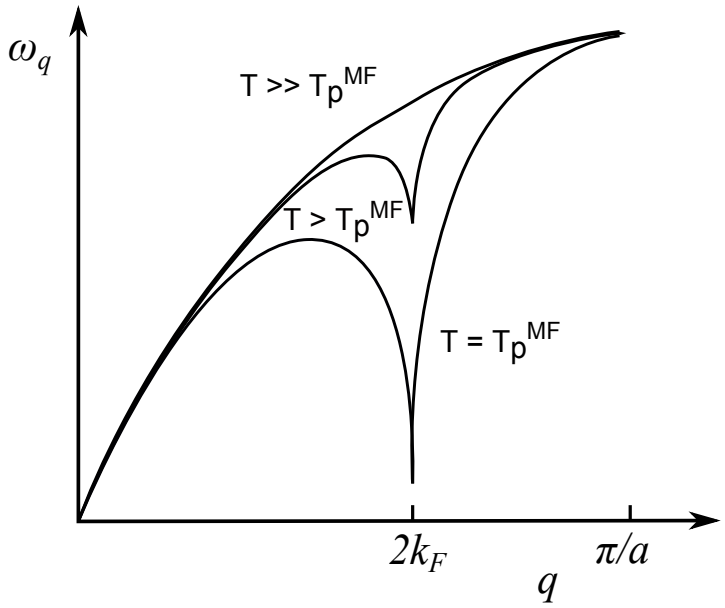

Figure 2.4: Phonon dispersion relation of a one-dimensional electron gas at various temperatures [36].

The temperature at which $\omega_{ren,q}$ becomes zero is called the Peierls transition temperature T_P^{MF}, and in the mean field approximation,

$$k_B T_P^{MF} = 1.14\epsilon_0 e{-}1/\lambda, \tag{2.18}$$

where $\lambda = 2g^2 n(\epsilon_F)/\hbar^2\omega_{2k_F}$ is the dimensionless electron-phonon coupling constant. This term describes the scattering of an electron by absorbing of a phonon of wavevector q or emission of a phonon of wavevector $-q$.

Below T_P^{MF}, $q = 2k_F$ becomes macroscopically occupied resulting in the static lattice distortion, and the mean lattice ionic displacement becomes

$$\langle u(x)\rangle = \Delta u \cos(2k_F x + \phi). \tag{2.19}$$

Here Δu is the amplitude of the lattice distortion and ϕ is the phase of the distortion with respect to the lattice.

$$\Delta u = \left(\frac{2\hbar}{NM\omega_{kF}}\frac{|\Delta|}{g}\right), \tag{2.20}$$

where N is the number of ionic lattice sites per unit length, M is the ionic mass, and Δ is the energy gap opened in the energy dispersion at the Fermi level. The modulation of the charge density in the ground state becomes

$$\rho(x) = \rho_0 + \rho_1 \ \cos(2k_F x + \phi) \tag{2.21}$$

where ρ_0 is the undistorted electronic density, and usually $\rho_1 << \rho_0$.

To summarize, for a one-dimensional metal with a linear chain separated by distance a_0, in the absence of electron-electron or electron-phonon interaction at T=0 K, the ground state corresponds to the situation depicts in Fig. 2.5(a): The electron

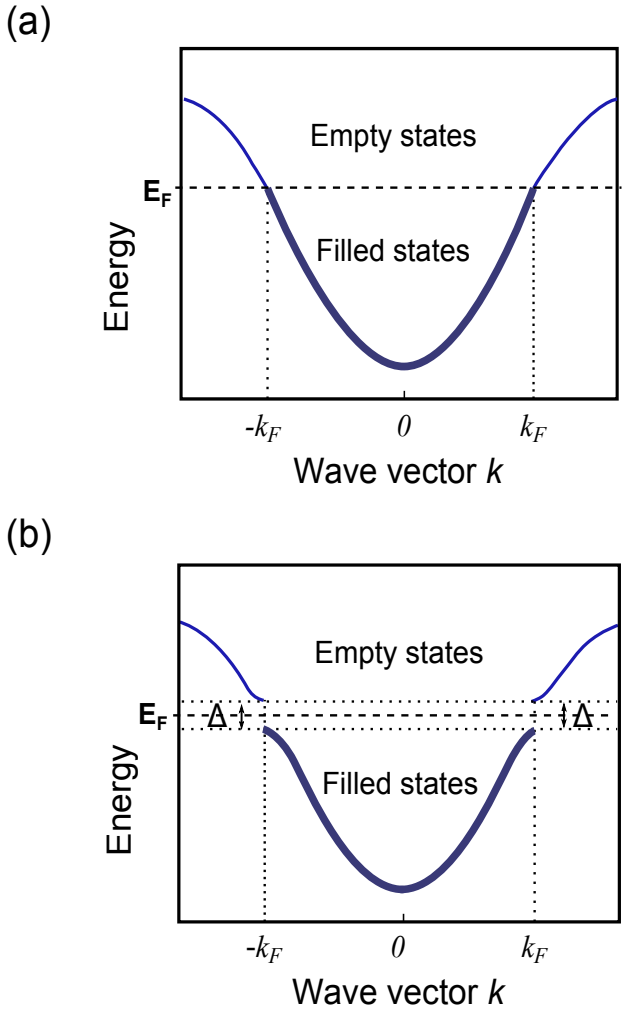

Figure 2.5: Peirerls distortion in a one-dimensional metal. One-electron states with energy $E(k) < E(k_F)$ are filled, while states with $E(k) > E(k_F)$ are empty. (a) Normal state (b) CDW state. In the band diagram, a gap Δ opens at the Fermi energy [36].

states are filled up to the Fermi level ϵ_F and the lattice is a periodic array of atoms with lattice constant a_0. In the presence of an electron-phonon interaction, it is energetically favorable to introduce periodic lattice distortion with period λ related to the Fermi wave vector $k_F\lambda = \pi/k_F$ to open up a gap at the Fermi level, as shown in Fig. 2.5(b). The energies of the occupied states below the Fermi energy ϵ_F are lowered, while the empty states are raised in energy. The gain in electronic energy is proportional to $u^2 \ln(u)$ for small lattice distortion u, while the cost of strain energy is proportional to u^2 [42]. Therefore, the total energy $u^2 ln(u) + u^2$ is decreased in the deformed state; hence, this deformed state is the preferred ground state.

At finite temperature, normal electrons excited across the energy gap screen the electron-phonon interaction. This, in turn, leads to the reduction of the gap and the magnitude of the lattice distortion, and eventually to a second-order phase transition at the Peierls temperature. The material is a metal above the transition temperature while it is a semiconductor below Peierls temperature with a temperature-dependent energy gap.

2.4 Charge Density Wave Conduction: Fröhlich Formalism

The Peierls instability leads to a periodic distortion of lattice and charge density in quasi-one-dimensional metals. Once the charge density waves are formed, the wavelength of the CDW is determined only by the Fermi wave vector, there is no direct relation between λ and a_0. If the ratio between the wavelength λ and lattice constant a_0 of the underlying lattice is a rational number, the CDW is commensurate with the underlying lattice and the CDW energy depends on its phase. On the other hand, when the ratio of the wavelength λ and lattice constant a_0 is an irrational number, the CDW is incommensurate and the CDW is translationally invariant with respect to the underlying lattice. Therefore, an incommensurate CDW state does not have a preferred ground state and ground state energy of the system would not change if the CDW is displaced.

In 1955, Fröhlich [38] demonstrated that the incommensurate CDW can slide through the lattice upon application of an infinitesimal electric field. Since the CDW carries charge collectively, it can contribute to electrical conductivity. Fröhlich proposed this as a possible mechanism for superconductivity. Instead, the CDW's are not superconductors, since the CDW is usually pinned to the lattice by impurities and defects. Therefore, contrary to the Fröhlich theory, the collective mode contribution to the electrical conductivity at low electric field is zero. However, if an moderate electric field is applied that is large enough to overcome the pining potential, the CDW is depinned from the underlying lattice and slides through the lattice. The

sliding of the CDW results in increase of conductivity. A typical example is shown in Fig. 2.6. Below a threshold voltage V_T, the I-V curve is linear, since the CDW is pinned and the current is due to thermally excited quasi-particles. CDW sliding starts in at V_T and the collective CDW motion causes a nonlinear I-V curve. This non-Ohmic behavior is a unique phenomena of CDW materials.

In the sliding state, the lattice ions oscillate back and forth to propagate the CDW condensate charge through the crystal, and the frequency of the macroscopically occupied $2k_F$ phonon condensate becomes nonzero, similar to the drift frequency ω_d of the CDW. The lattice distortion in the moving state is described by

$$u(t) = u_0 \cos\left[Qna - \omega_d t\right], \tag{2.22}$$

with the electron density modulation

$$\rho(x,t) = \rho_0 \cos\left[Qx - \omega_d t\right] \tag{2.23}$$

moving with a finite drift velocity $v_d = \omega_d/Q$, where $Q = 2k_F$.

Fröhich's original treatment was based on a one-dimensional free-electron gas model, and employed a variational calculation to determine the ground state of a coupled electron-phonon system with a fixed total momentum. Here, by following the tight binding approach of Allender, Bray, and Bardeen [43], the properties of the Fröhlich transport formalism can be calculated. For the moving lattice wave described by Eqn. (2.22), the corresponding macroscopic phonon modes can be described by,

$$\langle b_{\pm q} \rangle = \frac{U_0}{2} \left(\frac{1}{1 \mp V_d/s} \right) \exp\left(\mp i\omega_d t\right) \tag{2.24}$$

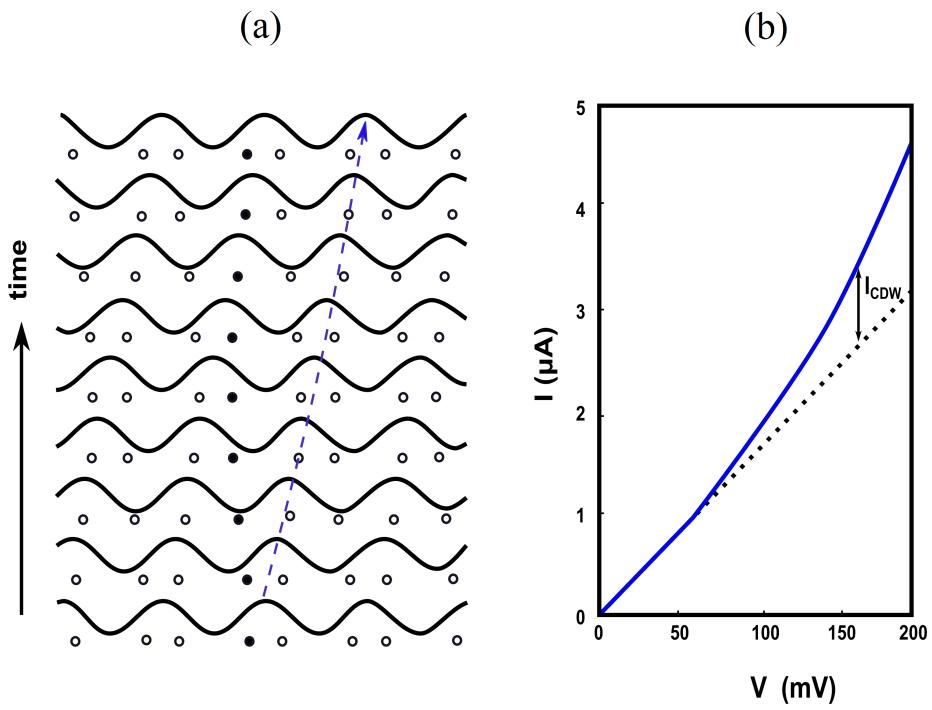

Figure 2.6: Sliding charge density waves (CDW) and current-voltage characteristics. (a) Sliding CDW in motion. Each snapshot corresponds to an advancement of the CDW by $\lambda_{CDW}/8$. (b) CDW sliding results in non-linear current-voltage characteristics [43].

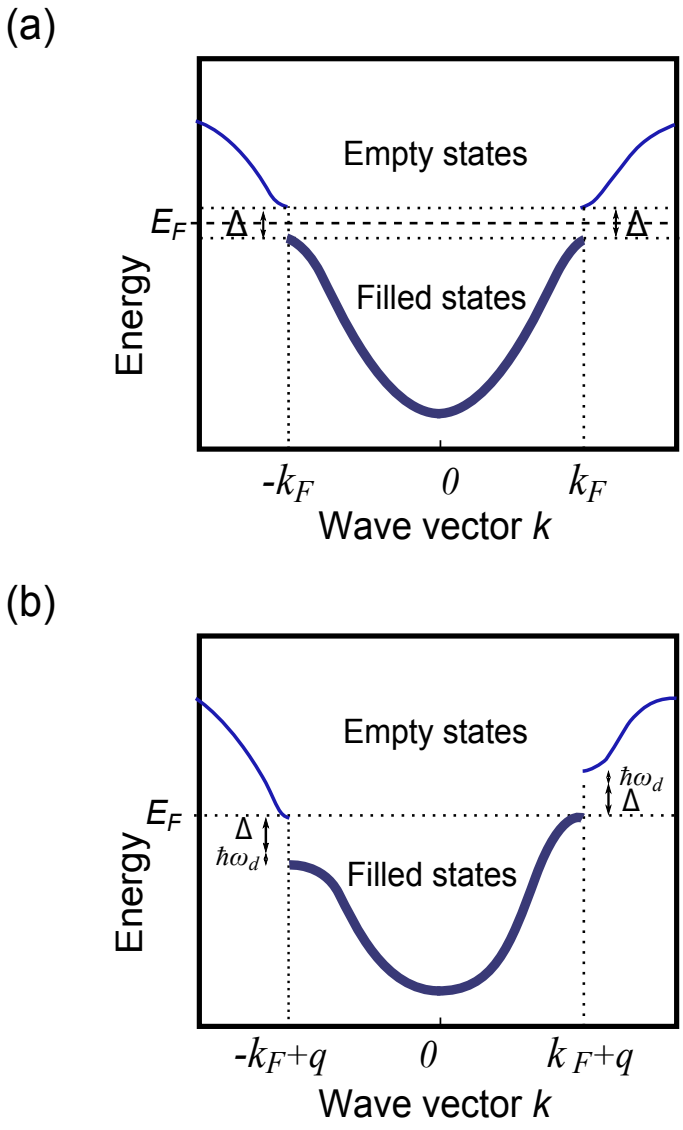

Figure 2.7: Half-filled tight band which has undergone Peierls transition. The Peierls energy gap Δ appears at the Fermi surface. (a) Stationary CDW with a drift velocity $V_d = 0$. (b) Moving CDW with a drift velocity $V_d > 0$ [44].

where $s = (m_b/3M)^{1/2} V_F$ is the sound velocity, V_F is the Fermi velocity, and $\omega_d = QV_d$ is the drift frequency. The energy gaps with the same magnitude are now displaced by wavevector $q = m_b V_d/\hbar$ with respect to their position in the stationary ground state, and by $\delta E = \hbar\omega_d$ in energy as shown in Fig. 2.7. In addition, the Bragg planes associated with the CDW distortion are now moving, so that the Bragg reflection involves a loss of both momentum and energy. The energy of the moving state is increased by the kinetic energy of the electron-ion system, $\frac{1}{2}N_{el}(m + M_F)V_d^2$, over that in the stationary state. The total momentum of the system is given by

$$\langle p \rangle = N_{el}\,(m + M_F)\,V_d, \tag{2.25}$$

which shows that, due to the strong electron and phonon with $2k_F$ coupling, the momentum mV_d per electron is enhanced by an effective lattice momentum $M_F V_d$. For a typical one-dimensional CDW material, the Fröhlich mass ratio M_F/m is generally estimated to be around $100 - 10^4$, so that the electron mass can be neglected in the above expression. The expectation value of the electric current carried by the ground state is

$$\langle J_{CDW} \rangle = -n_c(0) e V_d \tag{2.26}$$

where $n_c(0)$ is the condensed CDW carrier density at zero temperature.

The CDW current in the Fröhlich moving ground state is carried by a filled band and it results from collective motion of electron-phonon condensate. An applied electric field acts to transfer the system in to a new current carrying ground state. A moving CDW that carries an electric current represents the only other known mechanism of collective charge transport besides superconductivity.

2.5 Charge Density Wave Materials

Charge density wave formation in any material depends on the existence of a Fermi surface. Charge density waves do not form in electrically insulating materials, since they already have a band gap above the highest occupied electronic states. Consequently, materials exhibiting the Peierls transition are electrically conducting above their transition temperature.

A large number of organic and inorganic solids have crystal structures, in which the fundamental structural units form linear chains. Among the inorganic linear chain compounds are, for example, the platinum chain complex Krogmann's salt (KCP), the transition metal bronzes, such as $K_{0.3}MoO_3$ (blue bronze), and the transition metalchalcogenides such as $NbSe_3$ and TaS_3. While most of these materials are insulators or semiconductors, several groups have partially filled electron bands and consequently display metallic behavior at high temperature.

2.5.1 Niobium Triselenide: $NbSe_3$

All the experimental work described in this dissertation is carried out on niobium triselenide ($NbSe_3$), which is one of the most widely studied CDW material. $NbSe_3$ lends itself well to transport experiments, since high purity crystals can be grown and its CDW transport properties are very clean compared to those of other compounds.

The quasi-one-dimensional conductor, $NbSe_3$ is a representative of the family of transition metal trichalcogenides with the general formula MX_3, where M = Nb or

Ta and X = chalcogen (S or Se) [36]. The materials belonging to this group are strongly anisotropic three-dimensional conductors that consist of conducting chains weakly coupled by Van de Walls forces [45].

$NbSe_3$ is probably the most widely studied charge density wave material. It was first synthesized by chemical vapor deposition at 700^o C by Meerschaut and J. Rouxel in 1975 [46]. $NbSe_3$ crystals grow as needle-shaped whiskers with several millimeters long, somewhat flexible along the needle axis, and with a typical cross-section of 50 μm^2. The crystal structure, shown in Fig. 2.8(a), consists of chains along the b - axis of trigonal prism of Se with transition metal approximately at the center of each chalcogen prism. The chains are linked in the c - direction by interchain Nb-Se bonds, with lattice parameters, a = 10.09 Å, b = 3.481 Å, c = 15.629 Å, and β = 109.47 Å [47]. These chains are parallel to the crystallographic b - axis.

Figure 2.8(b) shows a projection of the crystal structure perpendicular to the b - axis. The unit cell of $NbSe_3$ is monoclinic and contains six chains divided in to three types, I, II and III. These three types can be distinguished by the strength of the outer Se-Se bonds and the spacing between Se atoms in each prism.

$NbSe_3$ is metallic at room temperature with resistivity of about 0.2 $m\Omega cm$ along the chain direction [48]. It stays metallic at low temperatures, since part of the Fermi surface remain ungapped. $NbSe_3$ is not highly anisotropic. Therefore, perpendicular to the b - axis, the room temperature resistivity of $NbSe_3$ is 10 times lower. Upon cooling, $NbSe_3$ undergoes two Peierls transitions to CDW state [14]. The first transition occurs at T_{P1} = 145 K, which corresponds to the formation of an incommensurate CDW and associates with the chain III (which has the closest

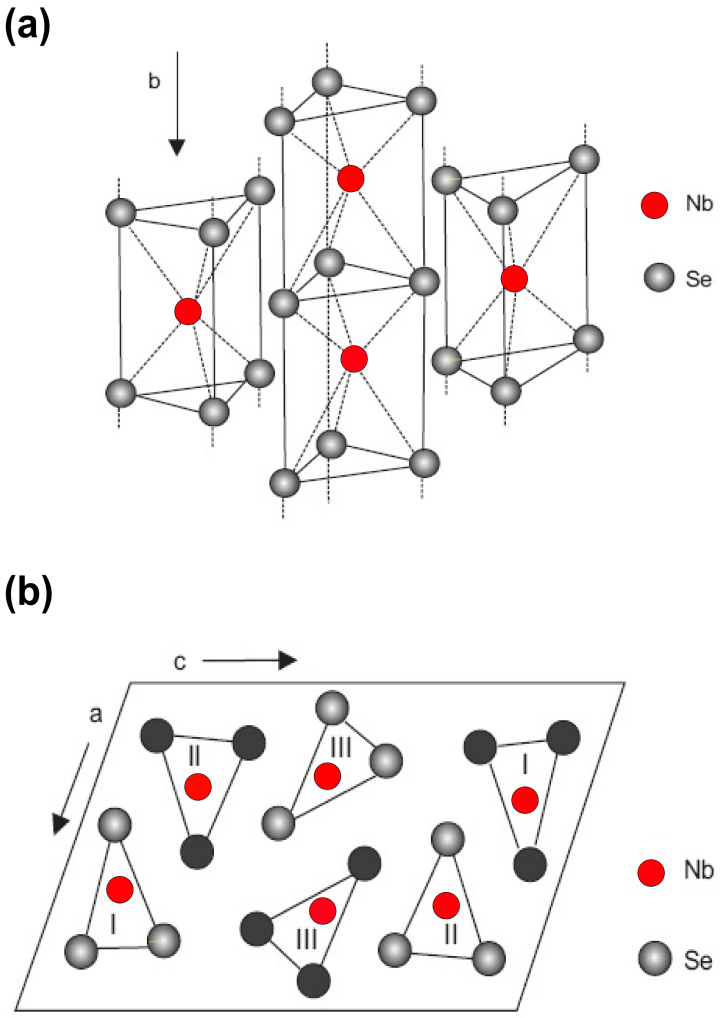

Figure 2.8: Schematic representation of the $NbSe_3$ structure in space. The unit cell consists of six chains of three different types I, II, and III [46].

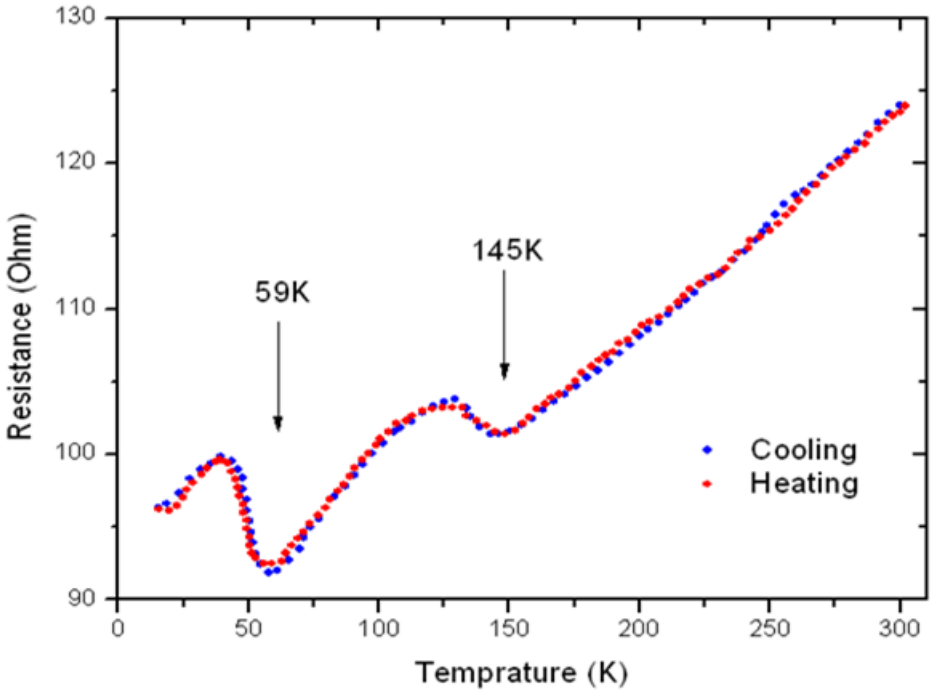

Figure 2.9: Temperature dependence of the resistivity of $NbSe_3$ along chain direction. Data obtained by cooling (blue circles) and heating (red circles) coincide. The resistivity anomalies at 145 K and 59 K are associated with two independent Peierls transitions. Below the second Peierls transition, $NbSe_3$ remains metallic due to an incomplete nesting of the Fermi surface.

chalcogen spacing). The second transition occurs at $T_{P2} = 59$ K, which results in an incommensurate CDW and associates with the type I (chain I which has intermediate chalcogen spacing). Chain II has the largest chalcogen spacing and does not form charge density waves. These two independent transitions are marked in the resistivity as a function of temperature by two anomalies as shown in Fig. 2.9. $NbSe_3$ is an unconventional CDW conductor in which part of the Fermi surface remains ungapped below the transition temperatures. As a result, the material remains metallic at all the temperatures.

Chapter 3

Theoretical Models

3.1 Introduction

Charge density waves were known to exist in the early 1970's in quasi-one-dimensional conductors such as TTF-TCNQ and potassium cyanoplatinate (KCP), as well as in quasi-two-dimensional materials such as TaS_2 and $NbSe_2$. The interest in charge density waves grew dramatically in 1976, when non-linear conductivity was first observed in the transition metal trichalcogenide $NbSe_3$ [13]. Since then, a fairly large number of materials have been discovered, and most of the research work has done on potassium blue bronze $K_{0.3}MoO_3$, trichalcogenide orthorombic-TaS_3, halogen-transition metaltetrachalcogenide $(TaSe_4)_2I$ materials and much of the work on $NbSe_3$. The single feature these various materials have in common is the one-dimensional character of the band structure that corresponds to the anisotropic properties in conductivity.

The non-linear dc conductivity was the first indication that the CDW could move through the lattice and transport the charge. It was soon determined by electron and X-ray [14] measurements, which strongly suggested that the observed nonlinearity was due to collective motion of the CDW. In addition to the non-linear nature of the CDW conduction, it was determined that CDW conduction occurred only above a threshold electric field and the current oscillations with a well-defined frequency spectrum appeared in the sliding state [49]. In the sliding state (above the threshold field), the dc conductivity $\rho = J/E$ increases with increasing field and obeys a slightly modified Zener tunneling form until it saturates at high field [50]. A frequency-dependent ac conductivity observed at MHz frequencies along with a very large dielectric constant $(10^8 - 10^9)$ [51], indicates a collective response with its associated strong polarizability. ac-dc interferences are another effect observed in a moving CDW due to characteristic periodicity [52]. Finally, metastability and memory effect in the CDW response have also been observed in a wide variety of transport measurements [53].

3.2 Theoretical Models

Two different classes of theories based on classical and quantum phenomena, have been proposed to describe CDW response in the presence of defects. The most notable models include classical rigid model and classical deformable model based on classical phenomena and quantum tunneling model based on quantum phenomena. All these models neglect variation in the CDW's amplitude and consider only the dynamics of the phase. In each case, the CDW is modeled as moving in a periodic potential that represents the pinning by impurities.

3.2.1 Classical Rigid Model

The simplest model to describe the charge density wave transport is the classical rigid model. It is also referred to as the single impurity model or the rigid overdamped oscillator model. In 1981, Grüner, Zawadowski, and Chaikin [16] proposed this purely phenomenological description of CDW motion. A similar model was considered by Monceau, Richard, and Renard in 1982 [48]. This model assumes that the CDW is perfectly ordered and has a single degree of freedom: the CDW phase. This assumes that the charge density wave amplitude is constant in both time and space, that the wave does not stretch or compress as it moves, and that the electric field is directly couples to the macroscopic phase of the CDW.

In the presence of impurities, this model treats the CDW condensate as a rigid overdamped object in a periodic pinning potential called washboard potential. The pinning potential is caused by the overall effect of the impurities and it's periodicity

is equal to the CDW wavelength. The simplest periodic pinning potential $U(x)$ is modeled as

$$U(x) = \frac{m^* w_o^2}{4k_F} \sin(2k_F x), \tag{3.1}$$

where m^* is the effective mass, w_o is the characteristic pinning frequency and x is the position of the particle. The driving force of the CDW is the applied electric field and it is damped by interactions with quasi particles. Therefore, that the equation of motion for the position of the CDW phase ϕ in an electric field E is taken to be

$$\ddot{\phi} + \frac{1}{\tau}\phi + \omega_o^2 \sin\phi = \frac{eQ}{M_F} E(t) \tag{3.2}$$

where τ is the damping constant and M_F is the effective mass of the CDW. It is expected that M_F is much larger than the electron mass, because the lattice distortion must move with the CDW.

An external voltage applied to the system corresponds to a force E on the particle. The electric field effectively tilt the washboard potential. For small fields, the particle remains in a trench and the CDW is pinned. Above a threshold field, E_T, the tilt is big enough to get the particle out of the trench. Then, the CDW slides through the potential as it rolls down the staircase as shown in Fig. 3.1.

The dc threshold field E_T is calculated to be

$$E_T = \frac{M_F w_o^2 \lambda_{cdw}}{2\pi e}, \tag{3.3}$$

while the dc conductance $\sigma_{dc}(E)$ is calculated as

$$\sigma_{dc}(E) = \begin{cases} 0 & \text{for} \quad E < E_T \\ \sigma_b \left(1 - \frac{E_T}{E}^2\right)^2 & \text{for} \quad E > E_T. \end{cases} \tag{3.4}$$

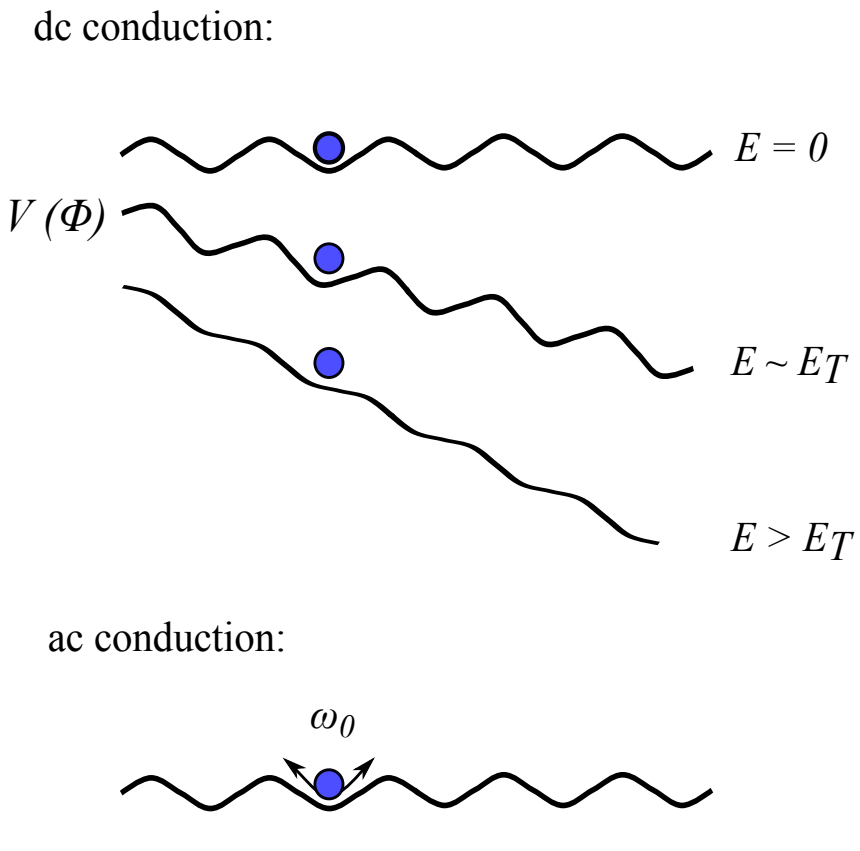

Figure 3.1: Classical single particle model of density wave transport. CDW is described as a rigid object (that oscillates with frequency w_o) moving in a sinusoidal periodic potential [36].

Here $\sigma_b = \frac{n_e e^2 \tau}{M_F}$ is the maximum conductivity obtainable for the CDW at high fields. For small fields, this model predicts an ac conductivity $\sigma(w)$, by making the approximation $\sin\phi \sim \phi$,

$$\sigma(\omega) = \sigma_b \frac{i\omega/\tau}{(\omega_p^2 - \omega^2) + i\omega\tau}. \tag{3.5}$$

This approach qualitatively predicts much of the observed CDW phenomena. It predicts a sharp depinnig transition at a threshold field E_T. Also, this model predicts that the motion of the CDW will be modulated by the washboard, and hence, this model reproduces the narrow band "noise" spectrum, coherent oscillations, and interference effects [54]. Most importantly, this model of CDW provides a simple picture that helps in visualizing how a rigid CDW, interacting with impurities, would behave.

The model of a rigid CDW, pinned by a single impurity, is not a good description of a system with many randomly distributed impurities resulting in a distribution of pinning frequencies and other parameters. The flow to the rigid model is its negligence of internal degree of freedom and random pinning. Indeed, the rigid overdamped oscillator model provides a poor qualitative comparison to experiments.

3.2.2 Classical Deformable Model

The most widely studied model of charge density wave transport is the classical deformable model. This model, a vast improvement over the classical rigid model description of the CDW dynamics, is also named as FLR model. The classical deformable model is developed by Hidetashi Fukuyama, Patrik Lee, and T. Maurice Rice [17, 18] and later, extended by Snedon, Cross, and Fisher [55].

The deformable model treats CDW as a charged elastic medium that can deform around the impurities, and thus incorporate an infinite number of internal degrees of freedom. The phenomenological Hamiltonian, also known as the FLR Hamiltonian, for the deformable model of the CDW state can be written as

$$H = \frac{1}{2}\int k\frac{d\phi}{dx}^2 dx - (E)\int \phi(x)dx + \sum_i V_i(x - R_i) \tag{3.6}$$

where k is the elastic constant of the phase mode, $V(x - R_i)$ is the electric potential at x due to the i^{th} impurity at position R_i, and E is the externally applied driving electric field. The position of the impurity as well as their strength $V(R_i)$ are assumed to be random.

The first and the third term in Eqn. (3.6) are introduced by Fukuyama, Lee, and Rice. The first term represents the elastic energy of the CDW system while the third term describes the interaction energy of the CDW system, with impurities located at random positions. The second term, which is introduced by Shedon, Cross, and Fisher, describes the polarization energy of the CDW in a uniform applied electric field E.

CDW motion is possible when the applied force is large enough to overcome a

threshold value, which results from the balancing of elastic and impurity pinning energy. The deformable model distinguishes two regimes; strong and weak pinning.

In the strong pinning regime, the impurity pinning force is larger than the elastic force in the CDW. The CDW phase is fully adjusted at each impurity. In the weak pinning regime, the elastic force is larger than the impurity pinning force. The CDW phase is adjusted to many randomly distributed impurity sites with a length scale over which the phase varies by a wave length. This length scale is known as the phase coherence length l_ϕ. l_ϕ depends on the impurity concentration and the pinning properties of the type of impurity.

Many aspects of CDW phenomena have been successfully described in the context of this model, reproducing the behavior of the classical rigid model, and also including effects due to the internal dynamics of the CDW. However, a complete description of CDW dynamics faces some difficulties. Many features of these theories do not depend on how the CDW is actually accelerated by an electric field, so that they may prove useful in describing how the CDW deform during the motion. This model also predicts that the high-field dc conductivity has the form $a - bE^{-1/2}$, where a and b are constants [55]. This prediction is contradicted by experiments [56] that show substantial departure from the classically predicted behavior, but essentially perfect agreement with the Zener form $\exp(E_0/E)$, in the high field limit.

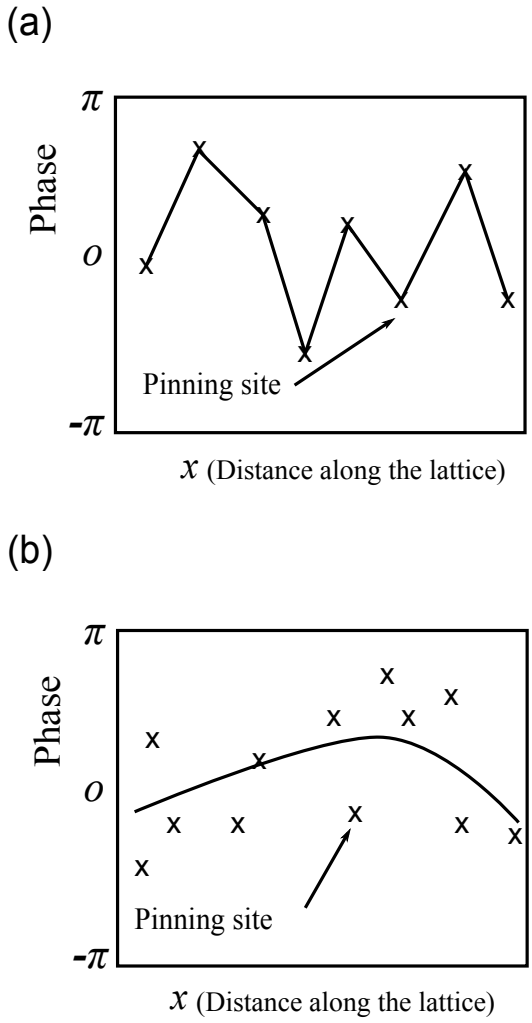

Figure 3.2: Illustration of (a) Strong and (b) Weak pinning of the charge density wave (CDW) phase in one-dimension. The cross ($\times$) represents the randomly distributed impurity pining sites while the solid line represents the distorted CDW phase ϕ.

3.2.3 Quantum Tunneling Model

In a very different approach, John Bardeen [19] has suggested that quantum effects are essential in describing the dynamics of the CDW transport. While all of the above classical models treat the phase of the CDW condensate as a classical variable, he assumed that the Zener type tunneling processes are responsible for the advancement of the average phase of the CDW condensate. Tunneling is first treated as advancement of the CDW phase by Maki [57]. Bardeen's model relies heavily on phase coherence between the neighboring chains. The model starts with the Fukuyama-Lee-Rice theory and sets periodic pinning forces at distance L_o apart. This gives the position dependent phase as shown in Fig. 3.3(a). Two degenerate solutions are possible for this particular pinning,

$$\phi_A = \frac{\pi}{2}\sin\frac{\pi x}{L_o} \qquad and \qquad \phi_B = -\pi - \frac{\pi}{2}\sin\frac{\pi x}{L_o}. \tag{3.7}$$

In the presence of an electric field, a CDW in state ϕ_A will move from its optimal position at an average rate $-v_d t$. The CDW current is determined by the transition rate between the two states. When the spatial average position is $\pi/2$, ϕ_A and ϕ_B are equivalent in energy, but separated by an energy barrier. At phases $\phi > \pi/2$, ϕ_B is favorable. The effective pinning potential $V(\theta)$ can be written as

$$V(\theta) \sim \begin{cases} -\cos\theta & \text{for} \quad \frac{-\pi}{2} < \theta < \frac{\pi}{2} \\ \cos\theta & \text{for} \quad \frac{\pi}{2} < \theta < \frac{3\pi}{2}. \end{cases} \tag{3.8}$$

This small periodic potential leads to a small pinning energy gap across which the CDW is excited by the electric field. The energy gap E_g is given by

$$E_g = \frac{2}{\pi}\left[\frac{m^*}{m}\right]^{\frac{1}{2}} \pi\omega_p, \tag{3.9}$$

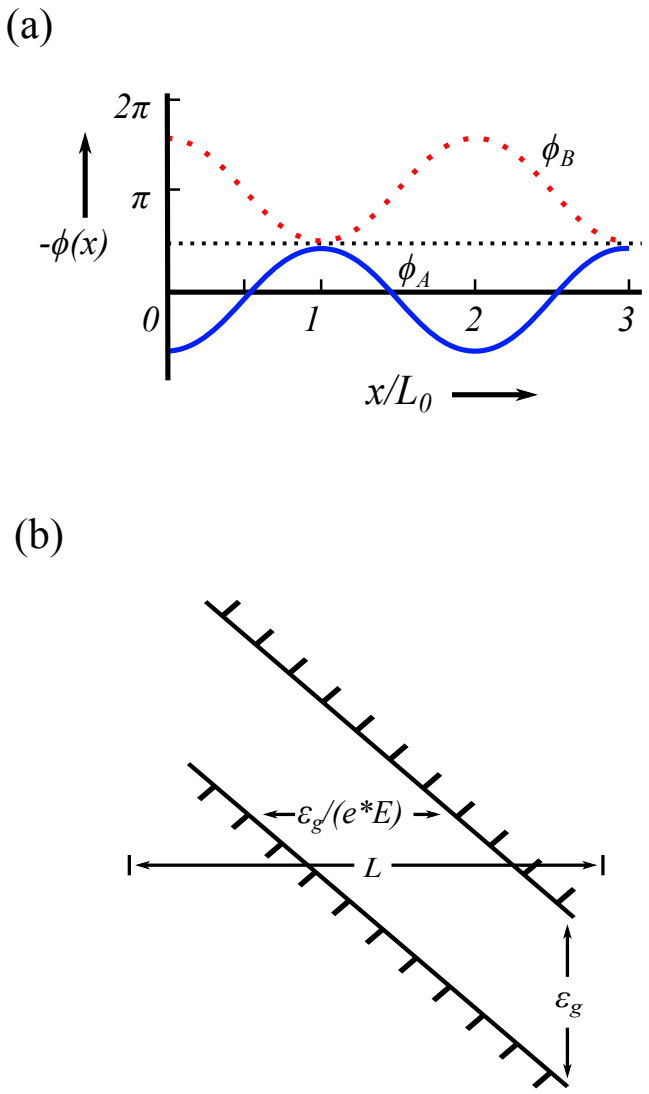

Figure 3.3: (a) Phase variation of the CDW. The two states ϕ_A and ϕ_B in the tunneling model [58]. (b) Zener diagram for tunneling of CDW electrons across the pinning gap. The bands representing Bloch states are tilted by the the electric field E [19].

with $\omega_p = \pi C_p/L_0$, where C_p is the phason velocity and m^* is the effective mass. The non-linear conduction $\sigma(E)$ has the typical tunneling form,

$$\sigma(E) = \sigma_\infty \left[1 - \frac{E_T}{E}\right] \exp\left(-\frac{E}{E_o}\right) \tag{3.10}$$

with $E_o = \frac{m^*}{m}\frac{\pi^2\omega_p^2}{V_F e}$, similar to the equation for the single particle tunneling. Figure 3.3(b) shows the Zener diagram for tunneling of CDW electrons across the pinning gap ϵ_g. If L represents a maximum distance within which the condensed electrons can tunnel, then tunneling occurs only when $e^*EL > \epsilon_g$.

The model does not treat the low frequency fluctuations that are assumed to be decoupled for the tunneling that occurs at high frequencies, and also it does not treat the polarization effects that are important for processes below threshold.

3.3 Literature Review: Quantum vs. Classical Models

A long standing debate concerns whether a classical description is sufficient to describe density wave depinning, or a quantum treatment is required. The pivotal CDW transport experiment on $NbSe_3$ [13] revealed a behavior of the form $J_{CDW} \sim E \exp[-E_0/E]$, where E_0 proved far too small to represent Zener tunneling of normal electrons across the Peierls gap. This observation motivated Bardeen [59] to propose a coherent Zener tunneling of condensed CDW electrons through a tiny "pinning gap" fixed at $\pm k_F$ by impurity scattering. Maki derived a similar J vs. E relation based on soliton pair creation [20]. Later experiments showed a threshold field E_T, for which Bardeen proposed [19] a maximum tunneling distance and modified Zener form, $J_{CDW} \propto (E - E_T) \exp[-E_0/E]$, seen in many $NbSe_3$ (Fig. 3.4(a)) and TaS_3 samples [60].

Earlier experiments have shown that, in $NbSe_3$ and TaS_3, the CDW displaces very little below the threshold electric field for CDW transport. This is evident in NMR experiments [15] showing a 2^0 CDW phase displacement in $NbSe_3$, as compared to the classically predicted 90^0 displacement below threshold. Further evidence provided by dielectric response and other ac responses including frequency mixing [27, 28, 29, 30] exhibits nearly bias-independent response below threshold. These flat ac responses are consistent with observed small phase displacements [15] and contradict classical predictions [31, 32, 33] of increasing or divergent dielectric response shown in Fig. 3.4(b). Thus, even near threshold, the phase appears to sit

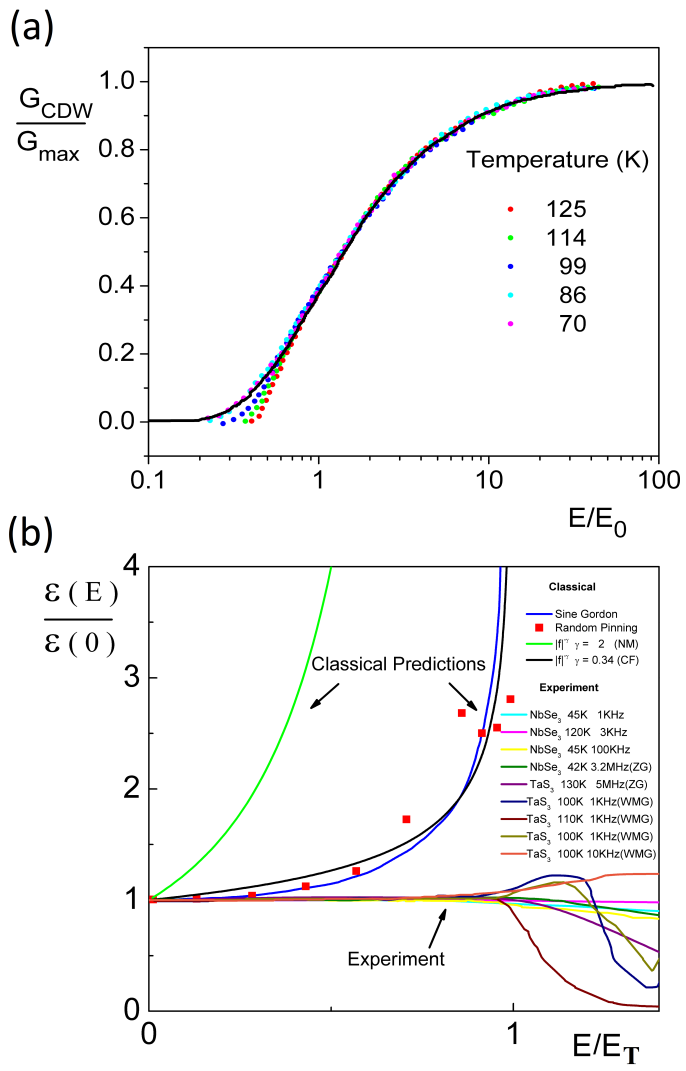

Figure 3.4: (a) Experimental conductance vs. electric field for $NbSe_3$, as compared to the Zener tunneling characteristic $\exp[-E_0/E]$ (solid line) pointed out by Bardeen [61]. (b) Bias dependent dielectric response (proportional to capacitance), showing contradiction of classical predictions vs experiment. Classical models include classical sine-Gordon, random pinning [31], renormalization group (NM [33]), and incommensurate harmonic chain models (CF [32]), where $f = 1 - E/E_T$. Some $NbSe_3$ measurements are carried out in our lab (see Appendix A.5.3) using a bridge circuit, while others were reported by ZG [28, 30] and WMG [29].

near the bottom of a pinning potential well, suggesting that E_T (measured) $<<$ E_T (classical). Furthermore, impedance and mixing experiments [27] yield results consistent with photon-assisted tunneling theory up to about 200 K. Aharonov-Bohm (A-B) quantum interference effect, showing oscillations of period $h/2e$ in the CDW conductance vs. magnetic flux have been reported for TaS_3 rings [25]. $NbSe_3$ crystals with columnar defects [24] further demonstrate the quantum character of the CDW condensate. Moreover, the fact that the period is $h/2e$, rather than $h/2Ne$, as predicted [26] for N parallel chains, suggests that the system behaves as a quantum fluid rather than a single massive object. As in Josephson tunneling, a complete theory must ultimately consider many microscopic degrees of freedom within the condensate, such as quantum solitons [21] or dressed electrons and holes that incorporate coupling to the $2k_F$ phonons.

Chapter 4

Soliton Nucleation Model of Density Wave Transport

4.1 Introduction

A wide class of nonperturbative phenomena in field theory can be undestood in terms of quantum tunneling. A well-known example is the quantum decay of the false vacuum [5], which has been a broad scientific interest in cosmology [62] and other fields [63] for over two decades. In three-dimensions, the boundary between the bubble of true vacuum and the surrouding false vacuum, is a type of topological defect known as a domain wall. A charge (flux) soliton-antisoliton pair in density waves [20, 21, 64] is a type of topological defect in condensed matter systems, which nucleate via quantum or thermal fluctuations.

4.2 Quantum Nucleation of Soliton-Antisoliton Pairs

The quntum decay of the metastable false vacuum of a scalor field ϕ, accompanied by the creation of solitons and antisolitons in (1+1)-dimensions, has been studied extensively in quantum field theory. Dias and Lemos [65] have calculated the effective one-loop action pair creation of soliton in (1+1)-D sine-Gordon model. In addition, they have extended their arguments to pair creation of soliton domain walls in higher dimensions.

Consider the problem of a scalar field theory in (1+1)-D with a metastable vacuum, that is a scalar potential which has a false vacuum ϑ_+ and a true vacuum ϑ_-, seperated by an energy density difference ϵ_v. In this case, the decay process can be interpreted as the false vacuum decaying into the true vacuum, plus a creation of a soliton-antisoliton pair:

$$\vartheta_+ \longrightarrow \vartheta_- + \ S \ + \ S'. \tag{4.1}$$

The energy necessary for the materialization of pair comes from the energy density difference between the two vacua. The soliton-antisoliton pair production rate per unit time and length is given by

$$\Gamma/L = \frac{\epsilon_v}{2\pi} e^{(\pi m^2/\epsilon_v)}. \tag{4.2}$$

Here, m represents the soliton mass and ϵ_v represents the gain in energy per unit length between the two created solitons, which are propotional to the applied electric field E for a density wave.

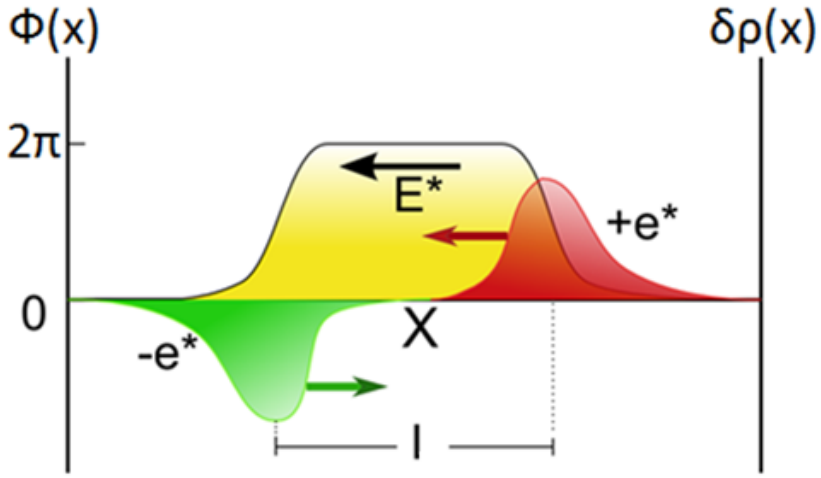

Figure 4.1: Materialized soliton-antisoliton pair. At $t = 0$, the system makes a quantum jump and a soliton-antisoliton pair is materialized. After materialization, the soliton and antisoliton are accelerated, driving away from each other.

At $t = 0$, the system makes a quantum jump and a soliton-antisoliton pair is materialized. After materialization, the soliton and antisoliton are accelerated, driving away from each other as shown in Fig. 4.1. The energy necessary for the materialization of the pair at rest is $E = 2m$. This energy comes from the conversion of false vacuum in to true vacuum. Since ϵ_v is the energy difference per unit length between two vacua, an energy of value $E = 2\epsilon_v$ is released within the pair. So, the pair materialization only occurs when energy release in a region of length R is equal to the rest energy: $2\epsilon_v R = 2m$. After the materialization, all the energy of the soliton-antisoliton pair released in the conversion between the two vacua, is used to accelerate the pair.

The current in density wave is $I = (Q_0/2\pi)\partial\phi/\partial t$ where $Q_0 \approx 2N_{ch}e$ and N_{ch} is the number of parallel chains. Charge solitons in density wave carry a charge of $\pm Q_0$. The soliton width is $\lambda_0 = c_0/\omega_0$, where c_0 is the phason velocity and ω_0 is the pinning frequency. The width λ_0 will increase with the decreasing impurity concentration (as ω_0 decreases), and may approach the distance between contacts on extremely pure samples.

4.3 Macroscopic Coulomb Blockade Model

The Coulomb blockade effect is well known for single electron tunneling and has also been proposed for charge soliton pair creation in the massive Schwinger model, which is essentially a quantum sine-Gordon model that includes electrostatic effects. The quantum picture discussed here interprets the threshold field due to Coulomb blockade of microscopic quantum solitons that transfer into soliton domain walls [66, 67].

The quantum interpretation of the threshold field, as a Coloumb blockade effect, is motivated by Colmen's paper [68] on soliton pair-creation in the massive Schwinger model.

A pair of S and S' domain walls with charge $\pm Q_0$ produces an internal field of magnitude $E^* = Q_0/\epsilon A$, as shown in Fig. 4.2, where A is the cross sectional area and ϵ is the dielectric constant. When an external field E is applied, the difference in electrostatic energies of a state with a pair seperation l and of the "vacuum" is given by,

$$\Delta U = \frac{1}{2}\epsilon A l \left[(E \pm E^*)^2 - E^2\right] = Q_0 l \left[\frac{1}{2}E^* \pm E\right]. \tag{4.3}$$

Note that ΔU is positive if $|E| < \frac{1}{2}E^*$. Therefore, conservation of energy forbids the vacuum to produce a pair if the field is less than a quantum threshold value $E_T \equiv \frac{1}{2}E^* = Q_0/2\epsilon A$, which can be much less than the classical depinning field E_{cl}.

Density waves are often highly anisotropic, where the dielectric response $\epsilon_{||}$, along the chain direction, is much greater than that of $\epsilon_\perp$ in the perpendicular directions. In this case, the Coulomb blockade threshold for nucleation of a 2π soliton-antisoliton

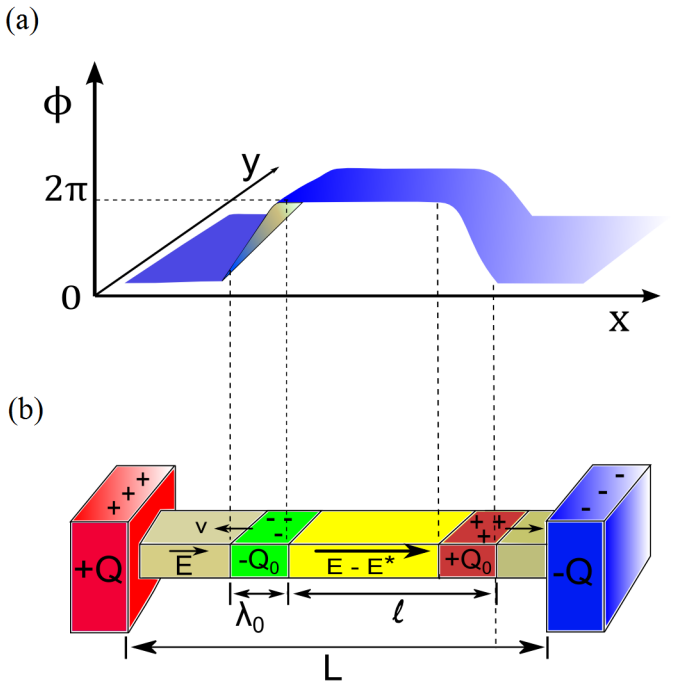

Figure 4.2: (a) CDW phase vs. position, showing a nucleated $S - S'$ domain wall pair. (b) Model of density wave capacitance in which charge soliton domain walls are moving towards the contacts. The applied field E, partially or completely cancels the internal field E^*. The distance ℓ, soliton width λ_0, and crystal thickness are greatly exaggerared for clarity.

(dislocation-antidislocation) pair (Fig. 4.3(a)) is comparable to that of domain wall pair creation, within a factor of $\approx 1/2$. This is seen by starting with the Maxwell equation: $\nabla \cdot D = \rho$, where (using the summation convention) $D_i = \epsilon_{ij} E_j$. Here $\epsilon_{i,j}$ is the relative dielectric tensor, which is diagonal with elements $\epsilon_{||} = \epsilon_{xx}$, $\epsilon_{\perp y} = \epsilon_{yy}$, and $\epsilon_{\perp z} = \epsilon_{zz}$, if the axes $i, j = x, y$, and z are along principal crystallographic directions. Introducing rescaled variables $x' = x/\epsilon_{||}$, $y' = y/\epsilon_{\perp y}$, and $z' = z/\epsilon_{\perp z}$ yield $\nabla' \cdot E = \rho/\epsilon_0$, resulting in the modified charge distribution, electrostatic potential, and field lines as shown in Fig. 4.3(b), which assumes that $\epsilon_{||} \perp \epsilon_{\perp xy}$. In the rescaled coordinate system of Fig. 4.3(b), the dislocation pair looks like a parallel plate capacitor that produces an internal field $E^* = 2e/2\epsilon A_{ch}$, where A_{ch} is the cross-sectional area of a density wave chain and $\epsilon = \epsilon_r \epsilon_0$. Figure 4.3(c) illustrates the aggregation of many 2π dislocations of charge $2e$ into soliton domain walls, each of which may behave as a quantum fluid and between which the bubble of true vacuum is grown.

A density wave between two contacts behaves as a capacitor with an enormous dielectric constant. The initial charging energy is $Q^2/2C$, where Q is the displacement charge and $C = \epsilon A/L$. We define

$$\theta = \frac{2\pi Q}{Q_0} = \frac{2\pi E}{E^*} = \frac{\pi E}{E_T}. \tag{4.4}$$

Note that displacement ϕ near the middle creates a non-topological kink-antikink pair with charge $\pm \left(\frac{\phi}{2\pi}\right) Q_0$, if $\phi = 0$ at the contacts. The sum of the washboard pinning and quadratic charging energies can be written as [66]

$$U(\phi) = \int_0^L dx \left\{ u_0 \left[1 - \cos \phi(x)\right] + u_{EM} \left[\theta - \phi(x)\right]^2 \right\}, \tag{4.5}$$

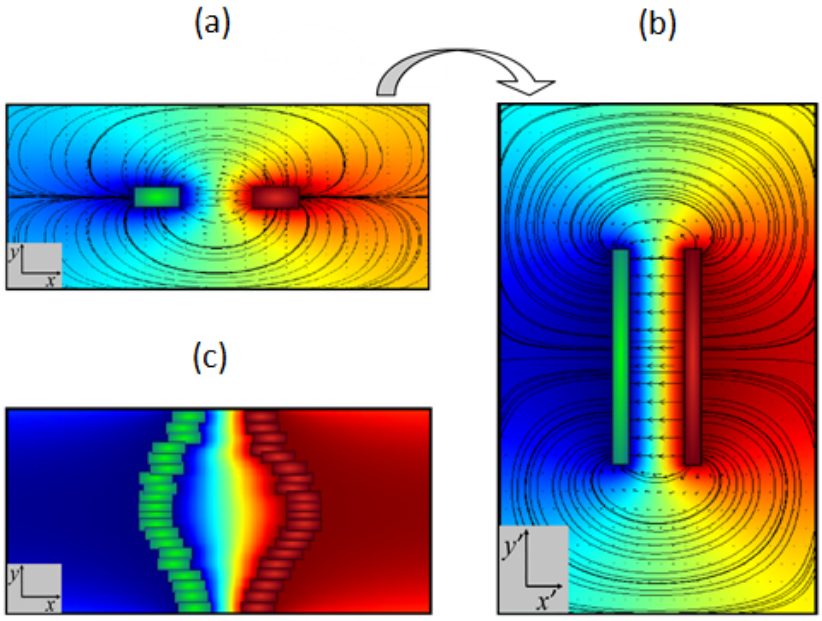

Figure 4.3: (a) COMSOL Multiphysics (COMSOL, Inc.) simulation of the electrostatic potential (red = positive, blue = negative) and electric field lines for an electric dipole consisting of dislocations represented as positive and negative rectangular charge distributions. (b) COMSOL simulation for the same system, but with highly anisotropic dielectric constants, in the rescaled coordinate system. The apparent distance between the charges is greatly reduced along the x' direction, yielding an arrangement resembling a parallel plate capacitor. (c) In the original coordinate system, aggregation of many dislocations into "domain walls", between which the bubble of "true vacuum" grows as the domain walls are driven toward the contacts by the externally applied electric field.

where the first term represents the pining energy and the last, quadratic term represents the electrostatic energy resulting from the net displacement charge or equivalently, the applied field and internal fields created by kinks due to phase displacements.

If the system starts out in its ground state, conservation of energy will prevent tunneling when the applied field is below threshold, $\theta < \pi$ $(E < E_T)$, as shown in Fig. 4.4. However, when θ exceeds π, what was formally the true vacuum becomes the unstable false vacuum. One or more bubbles of true vacuum with soliton domain walls at their surface then nucleate and expand rapidly.

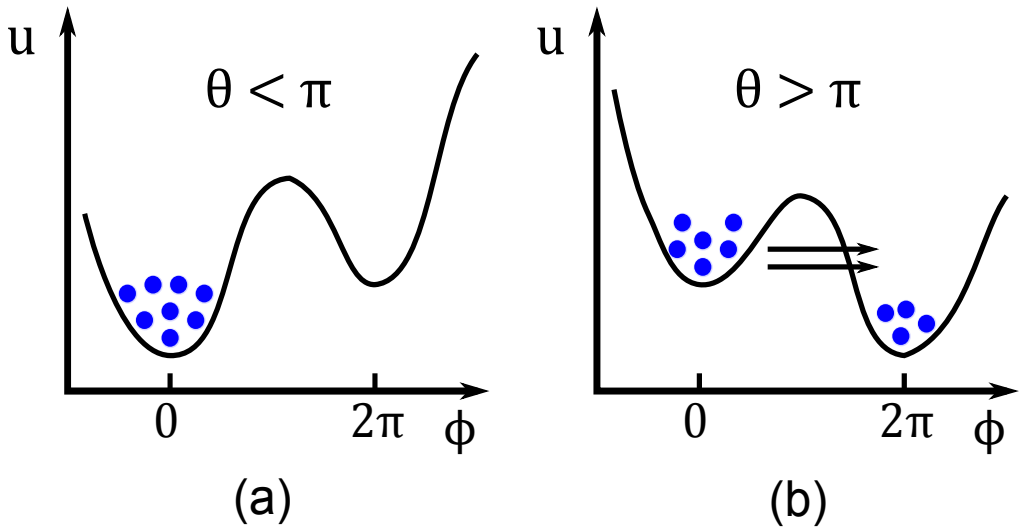

Figure 4.4: Plot of potential energy vs. ϕ for two different values of θ, in which the many spatial degrees of freedom are illustrated schematically. (a) When $\theta < \pi$, tunneling is prevented by conservation of energy. (b) When $\theta > \pi$, parts of the system tunnel into the adjacent well via decay of the false vacuum.

4.4 Tunneling Hamiltonian Matrix Element

The tunneling Hamiltonian is originally proposed by Bardeen [2] and is also discussed by Duke in Chapter 18 of Tunneling in Solids [69]. If ψ_p and ψ_q represent states on the left- and right-side of a potential barrier respectively; then, in the 1-D case, the matrix element coupling the two states is given by

$$T_{p,q} = \hbar i I_{p,q}, \tag{4.6}$$

where $I_{p,q} \equiv (\hbar/2mi)[\psi_q^* \partial_x \psi_p - \psi_p \partial_x \psi_q^*]$ is evaluated anywhere inside the barrier. First, let's consider a particle in a 1-D box with a rectangular potential barrier of width d, separating wells of width L in the two sides of the box as shown in Fig. 4.5. The wavefunctions are standing waves of energy $E_{p,q}$ in the wells and exponentially decay inside the barrier of height U with a decay constant $k \approx \frac{1}{\hbar}\sqrt{2mU}$, provided $U >> E_{p,q}$. By normalizing the wavefunctions, ensuring that they and their derivatives are continuous at the well-barrier boundaries, and letting x' measure the distance from the left side of the barrier, one finds the wavefunctions inside the barrier to be

$$\psi_p(x') \approx \frac{p\pi}{kL}\sqrt{\frac{2}{L}}\exp[-kx'] \tag{4.7}$$

and

$$\psi_q(x') \approx \frac{q\pi}{kL}\sqrt{\frac{2}{L}}\exp[-k(x'-d)], \tag{4.8}$$

yielding the matrix element

$$T_{p,q} = -[2pq\pi^2\hbar^2/(mL^3)]\exp[-kd]. \tag{4.9}$$

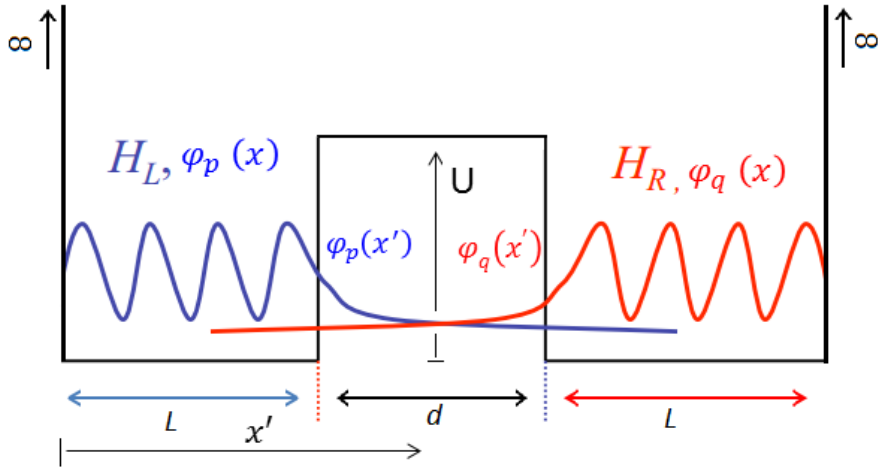

Figure 4.5: Particle in a one-dimensional box with a rectangular potential barrier of width d, separating wells of width L in the two sides of the box. The wavefunctions ψ_p and ψ_q are standing waves of energy E_p and E_q in the wells and exponentially decay inside the barrier of height U.

Recalling that $E_n = (n^2\pi^2\hbar^2)/(2mL^2)$, yields the result:

$$T_{p,q} = -[4\sqrt{E_p E_q}/(kL)]\exp[-kd] \tag{4.10}$$

or

$$T(E) = -[4E/(kL)]\exp[-kd] \tag{4.11}$$

for states of equal energy E.

Next, consider an energy gap $2\Delta_\psi$ tilted by a force F , for which the tunneling distance is $d = \ell = 2\Delta_\psi/F$, in a simple real-space picture as shown in Fig. 4.6. Inside the gap, $k \approx 1/\hbar\sqrt{2m\Delta_\psi} = \Delta_\psi/(\hbar c_0)$, since $m = \Delta_\psi/c_0^2 \rightarrow kd \approx \Delta_\psi^2/(\hbar c_0 F) \equiv F_0/F$.

After a materialized quantum soliton has traveled a distance L, its energy E relative to the upper band edge is $E = FL$, so $E/kL = F/k = F\lambda$, where $\lambda \equiv 1/k$, yielding the simple expression

$$T(F) = -4F\lambda\exp[-F_0/F]. \tag{4.12}$$

This result has the appeal of being similar to the rate of Schwinger pair production in 1-D [70].

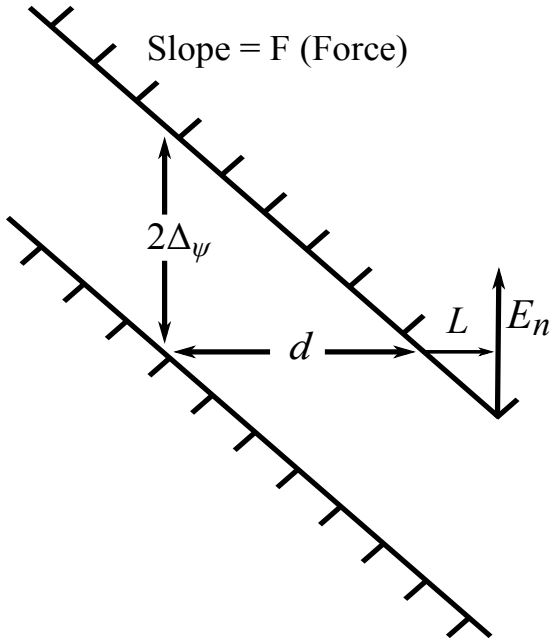

Figure 4.6: Simple real-space picture of an energy gap $2\Delta_\psi$, tilted by a force F, for which the tunneling distance is $d = \ell = 2\Delta_\psi/F$.

4.5 Time-correlated Soliton Tunneling Model

In this section, we propose an idealized time-correlated soliton tunneling model similar to the resistively and shunted junction (RSJ) model, to simulate density wave dynamics, including coherent voltage oscillations and I-V characteristics. This model has been widely used to describe the behavior of current-biased junctions [71]. It includes a shunt resistance R, representing normal, uncondensed electrons, in parallel with a capacitive tunnel junction representing soliton tunneling, by analogy to time-correlated singe-electron tunneling (SET) [72].

In this model, the parallel combination of two elements is driven by a current source, as shown in Fig. 4.7. The current source applies a current I to a pair of contacts, while the voltage $V(t)$ is measured across the same contacts or pair of inner contacts. Recalling that $\theta = 2\pi(Q/Q_0)$, The density wave current can be written in terms of displacement charge Q as,

$$I_{DW} = \frac{dQ}{dt} = \frac{Q_0}{2\pi}\frac{d\theta}{dt}. \tag{4.13}$$

Advancing the phase of all parallel chains by $2\pi n$ creates multiple pairs of soliton domain walls of total charge $\pm nQ_0$, that quickly reach the contacts. Similar to SET, the voltage is then proportional to net displacement charge

$$V = (Q - nQ_0)/C = (Q_0/2\pi C)[\theta - 2\pi n], \tag{4.14}$$

when the phase has advanced to $\langle\phi\rangle = 2\pi n$ between the contacts. More generally, if the phase expectation value $\langle\phi\rangle$ among N parallel chains advances by a fraction or

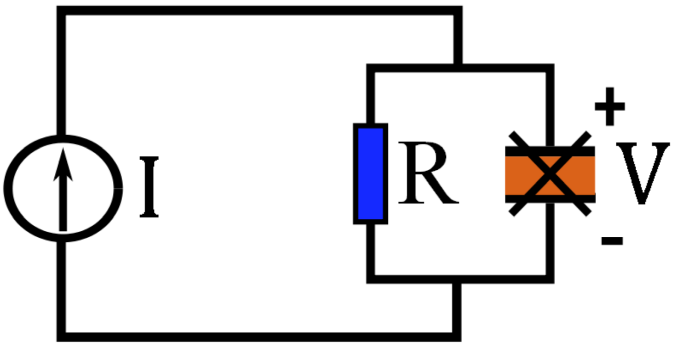

Figure 4.7: Modified resistively shunted junction model, in which time-correlated tunneling of soliton and antisoliton is represented by analogy to time-correlated SET.

non-integer multiple of 2π, the voltage is

$$V = (Q_0/2\pi C)[\theta - \langle\phi\rangle] \tag{4.15}$$

where $C = \epsilon A/\ell$. This leads to a total current

$$I = I_n + I_{DW}, \tag{4.16}$$

where $I_n = (Q_0/2\pi RC)[\theta - \langle\phi\rangle]$ is the normal current.Defining $\omega = 2\pi I/Q_0$ and $\tau \equiv RC$ yields the following equation for the time evolution of θ:

$$\frac{d\theta}{dt} = \omega - \frac{1}{\tau}[\theta - \langle\phi\rangle]. \tag{4.17}$$

Two approaches are used for computing $\langle\phi\rangle$, voltage, and density wave current vs. time, employing tunneling probabilities and probability amplitudes. Whereas the method employing probabilities (discussed in Appendix A.6) predicts sharp sawtooth behavior in coherent voltage oscillations. The latter approach, which yields much better agreement between theory and experiment on high quality $NbSe_3$ crystals, is discussed below. It is motivated by Feynman's treatment [73] of the superconducting Josephson junction and employs the Schrödinger equation, to describe the time evolution of the original and emerging macrostates.

First, we compute $\langle\phi\rangle$ by solving the Schrödinger equation

$$i\hbar\frac{\partial\psi_{0,1}}{\partial t} = U_0\psi_{0,1} + T\psi_{1,0} \ , \tag{4.18}$$

to compute the original and emerging macrostate amplitudes $\psi_0(t)$ and $\psi_1(t)$ (more generally ψ_n and ψ_{n+1}) for the system to be on branches 0 and 1 (or n and $n+1$, Fig. 4.8), respectively. We interpret these amplitudes to represent classically

robust order parameters, and the above equation is viewed as an emergent classical equation following Feynman [73]. The macrostates are coupled via a tunneling matrix element T with a Zener-like field dependence.

Our model represents the amplitudes $\psi_{0,1}$ by

$$\psi_{0,1} = \sqrt{\rho_{0,1}} \exp\left[i\delta_{0,1}\right], \tag{4.19}$$

where $\rho_{0,1} = N_{0,1}/N$ is the fraction of parallel chains on the respective branch. Advancing $\phi_k(x)$ by 2π within a given region, taking ϕ_k from one branch to the next, is equivalent to creating a pair of microscopic 2π-solitons. Thus, the macrostate order parameters $\psi_{0,1}$'s are coupled via coherent, Zener/Josephson tunneling of delocalized quantum solitons [21], with an enormous aggregate of N (up to $\sim 10^9$) such processes occurring coherently.

The driving force is the energy difference per unit length between potential minima at $\phi \sim 2\pi n$ and $\phi \sim 2\pi(n+1)$. When $\alpha \equiv u_{EM}/u_0 << 1$, this force is given by

$$F = 4\pi u_{EM}\theta'_n, \tag{4.20}$$

where $\theta'_n = \theta - 2\pi(n + \frac{1}{2})$. Following Bardeen [2, 69], T is estimated as

$$T(F) = -4F\lambda \exp[-F_0/F], \tag{4.21}$$

where $\lambda^{-1} \sim \Delta_\varphi/\hbar v_0 + \lambda_m^{-1}$, λ_m is the mean free path length, Δ_φ is the microscopic soliton energy, v_0 is the phason velocity, and $F_0 \sim \Delta_\varphi^2/\hbar v_0$. This expression is similar to the rate of Schwinger pair production in 1-D [70]. Since any negative energy difference (Figs. 4.2(a) & (b)) within the "bubble" along the x- direction is

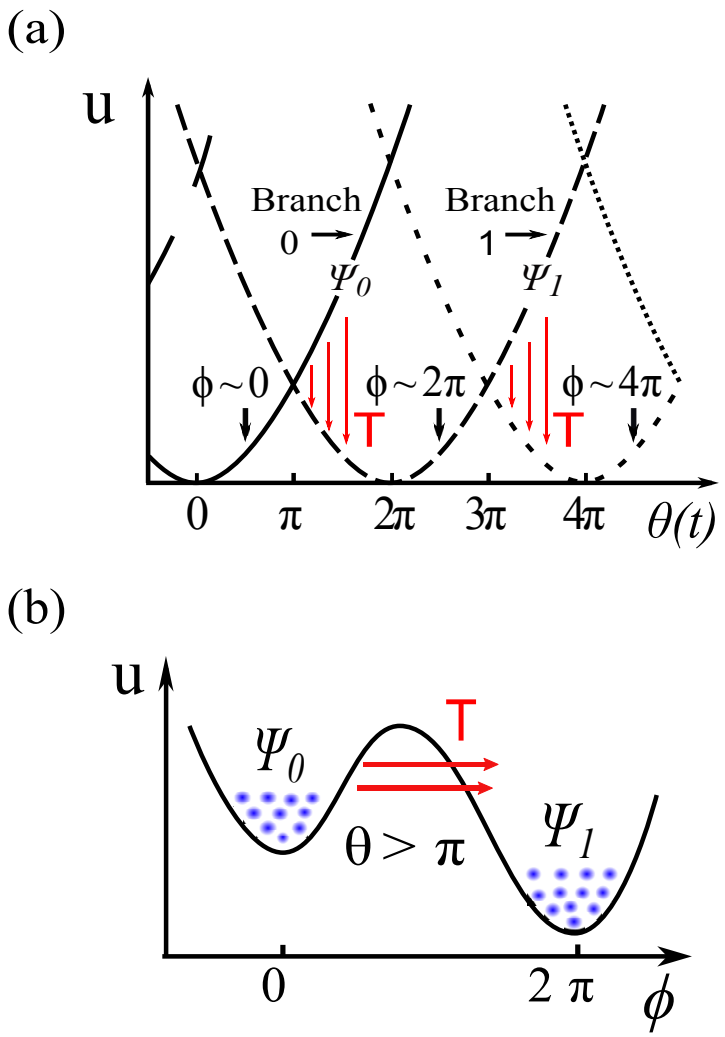

Figure 4.8: (a) Potential energy (u) vs. θ, showing several parabolic branches for $\phi \sim 2\pi n$, representing electrostatic charging energies $(Q - nQ_0)^2/2c \propto (\theta - 2\pi n)^2$. (b) u vs. ϕ when $\theta = 2\pi E/E^* > \pi (E > E_T)$ as the phases $\phi_k(x)$ tunnel coherently into the next well via the tunneling matrix element T.

balanced by the positive soliton pair energy at its boundaries, T couples states of equal energy $U_0 = U_1 = U$. Thus, defining

$$\psi_{0,1} = \chi_{0,1}(t) \exp[-iUt/\hbar], \tag{4.22}$$

the Schrödinger equation (Eqn. (4.18)) reduces to

$$i\hbar \partial \chi_{0,1}/\partial t = T\chi_{1,0}. \tag{4.23}$$

We define: $t' = t/\tau$, $f = \omega\tau/2\pi$ ($\propto I$), $q = \theta/2\pi$, $q_o = F_0/2F_T = \theta_0/2\pi$, $F_T = 2eE_T$, and $q'_n = \theta'_n/2\pi = q - n - \frac{1}{2}$, to simplify the computations. Finally, setting $\chi_0(t) = c_0(t)$ and $\chi_1(t) = ic_1(t)$, taking c_0 and c_1 to be real, yields the coupled equations:

$$dc_1/dt' = [\gamma q'_n \exp(-q_0/q'_0)]\, c_0 \tag{4.24}$$

and, for $q'_n > 0$,

$$dc_o/dt' = -[\gamma q'_n \exp(-q_0/q'_n)]\, c_1 \tag{4.25}$$

where $\gamma = 32\pi^2 u_E \lambda\tau/\hbar$. These are integrated numerically, with initial values $c_0 = 1$ and $c_1 = 0$, yielding $\langle\phi\rangle = 2\pi[n + p]$, where $p = |c_1|^2$. The transition from branch n to $n + 1$ is considered complete, and n is incremented while p is reset back to zero, once p exceeds a cutoff close to one (*e.g.* 0.9995). When the applied current pulse is turned off, any remaining displacement charge discharges back through the shunt resistance and the system retains a memory of the previous macrostate amplitudes. The algorithm thus incorporates backward transitions from branch n to branch $n-1$, when dQ/dt, F, and q'_n are negative. We find that no more than three training pulses are needed to converge to a "fixed point" of one or two voltage oscillation patterns, which are averaged.

4.6 Comparison of Experimental Results with Soliton Nucleation Theory

4.6.1 Pulse Response

Figures 4.9(a) & (b) show a comparison between the quantum theory simulations vs. experimental coherent voltage oscillations, for several rectangular current pulses amplitudes. The parameters used to obtain the theoretical plots (solid lines) in Fig. 4.9(a) are: $\gamma = 0.5$, $q_0 = 0.7$, $\tau = 51\ ns$, $V^* = E^*\ell = 1.11\ mV$ (where ℓ= distance between contacts), and $R_n = 100\ \Omega$. The measured threshold current of 6.93 μA is taken to correspond to $f = 0.6$, the normalized onset threshold current consistent with the chosen values of γ and q_0, and the remaining current pulse amplitudes f's are scaled accordingly to the indicated amplitudes in Fig. 4.9(a) ranging from 9.90 μA to 11.88 μA. The parameters used to obtain the theoretical plots (solid lines) in Fig. 4.9(b) are: $\gamma = 4.2$, $q_0 = 1.55$, and f's are 2.20, 2.60, and 2.80.

Moreover, the model correctly reproduces the experimentally observed progression of non-sinusoidal voltage oscillation shapes, ranging from rounded backward sawtooth behavior for lower current pulse to more symmetrical oscillations for higher current amplitudes. As in classical models, the coherent oscillation frequency equals the density wave drift frequency $f_d = I_{DW}/Q_0$ in our model. Thus, for a given pulse width, the number of voltage oscillations increase with pulse amplitude. The model captures the correct number of oscillations for different applied current amplitudes using the same parameters.

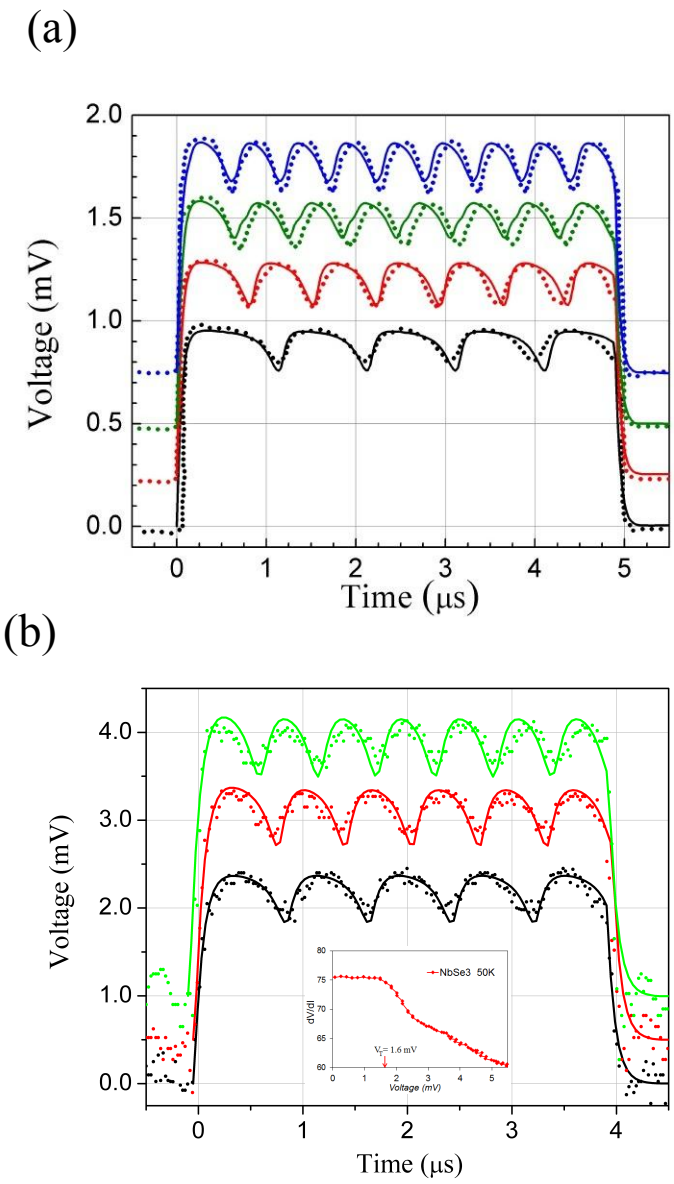

Figure 4.9: (a) Theoretical (solid lines) vs. experimental (dotted lines [74]) coherent voltage oscillations of an $NbSe_3$ crystal at 52 K, for current pulse amplitudes (bottom to top): 9.90 μA (black), 10.89 μA (blue), 11.49 μA (red), 11.88 μA (green), with 0.25 mV offset, using a consistent set of parameters for the theoritical plots. (b) Theoretical (solid lines) vs. experimental (dotted lines) coherent voltage oscillations of an $NbSe_3$ crystal at 50 K, for current pulse amplitudes (bottom to top): 29.3 μA (black), 34.6 μA (red), 37.3 μA (green), with 0.5 mV offset. Inset shows the differential resistance vs. bias voltage for the same $NbSe_3$ sample at the same temprature.

4.6.2 Current Voltage Response

The I_{DW}-V and dV/dI characteristics of Figs. 4.10- 4.12 are computed by simulating each applied current as a step function, and then averaging the voltage over several complete oscillations once the time-averaged voltage reaches a plateau. Figures 4.10 and 4.11 show resulting plots of normalized density wave current vs. field and differential resistance dV/dI vs. total current, respectively, for several values of $q_0 = \theta_0/2\pi$ and a fixed value of $\gamma' = 1.5$. The dotted lines in Fig. 4.10 are obtained from a normalized Bardeen function [19], $I_{DW}/I^* = \Gamma[E' - E'_{Tm}]\exp[E'_{0m}/E']$, where $E' = E/E^*$ and $I^* = (E^*\ell)/R_n$, while $E'_{Tm} = E_{Tm}/E^*$ and $E'_{0m} = E_{0m}/E^*$ represent normalized, "measured" threshold and Zener activation fields and $\Gamma = 1.0$ for all three plots. The remaining parameters used for the Bardeen function fits to the simulations, for $q_0 = 2$, 4, and 6, are shown in Table 4.1 below.

q_0	E'_{Tm}	E'_{Om}
2	0.847	0.96
4	1.10	2.55
6	1.40	4.05

Table 4.1: Parameters used to generate plots of the normalized Bardeen function, $I_{DW}/I^* = \Gamma[E' - E'_{Tm}]\exp[E'_{Om}/E']$, for comparison with the simulated I_{DW} vs. V curves in Fig. 4.10.

The measured normalized threshold E_{Tm}/E^* becomes significantly greater than the Coulomb blockade threshold, $E_T/E^* = 0.5$, as q_0 increases. This can be clearly seen in Fig. 4.11 as well. The dotted lines in Fig. 4.11 show, for an $NbSe_3$ crystal, differential resistance $R = dV/dI$, normalized to normal resistance $R_n = dV/dI|_{zerobias}$ vs. I/I_{Tm}, where I is the total applied current and $I_{Tm} = V_{Tm}/R_n$ is the measured

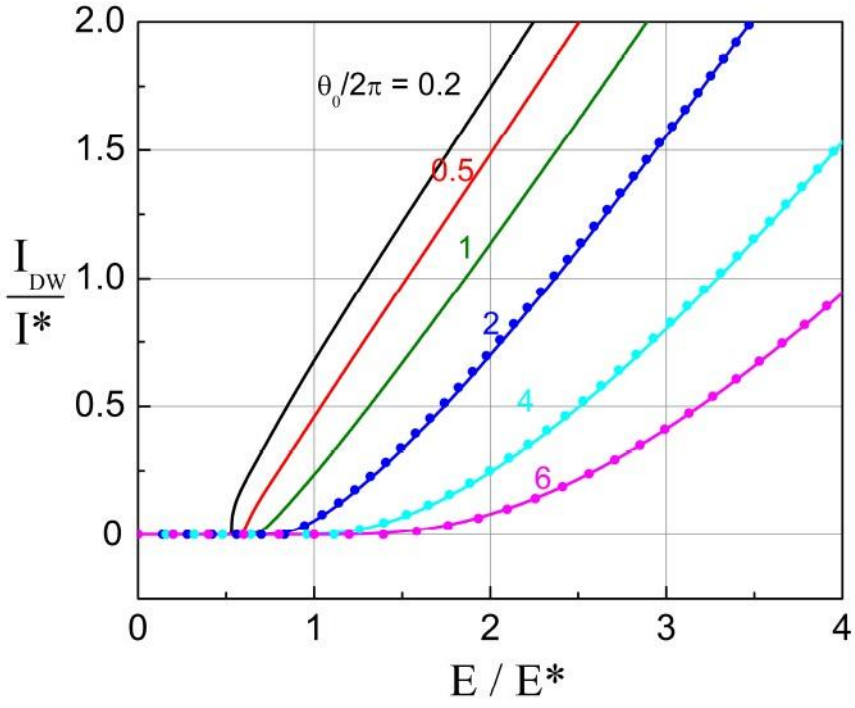

Figure 4.10: Predicted density wave current vs. field for several values of $\theta_0 \propto E_0/E_T$ for a fixed value of $\gamma = 0.5$. The dotted lines are fits to Bardeen's modified Zener characteristics $j_{DW} \propto [E - E_{Tm}] \exp[-E_{Om}/E]$.

threshold current. The solid lines in Fig. 4.12 are the results of simulations using the parameters indicated in Table 4.2 below.

Temperature	I_{Tm}/I^*	γ'	q_0
20 K	0.87	2.7	3.0
25 K	0.76	3.2	2.3
35 K	1.27	2.8	6.7
70 K	1.71	0.41	8.5
120 K	2.22	0.275	10.0

Table 4.2: Parameters used to generate the simulated dV/dI curves in Fig. 4.12 (solid lines).

A wide range of experimentally observed behaviors are captured by the model, with rounded Zener-like behavior [19, 60] emerging for relatively large values of $\theta_0 \propto E_0/E_T$, while more linear I-V curves and dV/dI curves with negative dips, as seen in $NbSe_3$ crystals with relatively low impurity concentration [56], result when E_0/E_T is small. For small θ_0, when the dV/dI simulations show negative wings, the measured threshold or onset for non-linear transport E_{Tm} occurs near the Coulomb blockade threshold: $E_{Tm} = E_T = E^*/2$. However, E_{Tm} becomes significantly larger than $E^*/2$ as θ_0 increases, as seen in Fig. 4.11. Figure 4.12 shows a direct comparison between theoretical and experimental dV/dI vs. I measurements, on an $NbSe_3$ crystal that exhibits rounded behavior, in which excellent agreement is obtained for several temperatures below the upper and lower Peierls transitions.

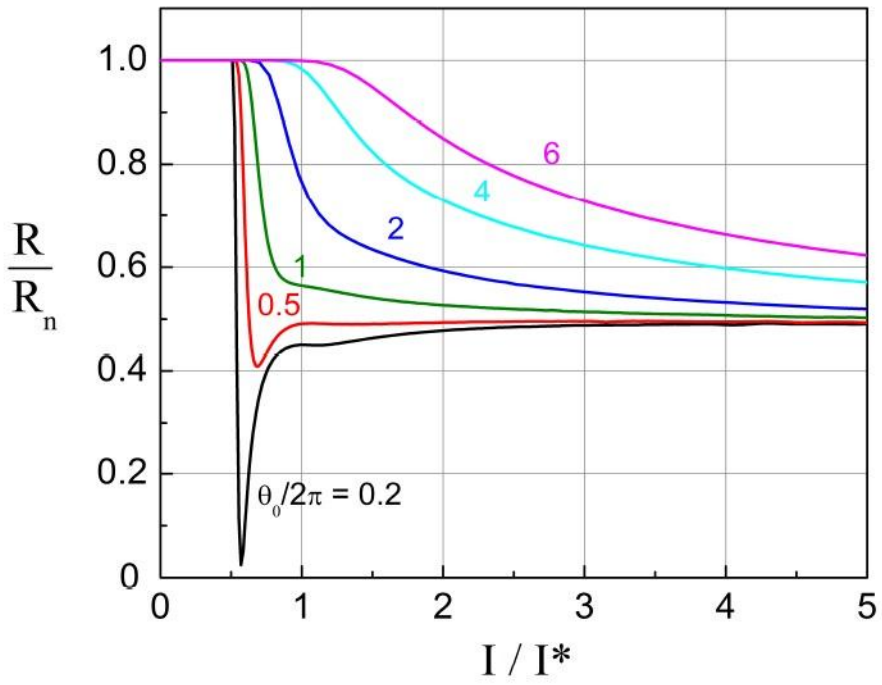

Figure 4.11: Simulated normalized differential resistance ($R = dV/dI$) vs. I/I^*, where $I^* = E^*\ell/R_n$ and ℓ is the distance between contacts, for several values of $q_0 = \theta_0/2\pi$ and $\gamma = 1.5$.

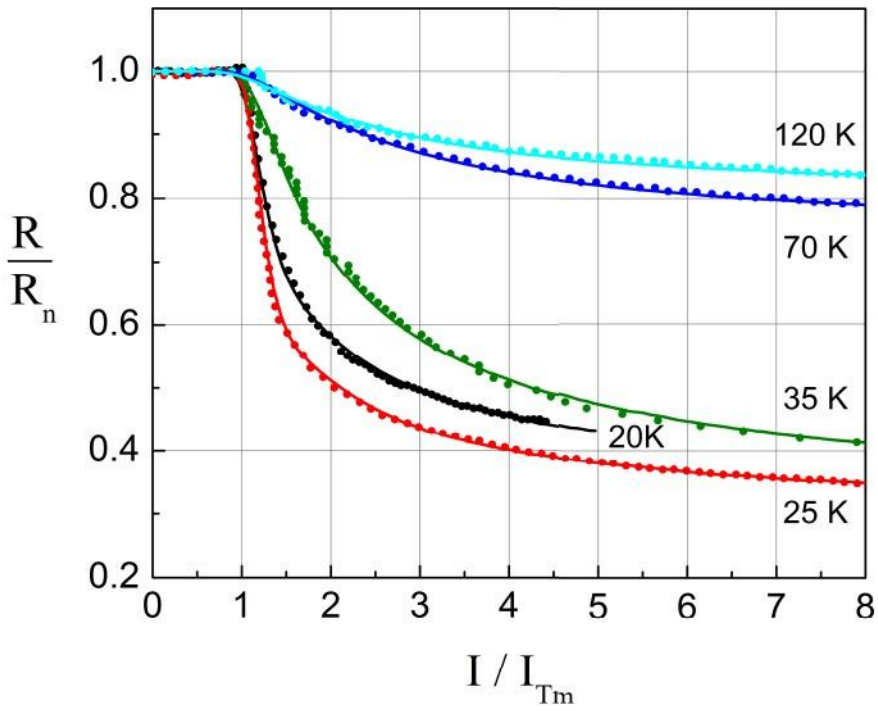

Figure 4.12: Theoretical (solid lines) and experimental (dotted lines) differential resistance vs. current plots for an $NbSe_3$ crystal at several tempratures below the upper and lower Peierls transitions. Theoretical plots are obtained using parameters in Table 4.2.

4.7 Discussion

The existence of more than one threshold is another feature observed in several CDW materials. The clearest evidence [75] is seen below 77 K in $K_{0.3}MoO_3$ (blue bronze), where an initial threshold at low fields is followed by a dramatic increase in differential conductance above a high field threshold, as shown in Fig. 4.13. These two major thresholds emerge naturally, provided the nucleated soliton conductance is sufficiently small for θ to be treated quasi-statically, *i.e.* $\theta = \pi\epsilon E/\epsilon_1 E_T$, where $\epsilon_1 = \epsilon(E \approx E_T)$ and ϵ is the field-dependent dielectric response.

The interpretation proposed here is that the low-field threshold E_{TS} is due to soliton nucleation, while the high-field threshold E_{cl} is due to classical depinning field. Figure 4.13(b) (left) illustrates the quantum ($\theta \geq \pi$) and classical ($\theta \geq \theta_c$) instabilities, where $\theta_c(\alpha) \cong \alpha^{-1} + \pi/2$, when $\alpha = u_{EM}/u_0 << 1$. Figure 4.13(b) (right) plots the pinning potential vs. ϕ, when $\theta = \pi$ for several values of α, showing the electrostatic energy dominance over pinning when $u_{EM}/u_0 \geq 1$. Figure 4.13(c) shows the resulting θ vs. u_{EM}/u_0 phase diagram, which illustrates the fully pinned states, $\theta < \pi$ and $u_{EM}/u_0 < 1$, a region ($\pi \leq \theta < \theta_c$) in which soliton nucleation occurs, and a high field threshold above which classical depinning occurs ($\theta \geq \theta_c$).

Experiments suggest that $NbSe_3$ and TaS_3 samples for most temperature ranges are in the limit $u_{EM}/u_0 << 1$ (red arrow in Fig. 4.13(c)), so that soliton nucleation is the primary CDW transport mechanism in these systems. $NbSe_3$, in particular, has an extraordinarily high dielectric constant, which is consistent with u_{EM} being much smaller than u_0, since u_{EM} scales inversely with ϵ. However, the blue bronze

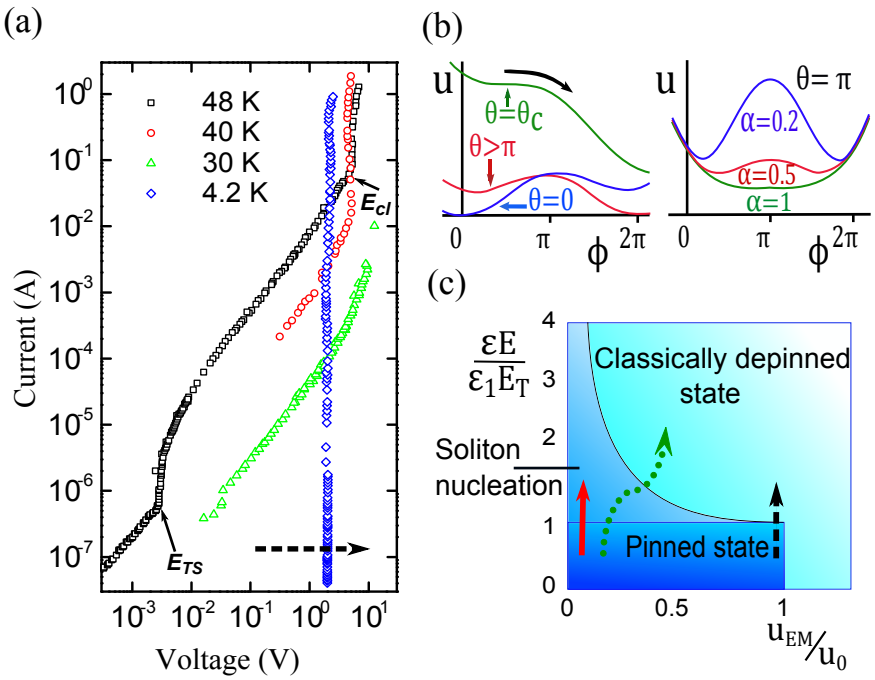

Figure 4.13: (a) I-V characteristics of blue bronze [75]. (b) (left) Potential energy u vs ϕ, showing $\theta \geq \pi$ quantum instability and $\theta \geq \theta_c$ classical depinning. (b) (right) u vs. ϕ at $\theta = \pi$ for several values of u_{EM}/u_0. (c) Proposed θ/π vs. u_{EM}/u_0 phase diagram, showing the pinned, soliton nucleation, and classically depinned states. E_T is the soliton nucleation threshold, ϵ_1 is the dielectric response for $E \approx E_T$, and ϵ depends on bias. The red arrow: $u_{EM}/u_0 << 1$ for which soliton pair creation dominates. The green arrow shows both soliton nucleation and classical depinning. Since $u_{EM} \propto 1/\epsilon$, the path curves to the left (right) if ϵ increases (decreases). The black arrows (a) & (c): classical depinning dominates.

data in Fig. 4.13(a) suggests a higher u_{EM}/u_0 , which enables both soliton nucleation and classical depinning thresholds to emerge, as indicated by the green arrow. In blue bronze, the dielectric response scales with the concentration of normal carriers thermally excited across the Peierls gap. At 4 K, the normal carriers become frozen out and the resulting low carrier concentration results in a relatively low ϵ, leading to a value of u_{EM}/u_0 sufficiently high for classical depinning to dominate, as indicated by the black arrows in Figs. 4.13(a) & (c).

Chapter 5

Response at Megahertz Frequencies: Photon-assisted Tunneling Theory

5.1 Introduction

The phenomena of photon-assisted tunneling (PAT) theory is first observed in superconductor-insulator-superconductor (SIS) tunnel junction in 1962 by Dayem and Martin [76], and explained theoretically in 1963 by Tien and Gordon [77]. The modifications made later [78] are useful for describing the behavior of the other non-linear characteristics of the systems at high frequencies. The following section will summarize the basic PAT theory applied to the CDW system. A formal derivation of this result may be found in the original literature of Tucker [79] and Miller [27].

5.2 Photon-assisted Tunneling Theory

Following the treatment by Bardeen [2], and by Cohen, Falicov, and Philips [3], the total Hamiltonian for the tunnel junction is given by

$$H \;=\; H_L \;+\; H_R \;+\; H_T \tag{5.1}$$

where H_L and H_R are the full many-body Hamiltonians for the left- and right-hand electrodes. The transfer Hamiltonian H_T, that couples the two sides, is given by

$$H_T = \sum_{kq} \left[T_{kq} c_k^+ c_q + T_{kq}^* c_q^+ c_k \right], \tag{5.2}$$

$$H_T = H_T^+ + H_T^- \tag{5.3}$$

where c_k and c_q are single-electron operators representing Bloch states on the left- and right-hand sides of the junction, respectively, and T_{kq}'s are the tunneling matrix elements. The term in H_T^+ thus transfers electron from right to left across the barrier, while H_T^- performs the reverse function. Photon-assisted tunneling theory treats the current response of the junction to an applied potential $eV(t)$, which modulates the energy of each electron on the left-hand side with respect to the right-hand side. It is assumed that this modulation occurs sufficiently slowly so that the density matrix for the uncoupled system retains its thermal equilibrium form. The only impact of the applied potential on the uncoupled system then appears as a simple phase modulation of all the left-side electron operators,

$$c_k(t) = \; c_k^o(t) \exp\left\{ \frac{-i}{\alpha} \int^t dt V(t) \right\} \tag{5.4}$$

$$= \; c_k^o(t) \exp -i(V_0 t/\alpha) \int_{-\infty}^{\infty} d\omega' W(\omega') e^{i\omega' t} \tag{5.5}$$

where $c_k^0(t)$ denotes the Heisenberg operator in the absence of an applied potential and $\alpha = \hbar/e$ represents a quantum scaling parameter between frequency and voltage. In Eqn. (5.5), the dc bias has been explicitly extracted and the time varying contribution expressed in terms of $W(\omega')$'s Fourier transform

$$\exp\left\{\frac{-i}{\alpha}\int^t dt'[V(t)-V_0]\right\} = \int_{-\infty}^{\infty} d\omega' W(\omega') e^{i\omega' t}. \tag{5.6}$$

The expectation value for the total current is calculated by treating the coupling through the transfer Hamiltonian H_T, as a perturbation, and using linear response theory, with the result

$$\langle I(t)\rangle = Im \int_{-\infty}^{\infty} d\omega' W(\omega') W^*(\omega'') e^{-i(\omega'-\omega'')t} \times \; j(\omega' + V_0'/\alpha). \tag{5.7}$$

The complex response function $j(w)$, is expressed in terms of the effective dc I-V characteristics:

$$im\ j(w) = I'(\alpha w) \quad and \quad Re\ j(w) = I'_{kk}(\alpha w) \tag{5.8}$$

where $I'(V) = I_{dc}(V)$ for the case of a tunnel junction. I'_{kk} is the Kramers-Kronig transform of the dc I-V characteristic. The results for the current response to an applied time-dependent potential may, therefore, be expressed in terms of the dc I-V characteristics.

5.2.1 Photon-assisted Tunneling Theory for Current Response in the Presence of an ac Signal

Let's now apply PAT theory to calculate the current induced by an applied sinusoidal potential

$$V(t) = V_o^{'} + Re(V_1 e^{iwt}), \tag{5.9}$$

where V_1 is taken to be real. The time dependent of the quantum mechanical phase factor induced by the potential is given by,

$$\exp\left\{\frac{-i}{\alpha}\int^t dt V_1 \cos\omega t\right\} = \exp\left\{-i\left(\frac{V_1}{\alpha\omega}\right)\sin\omega t\right\} \tag{5.10}$$

$$= \sum_{m=-\infty}^{\infty} J_n(V_1/\alpha\omega)\ e^{-in\omega t}. \tag{5.11}$$

The Fourier transform of this induced time dependence is, therefore,

$$W(\omega^{'}) = \sum_{m=-\infty}^{\infty} J_n(X)\ \delta(\omega^{'} - n\omega) \tag{5.12}$$

where $X = V_1/\alpha\omega$ is a dimensionless parameter proportional to the magnitude of the applied signal. The current response for this case is obtained by

$$\langle I(t)\rangle = Im \sum_{n,m=-\infty}^{\infty} J_n(X)\ J_{n+m}\ e^{+im\omega t}\ j(n\omega + V_0/\alpha) \tag{5.13}$$

$$= a_0 + \sum_{m=1}^{\infty} \left[2a_m \cos m\omega t + 2b_m \sin m\omega t\right]. \tag{5.14}$$

The strength of the current components at the various harmonics of the applied frequency are given by

$$2a_m = \sum_{n=-\infty}^{\infty} J_n(X)\left[J_{n+m}(x) + J_{n-m}(x)\right] I'(V_0' + n\alpha\omega) \tag{5.15}$$

and

$$2b_m = \sum_{n=-\infty}^{\infty} J_n(X)\left[J_{n+m}(x) - J_{n-m}(x)\right] I'_{kk}(V'_0 + n\alpha\omega). \tag{5.16}$$

The induced dc current response I'_{dc}, in the presence of a large-amplitude ac signal of frequency ω_{ac}, is given by,

$$I'_{dc}(V'_0, V'_{ac}) = \sum_{n=-\infty}^{\infty} J_n^2(x) I'(V'_0 + n\alpha\omega_{ac}) \tag{5.17}$$

where $I'(V'_0)$ represents the intrinsic dc current response of any applied ac signal, and $x = V_{ac}/\alpha\omega_{ac}$ denotes the argument of the Bessel function. Taking the third derivative of both sides of the Eqn. (5.17) with respect to V'_0 yields

$$\frac{d^3 I'_{dc}(V'_0, V_{ac})}{dV_0'^3} = \sum_{n=-\infty}^{\infty} J_n^2(x) \frac{d^3 I'(V'_0 + n\alpha\omega_{ac})}{dV_0'^3}. \tag{5.18}$$

If a current response is induced by one or more small ac signals of frequencies other than ω_{ac}; then, one would expect that the third derivatives in Eqn. (5.18) shold be replaced by third finite differences. This suggests that an induced current response δI, in the presence of an additional ac signal of amplitude V_{ac} and frequency ω_{ac}, should be given by,

$$\delta I(V'_0, V'_{ac}) = \sum_{n=-\infty}^{\infty} J_n^2(x) \delta I'(V'_0 + n\alpha\omega_{ac}) \tag{5.19}$$

where $\delta I(V'_0)$ represents the induced response in the absence of the additional ac signal.

Suppose now, that the frequency of the additional ac signal is increased, so that the quantum step size $\delta V = \alpha\omega_{ac}$ becomes significant. From Eqn. (5.19), an induced ac response at zero bias is now be given by

$$\delta I(V'_{ac}) = \sum_{n=-\infty}^{\infty} J_n^2(x) \delta I'(n\alpha\omega_{ac}) \tag{5.20}$$

where $x = V_{ac}/\alpha\omega_{ac}$, with α representing the scaling between frequency and voltage, and $\delta I'(V_0')$ representing the intrinsic response as a function of bias voltage V_0'.

When the frequency ω_{ac} is sufficiently high; however, $\delta I(n\alpha\omega_{ac}) \approx 0$ for $|n| \geq 1$, because the large quantum energies $n\alpha\omega_{ac}$ sample only regions of the I-V curves that are nearly linear. Then, the Eqn. (5.20) in this limit becomes

$$\delta I(V_{ac}') \approx J_0^2(V_{ac}/\alpha\omega_{ac}). \tag{5.21}$$

Above equations, predict a scaling between the frequency and the voltage. The scaling parameter α can be obtained experimentally by comparing the measured current response in the presence of a large-amplitude ac signal.

5.2.2 Photon-assisted Tunneling Theory on Charge Density Wave System

In a normal quasi particle tunnel junction, the voltage step size that corresponds to a quantum of frequency ω is given by $\delta V = \hbar\omega/e$, so that scaling parameter is $\alpha = \hbar/e$. Application of the PAT theory to a CDW system appears to require some modifications to the scaling parameter α. In CDW systems,, the effective voltage for accelerating CDW electrons is that across a effective small tunneling length L_D, known as scaling length, per domain ("tunnel junction"), rather than across the entire sample length ℓ and relevant charge, which is taken to be $2e$. Thus, the scaling parameter used in the CDW tunneling theory is taken to be

$$\alpha = \frac{N_D\hbar}{2e} \tag{5.22}$$

$$\alpha = \frac{\hbar}{2e}\frac{\ell}{L_D}. \tag{5.23}$$

where N_D=ℓ/L_D is approximately the number of Lee-Rice domains in series along the sample length. Therefore, scaling length

$$L_D = \frac{\hbar}{2\alpha e}\ \ell \tag{5.24}$$

can be expressed in terms of α.

5.3 Experimental Results Compared with Photon-assisted Tunneling Theory

5.3.1 Linear Response

To calculate the theoretical predictions for the complete ac response for the $NbSe_3$ from photon assisted tunneling theory, first, a fit to the dc I-V characteristic is obtained using the expression,

$$I_{CDW}(V) \;=\; I(V) - G_a V \tag{5.25}$$

$$I_{CDW}(V) = \; G_{b1}(V - V_{T1})e^{-m(V_{T1}/V)} + G_{b2}(V - V_{T2})e^{-n(V_{T2}/V)} \tag{5.26}$$

where $G_a = 11.4$ mmho, $G_{b1} = 0.94$ mmho, $G_{b2} = 0.013$ mmho, $V_{T1} = 0.015$ V, $V_{T2} = 1.15$ V, $m = 5.70$ mho, and $n = 3.82$ mho.

Figure 5.1 shows the experimentally measured CDW current as a function of bias voltage for sample $NbSe_3$ at 120 K. The solid line is the fitting function of the experimental result to the Eqn. (5.26). The dc I-V data are well characterized by this slightly modified version of Zener-type tunneling expression. The detailed form of the fitting function utilized in Eqn. (5.26) is relatively unimportant, since calculations based on PAT theory requires only that the true dc I-V characteristic be accurately represented.

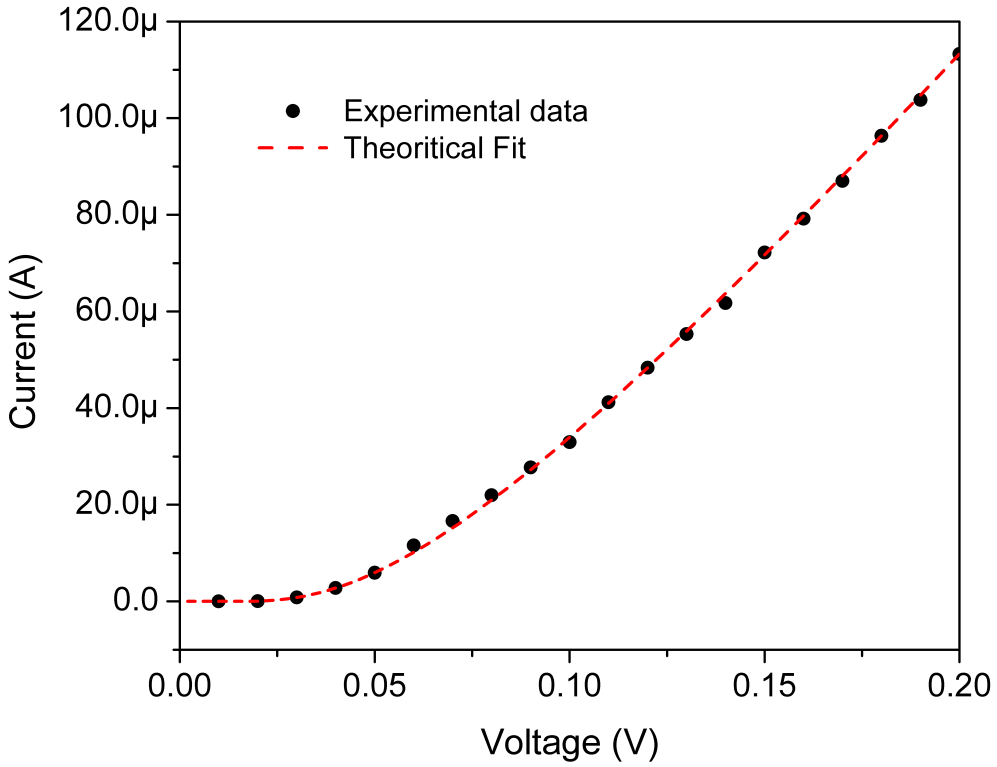

Figure 5.1: I-V characteristics of $NbSe_3$ sample at 120 K. The solid line is the theoretical fit of the dc data to Eqn. (5.26) with $G_a = 11.4\ mmho$, $G_{b1} = 0.94\ mmho$, $G_{b2} = 0.013\ mmho$, $V_{T1} = 0.015\ V$, $V_{T2} = 1.15\ V$, $m = 5.70\ mho$, and $n = 3.82\ mho$.

5.3.2 Non-linear Mixing Response

Mixing experiments provide a very sensitive method of probing the non-linear CDW dynamics. Measurements are performed using a PCI 1 MHz card lock-in amplifier with two (for dc bias) or in some cases with three (for ac bias) signal generators. The samples are mounted on the end of a microstrip transmission line, and cooled with a Helix closed cycle He cryostat, as discussed in Appendix A.2. A Voltage of the form

$$V(t) = V_0 + V_1 \cos \omega_1 t + V_2 \cos \omega_2 t, \tag{5.27}$$

is applied to the sample, inducing current components at the mixing frequency,

$$\begin{aligned} \Delta I_{w_0}(t) &= |\Delta I_0| \cos(\omega_0 t + \phi + \varphi) \\ &= \Delta I_r \cos(\omega_0 t + \phi) + \Delta I_i \sin(\omega_0 t + \phi) \end{aligned} \tag{5.28}$$

where $\Delta I_r = |\Delta I_0| \cos \varphi$ and $\Delta I_i = -|\Delta I_0| \sin \varphi$. The frequency of the induced response is $\omega_0 = \omega_2 - \omega_1$ ($f_0 = f_2 - f_1$) for direct mixing and $\omega_0 = \omega_2 - 2\omega_1$ ($f_0 = f_2 - 2f_1$) for harmonic mixing. Figure A.12 shows a schematic of the experimental setup used to measure the direct and harmonic response. A lock-in technique is used to detect signals generated by the samples at different frequencies. The experimental configuration used for the mixing experiments are discussed in greater detail in Appendix A.5.5. For the ac bias responses, the ac current source is replaced with an additional signal generator ω_{ac} (f_{ac}) to supply an ac bias.

5.3.3 Harmonic Response in the Presence of an ac Bias

Further tests of the tunneling theory involve measuring the scaling parameter α. To do that, harmonic responses of the sample $NbSe_3$ to the frequencies $f_0 = f_2 - 2f_1$ ($f_1 = \ 1MHz$ and $f_0 = 800\ kHz$) are measured with the background ac signal f_{ac} as a parameter. According to PAT theory in Section 5.2.1, an induced intrinsic ac harmonic response at zero bias,

$$\delta I(V'_{ac}) = \sum_{n=-\infty}^{\infty} J_n^2(x)\delta I'(n\alpha\omega_{ac}) \tag{5.29}$$

and high frequencies limit becomes

$$\delta I(V'_{ac}) \approx J_0^2(V_{ac}/\alpha\omega_{ac}). \tag{5.30}$$

Figures 5.2(a) & (b) shows the harmonic response for a $NbSe_3$ sample of length $\ell = 5\ mm$ between the contacts with a ac bias f_{ac}. The data resemble the expected Bessel type oscillations as predicted by PAT theory. Figure 5.2(b) shows both experimental and theoretical current responses at $f_{ac} = 4\ MHz$. Theoretical predictions obtained from $J_0^2(V_{ac}/\alpha\omega_{ac})$ with $\alpha = 1.1\ mV/MHz$, are indicated by solid lines. The theory correctly predicts the mixing response and seen to be in good quantitative agreement as well. The observed behavior gives direct evidence in favor of the photon-assisted tunneling theory of CDW conduction. Substituting α in Eqn. 5.24, the scaling length L_D is found to be 15 Å.

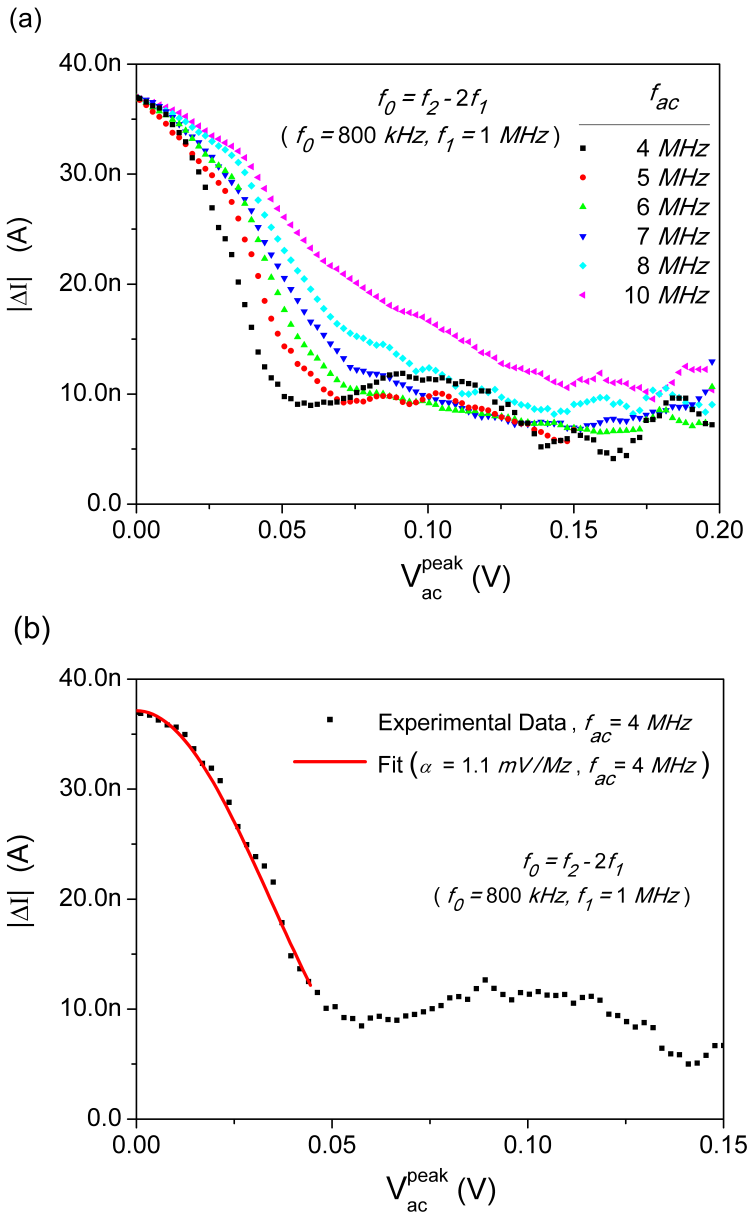

Figure 5.2: Harmonic response ($f_0 = f_1 - 2f_2 = 800\ kHz$) for $NbSe_3$ sample in the presence of an ac bias voltage at 120 K. Dotted lines corresponds to the experimental results. (a) Response for frequency f_1 as a parameter. (b) Response for fixed value of frequecy $f_{ac} = 4\ MHz$. The solid lines are the first order bessal fit of the experimental data to the Eqn. (5.30) with $\alpha = 1.1\ mV/MHz$ and $f_{ac} = 4\ MHz$.

5.3.4 Direct Mixing Response in the Presence of a dc Bias

The PAT theory calculations for the intrinsic direct mixing response are outlined in Appendix A.5.5. The theoretical prediction for the in-phase component of the induced direct mixing current is found to be,

$$\Delta I_r^{dm} = \sum_{n_1 n_2=-\infty}^{\infty} \{J_{n_1}(x_1) J_{n_2}(x_2)[J_{n_1-1}(x_1) J_{n_2+1}(x_2) + J_{n_1+1}(x_1) J_{n_2-1}(x_2)]\ I^{'}(V_2^{'} + n_1\alpha\omega_1 + n_2\alpha\omega_2)\} \tag{5.31}$$

where $x_i = V_i/\alpha\omega_i$. When the aplied ac voltage $V_{1,2}$'s are both small compared to $\alpha\omega_{1,2}$, or compared to the voltage scale of the dc I-V nonlinearity, the result of Eqn. (A.9) reduces in the limit $\omega_0 \to 0$ to

$$\Delta I^{dm} = \Delta I_r^{dm} = \frac{1}{2} V_1 V_2 \left[\frac{I_1 - 2I_0 - I_{-1}}{(\alpha\omega_1)^2}\right] \tag{5.32}$$

where $I_n = I'(V_0' + n\alpha\omega_1)$. When the applied frequencies $\omega_1 \approx \omega_2$ are both sufficiently small, the term in brackets approches the second derivative of the collapsed dc I-V characteristic $d^2I^{'}/dV^{'2}$.

Figures 5.3(a) & (b) show the experimental and theoretical plots of the bias-dependent direct mixing response using a low output frequency f_0= 1 kHz for a $NbSe_3$ sample at applied frequencies $f_1 = 1\ MHz$ and $f_2 = 1.1\ MHz$, with constant ac amplitudes $V_1 = V_2 \cong 2.0\ mV$. Direct mixing experiments show excellent agreement between the PAT theory and the experimental results.

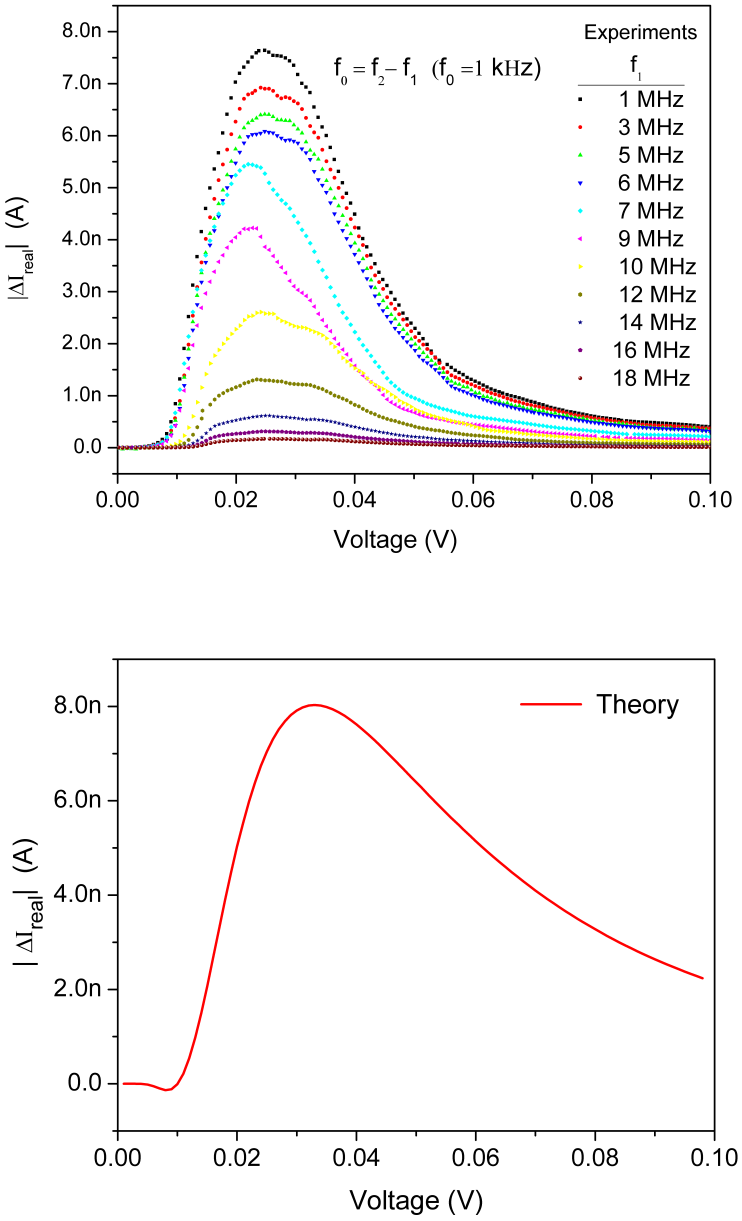

Figure 5.3: Direct mixing response of sample $NbSe_3$ for $f_0 = 1\ kHz$ frequency. (a) Experimental result f_1 as a parameter. (b) Theoretical result for $f_1 = 1\ MHz$. The theoretical predictions is obtained from Eqn. (5.26) and (5.32) with input amplitude $V_1 = V_2 \cong 2.0\ mV$.

5.3.5 Harmonic Mixing Response in the Presence of a dc Bias

The PAT theory calculations for the intrinsic harmonic mixing response are outlined in Appendix A.5.5. In Harmonic mixing, the generated difference frequency is $f_0 = f_2 - 2f_1$. The tunneling theory prediction for the in-phase component of the induced harmonic mixing current is found to be

$$\Delta I_r^{hm} = \sum_{n_1 n_2=-\infty}^{\infty} \{J_{n_1}(x_1) J_{n_2}(x_2)[J_{n_1-2}(x_1) J_{n_2+1}(x_2) + J_{n_1+2}(x_1) J_{n_2-1}(x_2)]\ I^{'}(V_2^{'} + n_1\alpha\omega_1 + n_2\alpha\omega_2)\} \tag{5.33}$$

where $x_i = V_i/\alpha\omega_i$. When the applied ac voltages $V_{1,2}$'s are both small compared to $\alpha\omega_{1,2}$, or to the voltage scale of the dc I-V nonlinearity, the result of Eqn. (A.11) reduces in the limit $\omega_0 \to 0$ to the form

$$\Delta I^{hm} = \Delta I_r^{hm} = \frac{1}{8} V_1^2 V_2 \left[\frac{I_2 - 2I_1 - 2I_{-1} - I_{-2}}{(\alpha\omega_1)^2(\alpha\omega_2)}\right] \tag{5.34}$$

where $I_n = I'(V_0' + n\alpha\omega_1)$. When the applied frequencies $\omega_1 \approx \omega_2$ are both sufficiently small, the term in brackets approaches the third derivative of the collapsed dc I-V characteristic $d^3I^{'}/dV^{'3}$.

Figures 5.4(a) & (b) show the experimental and theoretical plots of the bias-dependent direct mixing response using a low frequency $f_0 = 1\ kHz$ for a $NbSe_3$ sample at applied frequencies $f_1 = 1\ MHz$ and $f_2 = 2.1\ MHz$, with constant ac amplitudes $V_1 = V_2 \cong 5.0\ mV$.

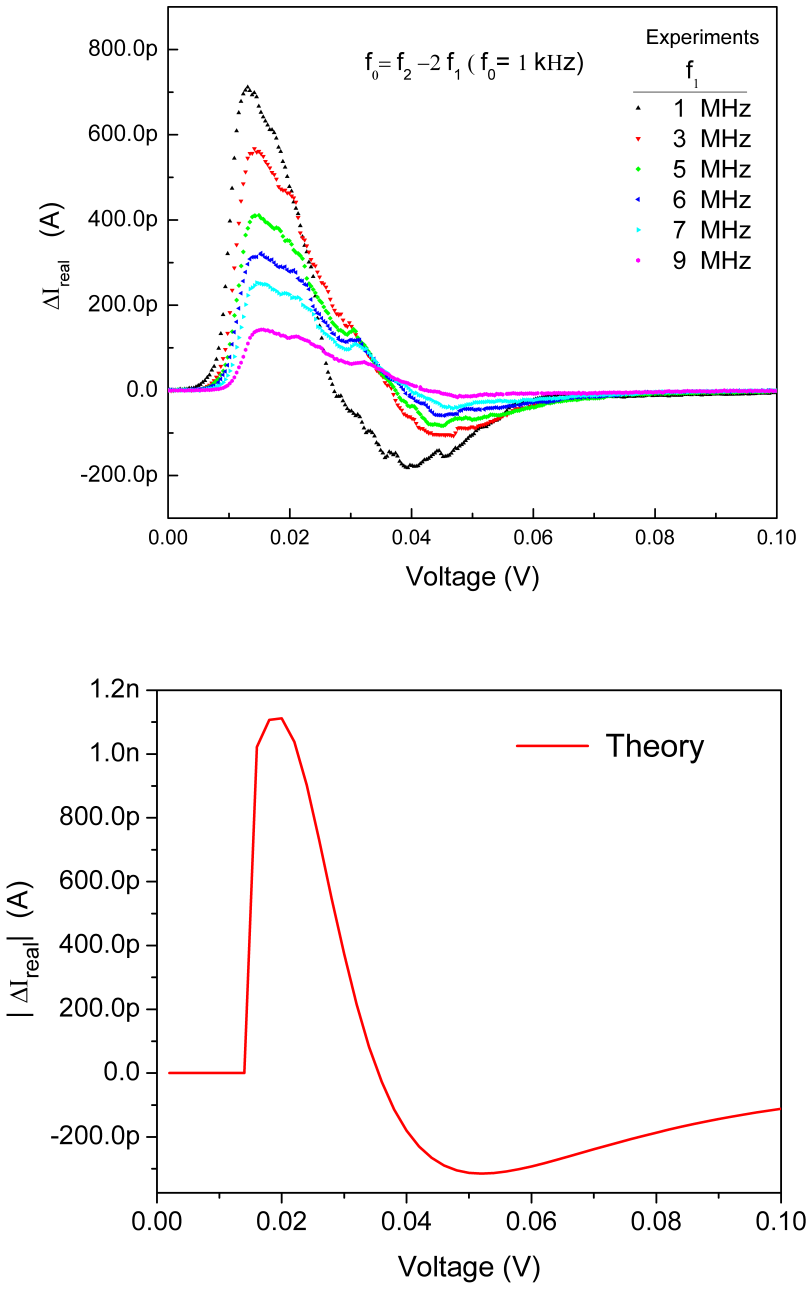

Figure 5.4: Harmonic mixing response of sample $NbSe_3$ for frequency $f_0 = 1\ kHz$. (a) Experimental result for frequency f_1 as a parameter. (b) Theoretical result for the $f_1 = 1\ MHz$. The theoretical predictions is obtained from Eqn. (5.26) and (5.34) with input amplitude $V_1 = V_2 \cong 5.0\ mV$.

5.4 Discussion

At dc bias voltages above threshold, the tunneling theory is found to give a quantitative account of the small signal ac dynamics in the megahertz region using only one adjustable parameter α, the scaling between frequency and voltage. Bessel-type oscillations are observed in small signal ac bias harmonic mixing. Such oscilations are predicted by PAT theory. The agreement between theory and experiment has been found to be excellent for experiments on both direct and harmonic mixing responses as a function of dc bias voltage. The results reported here thus provide a compelling evidence that the quantum tunneling process is important in the depining of charge density waves in $NbSe_3$.

Chapter 6

Conclusion

Density wave transport is one of the very few known cases of correlated transport of macroscopic number of electrons over long distances. The agreement between quantum tunneling theories and experimental results has been found to be excellent for variety of experiments including linear, non-linear, pulse, capacitance/dielectric measurements, direct and harmonic mixing responses as a function of dc bias voltage and in some cases with ac bias voltage.

In conclusion, the results reported here thus provide a compelling evidence that the quantum tunneling process is important in the depining and transport of charge density waves in $NbSe_3$ and related linear chain conductors. Additional area of impact include improved understanding of other correlated electron systems, flux vortex nucleation [80], and tunneling in quantum cosmology [62, 81]. Finally, the implications of the results on the thesis could impact fields as diverse as cosmology, condensed matter physics, quantum computation, and biophysics.

Bibliography

[1] L. M. Falicov, "Quantum tunneling phenomena, John Bardeen, and the tunneling hamiltonian," *Journal of Superconductivity*, vol. 4, pp. 331–336, 1991.

[2] J. Bardeen, "Tunnelling from a many-particle point of view," *Phys. Rev. Lett.*, vol. 6, pp. 57–59, Jan 1961.

[3] M. H. Cohen, L. M. Falicov, and J. C. Phillips, "Superconductive tunneling," *Phys. Rev. Lett.*, vol. 8, pp. 316–318, Apr 1962.

[4] B. D. Josephson, "Possible new effects in superconductive tunnelling," *Physics Letters*, vol. 1, no. 7, pp. 251–253, 1962.

[5] S. Coleman, "Fate of the false vacuum: Semiclassical theory," *Phys. Rev. D*, vol. 15, pp. 2929–2936, May 1977.

[6] S. Coleman, "Erratum: Fate of the false vacuum: Semiclassical theory," *Phys. Rev. D*, vol. 16, pp. 1248–1248, Aug 1977.

[7] C. G. Callan and S. Coleman, "Fate of the false vacuum. II. first quantum corrections," *Phys. Rev. D*, vol. 16, pp. 1762–1768, Sep 1977.

[8] J. B. Hartle and S. W. Hawking, "Wave function of the universe," *Phys. Rev. D*, vol. 28, pp. 2960–2975, Dec 1983.

[9] A. Vilenkin, "Quantum creation of universes," *Phys. Rev. D*, vol. 30, pp. 509–511, Jul 1984.

[10] A. R. Brown, S. Sarangi, B. Shlaer, and A. Weltman, "Enhanced brane tunneling and instanton wrinkles," *Phys. Rev. Lett.*, vol. 99, no. 161601, pp. 1–4, Oct 2007.

[11] P. J. Steinhardt and N. Turok, "Why the cosmological constant is small and positive," *Science*, vol. 312, p. 1180, 2006.

[12] I. Y. Kobzarev, L. B. Okun, and M. B. Voloshin, "Bubbles in Metastable Vacuum," *Sov. J. Nucl. Phys.*, vol. 20, pp. 644–646, 1975.

[13] P. Monçeau, N. P. Ong, A. M. Portis, A. Meerschaut, and J. Rouxel, "Electric field breakdown of charge density wave-induced anomalies in $NbSe_3$," *Phys. Rev. Lett.*, vol. 37, pp. 602–606, Sep 1976.

[14] R. M. Fleming, D. E. Moncton, and D. B. McWhan, "X-ray scattering and electric field studies of the sliding mode conductor $NbSe_3$," *Phys. Rev. B*, vol. 18, pp. 5560–5563, Nov 1978.

[15] J. H. Ross, Z. Wang, and C. P. Slichter, "NMR study of the structure and motion of charge density waves in $NbSe_3$," *Phys. Rev. Lett.*, vol. 56, pp. 663–666, Feb 1986.

[16] G. Grüner, A. Zawadowski, and P. M. Chaikin, "Nonlinear conductivity and

noise due to charge density wave depinning in $NbSe_3$," *Phys. Rev. Lett.*, vol. 46, pp. 511–515, Feb 1981.

[17] H. Fukuyama and P. A. Lee, "Dynamics of the charge density wave. I. impurity pinning in a single chain," *Phys. Rev. B*, vol. 17, pp. 535–541, Jan 1978.

[18] P. A. Lee and T. M. Rice, "Electric field depinning of charge density waves," *Phys. Rev. B*, vol. 19, pp. 3970–3980, Apr 1979.

[19] J. Bardeen, "Tunneling theory of charge density wave depinning," *Phys. Rev. Lett.*, vol. 45, pp. 1978–1980, Dec 1980.

[20] K. Maki, "Creation of soliton pairs by electric fields in charge density wave condensates," *Phys. Rev. Lett.*, vol. 39, pp. 46–48, Jul 1977.

[21] A. Maiti and J. H. Miller, "Theory of charge density wave tunneling," *Phys. Rev. B*, vol. 43, pp. 12205–12215, May 1991.

[22] I. Krive and A. Rozhavsky, "On the nature of threshold electric field in quasi-one-dimensional commensurate charge density waves," *Solid State Communications*, vol. 55, no. 8, pp. 691–694, 1985.

[23] I. S. Krive and A. S. Rozhavskii, "Macroscopic quantum tunneling of a three-dimensional charge density wave in an above-threshold electric field," *Sov. Phys.*, vol. 69, p. 552, 1989.

[24] Y. I. Latyshev, O. Laborde, P. Monceau, and S. Klaumünzer, "Aharonov-Bohm effect on charge density wave (CDW) moving through columnar defects in $NbSe_3$," *Phys. Rev. Lett.*, vol. 78, pp. 919–922, Feb 1997.

[25] M. Tsubota, K. Inagaki, and S. Tanda, "Quantum interference of charge density waves: Evidence for topological crystals of TaS_3," *Physica B: Condensed Matter*, vol. 404, no. 34, pp. 416–418, 2009.

[26] E. N. Bogachek, I. V. Krive, I. O. Kulik, and A. S. Rozhavsky, "Instanton Aharonov-Bohm effect and macroscopic quantum coherence in charge density wave systems," *Phys. Rev. B*, vol. 42, pp. 7614–7617, Oct 1990.

[27] J. H. Miller, R. E. Thorne, W. G. Lyons, J. R. Tucker, and J. Bardeen, "Dynamics of charge density waves in orthorhombic TaS_3," *Phys. Rev. B*, vol. 31, pp. 5229–5243, Apr 1985.

[28] A. Zettl and G. Grüner, "Phase coherence in the current-carrying charge density wave state: ac-dc coupling experiments in $NbSe_3$," *Phys. Rev. B*, vol. 29, pp. 755–767, Jan 1984.

[29] W. yu Wu, L. Mihaly, and G. Grüner, "Dielectric response enhancement in the current carrying cdw state," *Solid State Communications*, vol. 55, no. 8, pp. 663–666, 1985.

[30] G. Grüner, "The dynamics of charge density waves," *Rev. Mod. Phys.*, vol. 60, pp. 1129–1181, Oct 1988.

[31] P. B. Littlewood, "Sliding charge density waves: A numerical study," *Phys. Rev. B*, vol. 33, pp. 6694–6708, May 1986.

[32] S. N. Coppersmith and D. S. Fisher, "Threshold behavior of a driven incommensurate harmonic chain," *Phys. Rev. A*, vol. 38, pp. 6338–6350, Dec 1988.

[33] O. Narayan and A. A. Middleton, "Avalanches and the renormalization group for pinned charge density waves," *Phys. Rev. B*, vol. 49, pp. 244–256, Jan 1994.

[34] N. P. Ong, "Review of the Fröhlich sliding mode in $NbSe_3$," *Canadian Journal of Physics*, vol. 60, no. 5, pp. 757–765, 1982.

[35] G. Grüner and A. Zettl, "Charge density wave conduction: A novel collective transport phenomenon in solids," *Physics Reports*, vol. 119, no. 3, pp. 117–232, 1985.

[36] G. Grüner, *Density Waves in Solids*. Addison Wesley, Reading, MA, 1994.

[37] R. E. Peierls, *Qunatum Theory of Solids*. Oxford University Press, Oxford, 1953.

[38] H. Fröhlich, "On the theory of superconductivity: The one-dimensional case," *Proceedings of the Royal Society of London. Series A. Mathematical and Physical Sciences*, vol. 223, no. 1154, pp. 296–305, 1954.

[39] C. D. Malliakas, *Charge density waves and structural modulations in polytelluride compounds*. PhD thesis, Michigan State University, 2008.

[40] J. Schrieffer, *Theory of Superconductivity*. Addison-Wesley, Reading, 1983.

[41] E. J. Woll and W. Kohn, "Images of the fermi surface in phonon spectra of metals," *Phys. Rev.*, vol. 126, pp. 1693–1697, Jun 1962.

[42] M. Rice and S. Strssler, "Theory of a quasi-one-dimensional band-conductor," *Solid State Communications*, vol. 13, no. 1, pp. 125–128, 1973.

[43] D. Allender, J. W. Bray, and J. Bardeen, "Theory of fluctuation superconductivity from electron-phonon interactions in pseudo-one-dimensional systems," *Phys. Rev. B*, vol. 9, pp. 119–129, Jan 1974.

[44] R. E. Thorne, "Charge density wave conductors.," *Physics Today*, vol. 49, no. 5, p. 42, 1996.

[45] E. Dizhur, M. Il'aina, and S. Zaitsev-Zotov, "Metal-insulator transition in whiskers of the NbS_3; quasi-one-dimensional conductor under pressure," *JETP Letters*, vol. 86, pp. 132–134, 2007.

[46] A. Meerschaut and J. Rouxel, "Le seleniure $NbSe_3$: Obtention et structure," *Journal of the Less Common Metals*, vol. 39, no. 2, pp. 197–203, 1975.

[47] J. L. Hodeau, M. Marezio, C. Roucau, R. Ayroles, A. Meerschaut, J. Rouxel, and P. Monceau, "Charge density waves in $NbSe_3$ at 145 K: crystal structures, X-ray and electron diffraction studies," *Journal of Physics C: Solid State Physics*, vol. 11, no. 20, p. 4117, 1978.

[48] P. Monceau, J. Richard, and M. Renard, "Charge density wave motion in $NbSe_3$. I. studies of the differential resistance $\frac{\mathrm{dv}}{\mathrm{di}}$," *Phys. Rev. B*, vol. 25, pp. 931–947, Jan 1982.

[49] R. M. Fleming and C. C. Grimes, "Sliding-mode conductivity in $NbSe_3$: Observation of a threshold electric field and conduction noise," *Phys. Rev. Lett.*, vol. 42, pp. 1423–1426, May 1979.

[50] J. W. Brill, N. P. Ong, J. C. Eckert, J. W. Savage, S. K. Khanna, and R. B. Somoano, "Impurity effect on the fröhlich conductivity in $NbSe_3$," *Phys. Rev. B*, vol. 23, pp. 1517–1526, Feb 1981.

[51] G. Grüner, L. C. Tippie, J. Sanny, W. G. Clark, and N. P. Ong, "Frequency-dependent conductivity in $NbSe_3$," *Phys. Rev. Lett.*, vol. 45, pp. 935–938, Sep 1980.

[52] J. Richard, R. Thorne, W. Lyons, J. M. Jr., and J. Tucker, "Mixing experiments in $NbSe_3$," *Solid State Communications*, vol. 52, no. 2, pp. 183–187, 1984.

[53] T. C. Jones, X. Wu, C. R. Simpson, J. A. Clayhold, and J. P. McCarten, "Pulse-duration memory effect in $NbSe_3$ and comparison with numerical simulations of phase organization," *Phys. Rev. B*, vol. 61, pp. 10066–10075, Apr 2000.

[54] J. Richard, P. Monceau, and M. Renard, "Charge density wave motion in $NbSe_3$. II. dynamical properties," *Phys. Rev. B*, vol. 25, pp. 948–970, Jan 1982.

[55] L. Sneddon, M. C. Cross, and D. S. Fisher, "Sliding conductivity of charge density waves," *Phys. Rev. Lett.*, vol. 49, pp. 292–295, Jul 1982.

[56] R. E. Thorne, J. R. Tucker, and J. Bardeen, "Experiment versus the classical model of deformable charge density waves: Interference phenomena and mode locking," *Phys. Rev. Lett.*, vol. 58, pp. 828–831, Feb 1987.

[57] K. Maki, "Soliton pair creation and low-temperature electrical conductivity of charge density wave condensates," *Phys. Rev. B*, vol. 18, pp. 1641–1646, Aug 1978.

[58] J. Bardeen, "Depinning of charge density waves by quantum tunneling," *Physica Scripta*, vol. 1989, no. T27, p. 136, 1989.

[59] J. Bardeen, "Theory of non-ohmic conduction from charge density waves in $NbSe_3$," *Phys. Rev. Lett.*, vol. 42, pp. 1498–1500, May 1979.

[60] R. E. Thorne, J. H. Miller, W. G. Lyons, J. W. Lyding, and J. R. Tucker, "Macroscopic quantum tunneling in quasi one-dimensional metals. I. experiment," *Phys. Rev. Lett.*, vol. 55, pp. 1006–1009, Aug 1985.

[61] J. Bardeen, "Superconductivity and other macroscopic quantum phenomena," *Physics Today*, vol. 43, no. 12, pp. 25–31, 1990.

[62] E. P. Tryon, "Is the universe a vacuum fluctuation?," *Nature*, vol. 246, pp. 396–397, December 1973.

[63] A. O. Caldeira and A. J. Leggett, "Influence of dissipation on quantum tunneling in macroscopic systems," *Phys. Rev. Lett.*, vol. 46, pp. 211–214, Jan 1981.

[64] J. H. Miller, A. I. Wijesinghe, Z. Tang, and A. M. Guloy, "Correlated quantum transport of density wave electrons," *Phys. Rev. Lett.*, vol. 108, p. 036404, Jan 2012.

[65] O. Dias and J. Lemos, "False vacuum decay: Effective one-loop action for pair creation of domain walls," *Journal of Mathematical Physics*, vol. 42, pp. 3292–3298, Aug 2001.

[66] J. H. Miller, C. Ordóñez, and E. Prodan, "Time-correlated soliton tunneling in

charge and spin density waves," *Phys. Rev. Lett.*, vol. 84, pp. 1555–1558, Feb 2000.

[67] J. John H. Miller, "Quantum decay of the 'false vacuum' and pair creation of soliton domain walls," *AIP Conference Proceedings*, vol. 1327, no. 1, pp. 434–438, 2011.

[68] Sidney and Coleman, "Soliton pair creation in the massive schwinger model," *Annals of Physics*, vol. 101, no. 1, pp. 239–246, 1976.

[69] C. B. Duke, *Tunneling in Solids.* Academic Press, New York, 1969.

[70] T. D. Cohen and D. A. McGady, "Schwinger mechanism revisited," *Phys. Rev. D*, vol. 78, no. 036008, pp. 1–6, Aug 2008.

[71] K. Likharev, "Single-electron devices and their applications," *Proceedings of the IEEE*, vol. 87, pp. 606–632, Apr 1999.

[72] D. V. Averin and K. K. Likharev, "Coulomb blockade of single-electron tunneling, and coherent oscillations in small tunnel junctions," *Journal of Low Temperature Physics*, vol. 62, pp. 345–373, 1986.

[73] M. S. R. P. Feynman, R. B. Leighton, *The Feynman Lectures on Physics.* Addison-Wesley, Reading, Massachusetts, 1965.

[74] T. C. Jones, X. Wu, C. R. Simpson, J. A. Clayhold, and J. P. McCarten, "Pulse-duration memory effect in $NbSe_3$ and comparison with numerical simulations of phase organization," *Phys. Rev. B*, vol. 61, pp. 10066–10075, Apr 2000.

[75] G. Mihaly and P. Beauchene, "Sliding charge density waves without damping: Possible fröhlich superconductivity in blue bronze," *Solid State Communications*, vol. 63, no. 10, pp. 911–914, 1987.

[76] A. H. Dayem and R. J. Martin, "Quantum interaction of microwave radiation with tunneling between superconductors," *Phys. Rev. Lett.*, vol. 8, pp. 246–248, Mar 1962.

[77] P. K. Tien and J. P. Gordon, "Multiphoton process observed in the interaction of microwave fields with the tunneling between superconductor films," *Phys. Rev.*, vol. 129, pp. 647–651, Jan 1963.

[78] S. P. Kashinje, "Theory of photon-assisted tunneling in the transition between the quantum mechanical and classical limits," *Physica Status Solidi*, vol. 207, no. 2, p. 463, 1998.

[79] J. Tucker, "Quantum limited detection in tunnel junction mixers," *Quantum Electronics, IEEE Journal of*, vol. 15, pp. 1234–1258, Nov 1979.

[80] J. H. Miller, Jr. and A. I. Wijesinghe, "Magnetic blockade mechanism for quantum nucleation of superconducting vortex-antivortex pairs in zero external magnetic field," *ArXiv e-prints*, Oct. 2011.

[81] F. Dowker, J. P. Gauntlett, D. A. Kastor, and J. Traschen, "Pair creation of dilaton black holes," *Phys. Rev. D*, vol. 49, pp. 2909–2917, Mar 1994.

Appendix A

A.1 Electrode Design and Fabrication

Electrode pattern is constructed on alumina substrate using thin film microfabrication techniques. The complete fabrication process is shown in Fig. A.1. Prior to the fabrication process, the alumina substrate is immersed in acetone and methanol to remove the organic impurities, and rinsed in distilled water. The alumina substrate is then placed on a hot plate (100^0 C) for 1 hour to remove water and all the other remaining solvents. After that, it is placed on a vacuum spindle spin coater and a liquidous photoressist (Shipley 1813) is applied to the center of it. The substrate is then rapidly accelerated up to a constant speed, which is maintained for 30 s. Spin speed is generally in the range of 1000-10000 rpm to coat a uniform film about 0.5-1 μm thick. After spinning, the substrate is "soft-backed" (typically at 100- 120^0C for 1 to 2 min) to remove solvent from the photoresist and to increase resist adhesion to the substrate. Next, the substrate is aligned with respect to the mask in a mask aligning system, and the photoresist is exposed to ultraviolet light.

Photoresist development is usually done by flooding the substrate with the developer (MF212 diluted with 1:1 DH_20) solution. The substrate is then rinsed and dried. After the development, "postbaking" at approximately 100-180^{0}C may be required to increase the adhesion of the resist to the substrate.

Sputtering technique is used for the deposition of a thin layer of gold. In general, a thin layer of titanium with a thickness of 50 Å is first deposited by sputtering, to enhance the adhesion between the alumina substrate and the gold layer. The deposition sequence of the two metals is selected in such a way that the most stable metal would be deposited first. For both titanium and gold sputtering, pressurized argon (2x10^{-4} Torr) with a 7.5 mA beam current is used. To deposit a 50 Å thick film of titanium and a 2500 Å thick film of gold, the sputtering times are 30 and 45 minutes respectively. After the deposition process, the remaining soluble positive resist underneath the deposited material is dissolved by keeping inside the acetone solution for 2 to 3 hours. Finally, the alumina substrate is rinsed and dried to remove the remaining solvent.

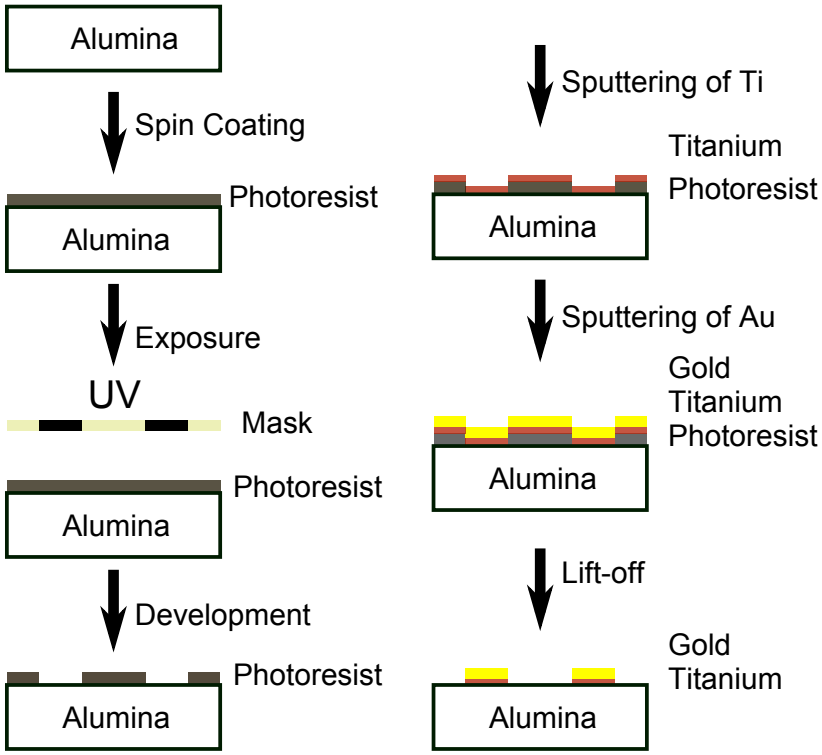

Figure A.1: Fabrication process of the gold microelectrode.

A.2 Low Temperature Setup

For the low temperature measurement, a CTI cryogenics model 22 closed cycle variable temperature refrigerator is used. This allows the sample to cool down to 12 K, under high vacuum. The cryostat is connected to the water cooled CTI 8200 compressor that compresses and expands Helium gas in a closed loop. During the expansion phase of each cycle, heat is removed from the cold head. A diode thermometer and a 50 Ω heater, which are installed on the cold head, are connected to a Lakeshore 325 temperature controller. The sample temperature can vary between 12 K to 350 K. The accuracy of the temperature is ±1 mK. The low temperature experimental setup is shown schematically in Fig. A.2.

Before beginning the cool down process, the shroud is evacuated using a fully automatic Blazer turbo molecular pump and a pressure of $1X10^{-4}$ Torr is quickly achieved. Better vacuum level ensures shorter cool down time and lower minimum temperature. Once the vacuum is established, the compressor and the closed cycle refrigerator work together, extracting heat from the cold head during the expansion phase of the Helium gas, and the system reaches the lowest temperature (roughly 12 K). The heater controls by Lakeshore 325 allows varying and measuring the temperature accurately.

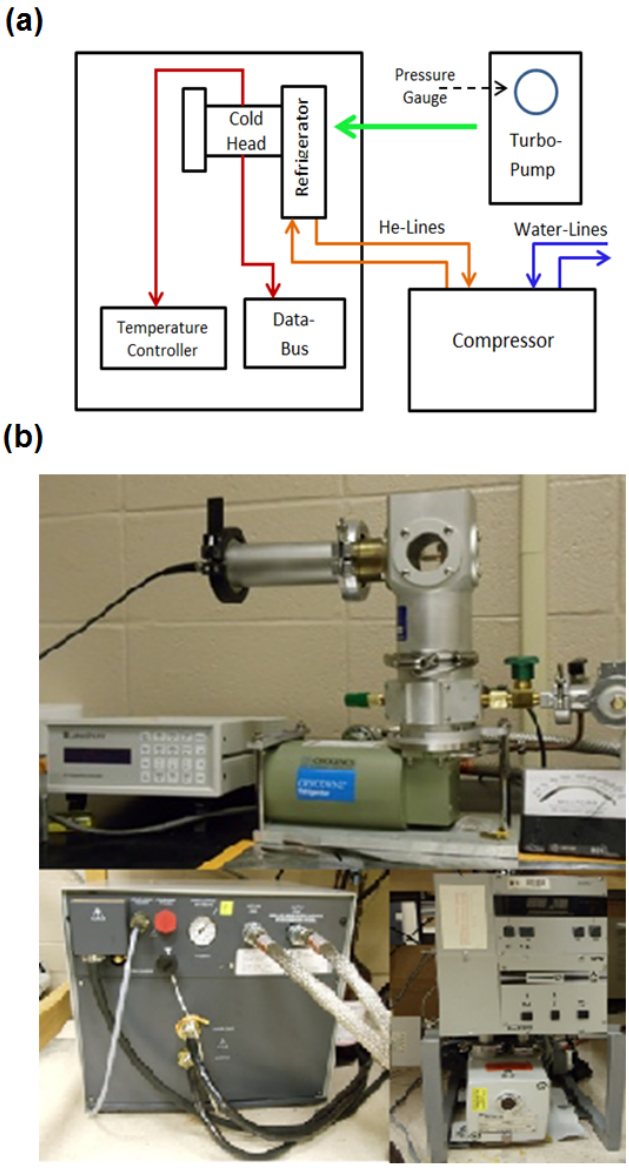

Figure A.2: Low temperature system. (a) Schematic diagram. (b) Instrument setup.

A.3 Sample Mounting

A.3.1 Low Frequency Measurement

In order to perform low frequency measurement at low temperature, 16 coaxial cables are soldered to the Janis vacuum shroud through vacuum compatible connector feedthroughs. The other ends of the cables are soldered to the gold spring contact probes mounted on a Teflon plate in such a way that they touch the electrode pads to supply the electrical connections to the sample. The sample holder is designed to accommodate several electrode connections on which the sample is directly mounted. Figure A.3(a) shows the electrode pattern used to mount the samples and Fig. A.3(b) shows the SEM image of the $NbSe_3$ crystal on top of the fabricated electrode. The electrodes are 0.1 mm thick and the spacing between the subsequent electrodes are 0.5 mm.

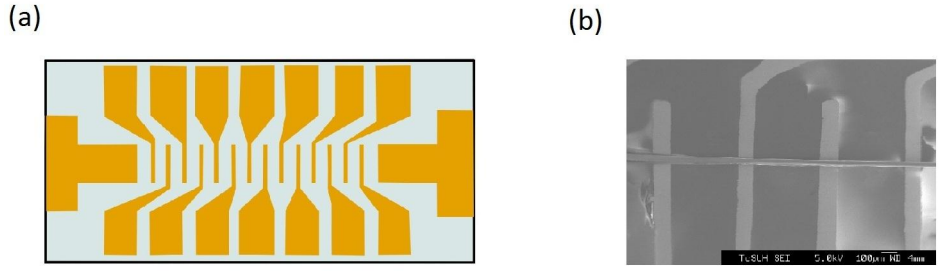

Figure A.3: (a) Schematic of the gold electrode pattern on alumina substrate with dimensions of 10 mm $\times$ 25 mm. The electrodes are 0.1 mm thick and the spacing between the subsequent electrodes are 0.5 mm. (b) SEM image of the $NbSe_3$ crystal on top of the gold microelectrode.

Sample crystals are mounted directly on top of the lithographically patterned gold electrode configuration on alumina substrate, using quick drying silver paint.

The bottom of the electrode configuration (alumina substrate) is mounted on top of the cold head of the cryostat and a small amount of thermally conductive grease is applied in between the two surfaces to ensure a good thermal conduction.

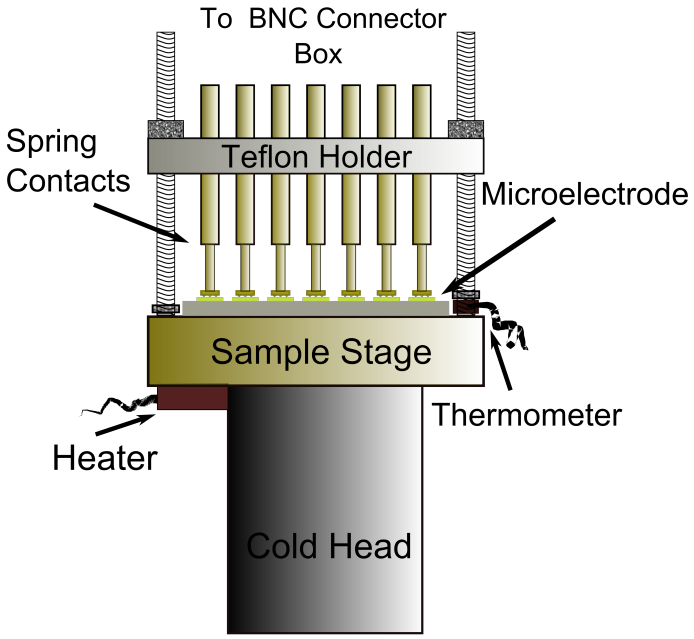

Figure A.4: Low frequency measurement sample holder and arrangement.

A.3.2 High Frequency Measurement

In order to perform high frequency measurement at low temperature, two semi-rigid stainless steel coaxial cables are run in to the Janis through vacuum compatible SMA rf feedthroughs. The sample holder is designed to accommodate two microstrip lines on which the sample is directly mounted. Figure A.5 shows the microstrip used to mount the samples. The substrate is 0.5 mm thick alumina with a dielectric constant of ϵ_r= 9.8. The 0.5 mm microstripline is fabricated on the alumina substrate using photolithographic patterning techniques and wet chemical etching. Sample

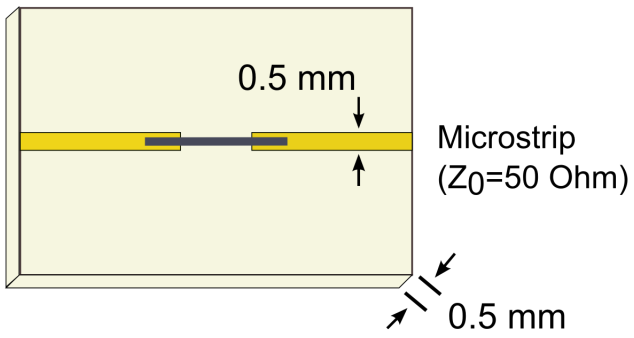

Figure A.5: Schematic of the microstrip line (0.5 mm) on alumina substrate with dimensions of 10 $mm \times 10$ mm.

crystals are mounted directly on top of the lithographically patterned microstrip electrode on alumina substrate, using quick drying silver paint. The bottom of the microstrip line is mounted on top of the rf feed through sample holder of the cryostat and a small amount of thermally conductive grease is applied in between the two surfaces to ensure a good thermal conduction.

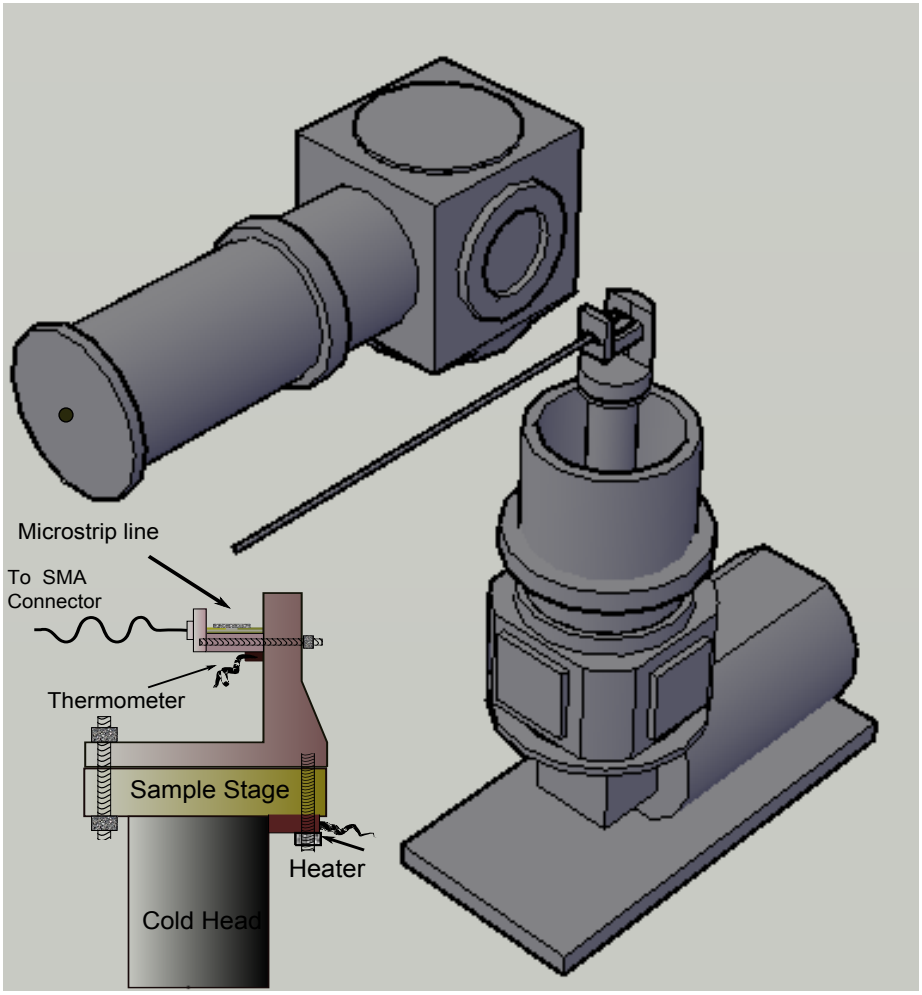

Figure A.6: High frequency measurement sample holder and arrangement.

A.4 Computer Interface: LabVIEW

Computer interfacing allows precise control of the instruments and ease of recording a large number of data in short time intervals. In this work, LabVIEW (Short for Laboratory Virtual Instrumentation Engineering Workbench) software is used for data acquisition. LabVIEW is a platform and a development environment for a visual programing language from National Instruments. Originally released for the Apple Macintosh in 1986, LabVIEW is commonly used for data acquisition, instrument control, and industrial automation.

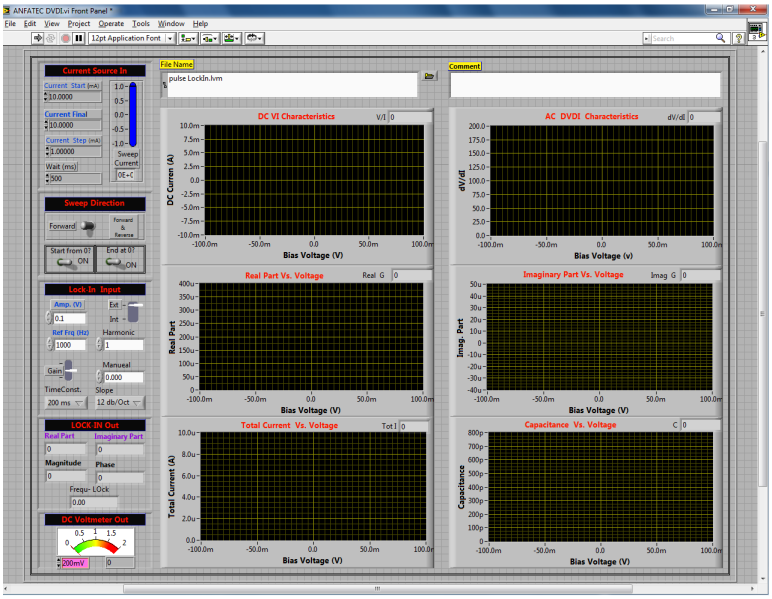

Figure A.7: Front panel of the labVIEW program.

The programming language used in labVIEW is a data flow language. Execution is determined by the structure of a graphical block diagram, on which the programmer connects different function-nodes by drawing wires. Figures. A.7 & A.8 show

the front panel and block diagram of the labVIEW program used in differential resistance, dielectric, and mixing experiments.

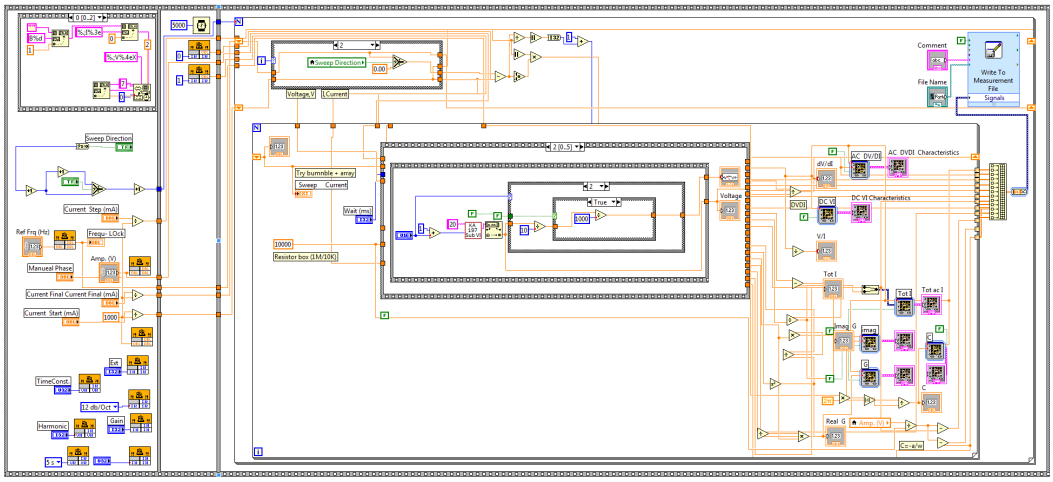

Figure A.8: Block diagram of the labVIEW program.

The advantage of using LabVIEW over other development environments is its extensive support for accessing the instrumentation hardware. Drivers for many different types of instruments are included or are available for download. Many libraries, with a large number of functions for data acquisition, signal generation, analysis, mathematics, statistics, *etc.*, along with numerous graphical interface elements are provided with LabVIEW. The provided drivers, interface elements and functions save the program development time. Even people with limited coding experience can write programs and deploy test solutions in a reduced time frame when compared to more conventional programming systems.

A.5 Electrical Measurements

Electrical property measurement techniques include direct current (dc) current-voltage I-V, differential resistance, dielectric, and pulse measurements. A description for each of these experimental setups will be given in detail below.

A.5.1 dc Measurement

The experimental set up for the dc I-V measurement system consists of a Keithley model 220 programmable current source,a Keithley model 182 sensitive voltmeter, and a pc interfaced with GPIB cable and IEEE interface card. I-V characteristics of the sample are found by using a standard four elecroedes technique, by measuring the corresponding voltage drop in inner two electrodes to current applied to the outer electrodes, using the ammeter and the voltmeter controlled via the LabVIEW software.

A.5.2 Differential Resistance Measurement

The experimental setup for the differential resistance measurement consists of a SR-830 DSP lock-in amplifier from Standford research system, a Keithley model 200 programmable current source, two 100 kΩ resistors, and a pc interfaced with GPIB cable and IEEE interface card. The circuit diagram for the differential resistance measurement is shown in Fig. A.9.

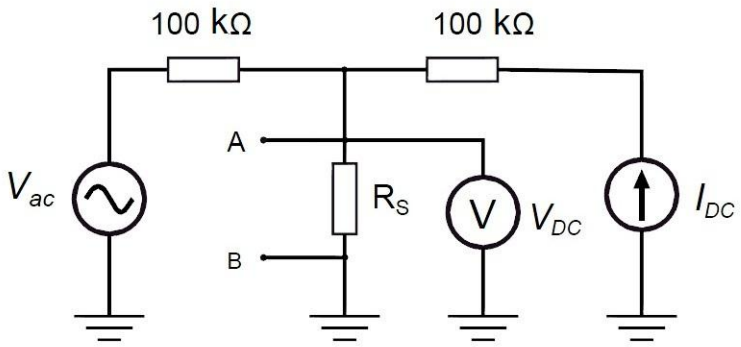

Figure A.9: Schematic of the cuitircuit diagram for the differential resistance (dV/dI) measurement. I_{DC} is the dc current source, V_{DC} is the voltmeter, V_{ac} is the ac signal output of the lock-in amplifier, and R_S is the sample under test. Ports A and B are connected to the lock-in amplifier in differential mode.

The measurement is performed by placing the sample in series with two 100 kΩ resistors such that resistance of the sample is much less than 100 kΩ ($>> R_{sample}$). Differential resistance (dV/dI) characteristics of the sample are measured by applying a low frequency (50-500 Hz), a small ac current, and a dc bias to the sample in a current bias configuration, measuring the voltage drop of the sample in lock-in

differential mode. Thus, a current of the form

$$I(t) = I_0 + \delta I_0 \cos(\omega t) \tag{A.1}$$

is applied to the sample. The sample nonlinearity induces a voltage response of the form

$$V(t) = V_{dc} + \delta V_1 \cos(\omega t) + \delta V_2 \cos(2\omega t) + ... \quad . \tag{A.2}$$

The low frequency voltage can be calculated by making a Taylor series expansion about the dc current bias point, where

$$\begin{aligned} V(t) &= V[I(t)] \\ &= V(I_0) + (\delta I_0 \cos \omega t) \left(\frac{dV}{dI}\right)_{I=I_0} \\ &\quad + \frac{1}{2}(\delta I_0 \cos \omega t)^2 \left(\frac{d^2V}{dI^2}\right)_{I=I_0} + ... \quad . \end{aligned} \tag{A.3}$$

From Eqn. (A.3), the ω component of the induced voltage can be found:

$$\delta V \cong (\delta I_0) \left(\frac{dV}{dI}\right)_{I=I_0} . \tag{A.4}$$

Hence, the dV/dI component of the sample can be measured simply from Eqn. (A.4).

A.5.3 Dielectric Measurement

The experimental setup for the dielectric constant measurement consists of a 7265 DSP lock-in amplifier from Signal Recovery, a Keithley model 200 programmable current source, a variable resistor, two 1 MΩ resistors, a 10 kΩ resistor, and a pc interfaced with GPIB cable and IEEE interface card. The ac admittance is measured using a bridge circuit as shown in Fig. A.10.

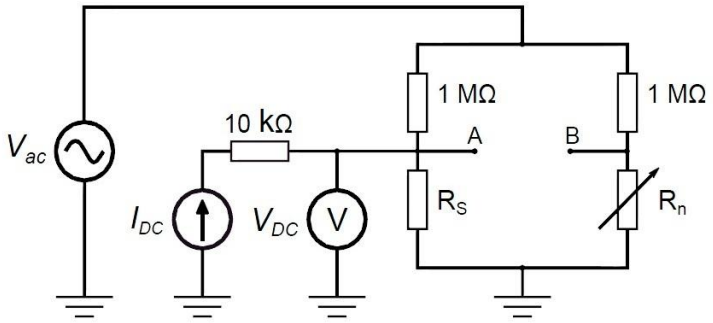

Figure A.10: Schematic of the bridge circuit for ac admittance (including capacitance) measurements. I_{DC} is the dc current source, V_{DC} is the voltmeter, V_{ac} is the ac signal output of the lock-in amplifier, R_S is the sample under test, and R_n is the variable resistor adjusted so that the sample's normal resistance to zero out the real part of the ac response at zero bias. Ports A and B are connected to the lock-in amplifier in differential mode.

The measurement is performed using a resistive bridge circuit in order to cancel out the normal carrier component of the conductivity. Then, the real and imaginary parts of the voltage are measured at the points A and B from the lock-in differential mode, while changing the bias current from the current source.

A.5.4 Pulse Measurement

The experimental set up for the pulse measurement system consists of a signal generator, an oscilascope, a 100 kΩ resistor, and a pc interfaced with GPIB cable and IEEE interface card. Figure A.11 shows the circuit diagram for the pulse measurement circuit.

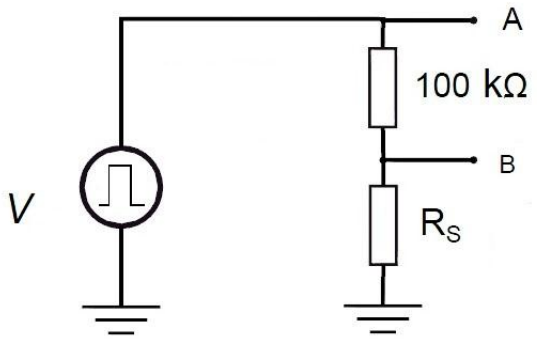

Figure A.11: Schematic of the pulse measurement circuit. V is the pulse generator, R_S is the sample under test in series with a 100 kΩ resistor. Ports A and B are connected to the input channels of the oscilascope.

The measurement is performed by placing the sample in series with a 100 kΩ resistor such that resistance of the sample is much less than 100 kΩ ($>>$ R_{sample}). The input and output of the voltage pulse are observed at the points A and B from the oscilascope 2-channel mode.

A.5.5 Non-linear Mixing Measurement

The experimental setup for the non-linear mixing technique consists of an AMU 2.4 - 1 MHz PCI-Bus lock-in amplifier from Anfatec Instruments AG, three signal generators from Agilant technologies, a Keithley model 200 programmable current source, three 100 kΩ resistors, and a pc interfaced with GPIB cable and IEEE interface card. Figure A.12 shows the schematic of the mixer configuration.

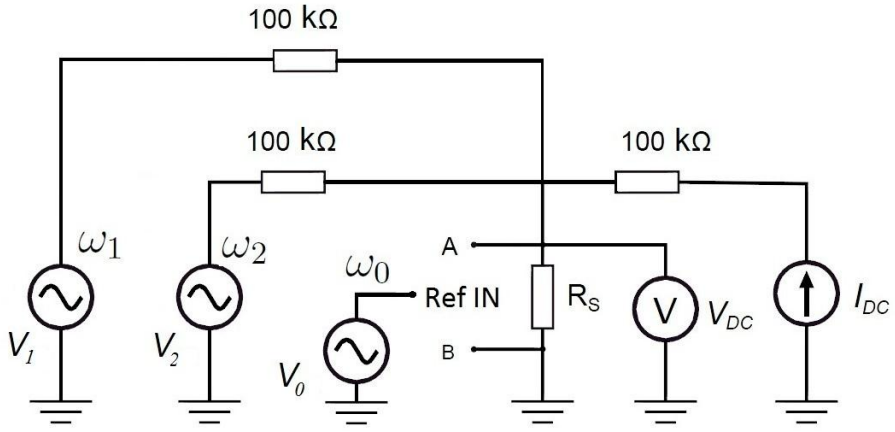

Figure A.12: Schematic of the bridge circuit diagram of the direct and harmonic mixing experiment configuration. I_{DC} is the dc current source, V_{DC} is the voltmeter, V_1, V_2, and V_0 are the ac signal sources with frequencies ω_1, ω_2, and ω_0, and R_S is the sample under test. Direct mixing signal is generated at the difference frequency $\omega_0 = \omega_2 - \omega_1$, while a harmonic mixing signal is generated at $\omega_0 = \omega_2 - 2\omega_1$. Ports A and B are connected to the lock-in amplifier in differential mode to detect the generated mixing current at different frequencies.

The measurement is performed by connecting two signal generators (phase locked with each other) and applying a voltage V_1 and V_2 to the sample of the form

$$V(t) = V_0^{'} + V_1 \cos(\omega_1 t + \phi_1) + V_2 \cos(\omega_2 t + \phi_2) \tag{A.5}$$

where $\phi = (\phi_2 - \phi_1)$ is the constant phase shift between the two signal generators and V_0 is the dc bias voltage. A direct mixing signal is generated at the difference frequency $\omega_0 = \omega_2 - \omega_1$, while a harmonic mixing signal is generated at $\omega_0 = \omega_2 - 2\omega_1$.

A lock-in amplifier is used to detect the generated ac mixing current $\Delta I \cos(\omega t + \phi + \varphi)$ at the difference frequency ω_0, where φ is the internal phase shift due to the CDW response. The Fourier transform of the quantum mechanical phase factor in this case is

$$W(\omega^{'}) = J_{n1}(x_1)\delta(\omega^{'} - n_1\omega_1) + J_{n_2}(x_2)\delta(\omega^{'} - n_2\omega_2) \tag{A.6}$$

where $x_i = V_i/\alpha\omega_i$. The third signal generator phase locked with others send the desired output frequency ω_0 to the reference input of the lock-in amplifier. The induced mixing signal of the sample is simultaneously fed to the signal input of the lock-in. Substituting Eqn. (A.6) in to the total induced current response term yields the following expression:

$$\begin{aligned}\langle I(t)\rangle = Im \sum_{n_1 n_2=-\infty}^{\infty} & J_{n_1}(x_1)J_{n_1+m1}(x_1)J_{n_2}(x_2)J_{n_2+m_2}(x_2) \\ & \times \exp^{i(m_1\theta_1+m_2\theta_2)} J(n_1\omega_1 + n_2\omega_2 + V_0^{'}/\alpha)\end{aligned} \tag{A.7}$$

where $\theta_i = \omega_i t + \phi_i$.

For the direct mixing, we are only interested in current components such that, $m_1 = +1$ and $m_2 = -1$ or $m_1 = -1$ and $m_2 = +1$. The direct mixing components of the current response thus reduce to

$$\langle I(t)\rangle_{\omega_0}^{dm} = \Delta I_r^{dm} \cos(\omega_0 t + \phi_0) + \Delta I_i^{dm} \sin(\omega_0 t + \phi_0). \tag{A.8}$$

Here, $\omega_0 = \omega_2 - \omega_1$ and $\phi_0 = \phi_2 - \phi_1$. The in phase component of the direct mixing

response is given by

$$\Delta I_r^{dm} = \sum_{n_1 n_2=-\infty}^{\infty} \{J_{n_1}(x_1)J_{n_2}(x_2)[J_{n_1-1}(x_1)J_{n_2+1}(x_2) + J_{n_1+1}(x_1)J_{n_2-1}(x_2)]\ I^{'}(V_0^{'} + n_1\alpha\omega_1 + n_2\alpha\omega_2)\}. \tag{A.9}$$

For the harmonic mixing, we are only interested in current components such that $m_1 = +2$ and $m_2 = -1$ or $m_1 = -2$ and $m_2 = +1$. The direct mixing components of the current response thus reduce to

$$\langle I(t)\rangle_{\omega_0}^{hm} = \Delta I_r^{hm}\cos(\omega_0 t + \phi_0) + \Delta I_i^{hm}\sin(\omega_0 t + \phi_0) \tag{A.10}$$

where $\omega_0 = \omega_2 - 2\omega_1$ and $\phi_0 = \phi_2 - 2\phi_1$. The in phase component of the harmonic mixing response is given by

$$\Delta I_r^{hm} = \sum_{n_1 n_2=-\infty}^{\infty} \{J_{n_1}(x_1)J_{n_2}(x_2)[J_{n_1-2}(x_2)J_{n_2+1}(x_2) + J_{n_1+2}(x_1)J_{n_2-1}(x_2)]\ I^{'}(V_0^{'} + n_1\alpha\omega_1 + n_2\alpha\omega_2)\}. \tag{A.11}$$

The quadrature components ΔI_i^{dm} and ΔI_r^{hm} can easily be shown to vanish for arbitrary amplitudes V_1 and V_2, when the difference frequency ω_0 approaches zero.

A.6 Computation of $< \phi >$: Probabilities Method

Here we discuss computation of $< \phi >$ using probabilities method. If the system starts on the n-branch, and if p represents the probability that the phase has advanced from $2\pi n$ to $2\pi(n+1)$ by quantum tunneling, then the phase expectation value is given by

$$\langle\phi\rangle = 2(1-p) + 2\pi(n+1)p = 2\pi[n+p]. \tag{A.12}$$

The driving force equals the difference in energy per unit length between the potential wells at $\phi \sim 2\pi n$ and $\phi \sim 2\pi(n+1)$. When $\alpha << 1$, this is given by

$$F = 4\pi u_E \left[\theta - 2\pi\left(n + \frac{1}{2}\right)\right]. \tag{A.13}$$

Defining $\theta'_n \equiv \theta - 2\pi\left(n+\frac{1}{2}\right)$ and following refs. [22, 65] for soliton pair production or using the analogy to Schwinger pair production in a 1-D system [70] , the tunneling rate, for $\theta'_n \geq 0$, can be written as

$$\Gamma = \Gamma_0 \theta'_n \exp[-\theta_0/\theta'_n]. \tag{A.14}$$

Here $\theta_0 = \pi E_0/E_T$, $E_0 = \pi\Delta_\varphi^2/(\hbar c_0 e^*)$, Δ_φ is the soliton energy and e^* the charge (most likely $2e$) per quantum degree of freedom, and Γ_0 is proportional to the high-field CDW conductance. The time evolution dp/dt is zero for $\theta'_n < 0$ and, for $\theta_n > 0$, given by

$$dp/dt = \Gamma_0 \theta'_n \exp(-\theta_0/\theta'_n)[1-p]. \tag{A.15}$$

Finally, to simplify the computations we make the definitions: $t' \equiv t/\tau$, $f \equiv \omega\tau/2\pi$, proportional to applied current I, $q \equiv \theta/2\pi$, $q_0 \equiv \theta_0/2\pi = E_0/2E_T = E_0/E^*$, $\gamma = 2\pi\tau\Gamma_0$, $q'_n \equiv \theta'_n/2\pi = q - n - 1/2$, and $v \equiv q - p - n$ is proportional to the

voltage across the inner contacts and to the normal shunt current. This results in the coupled differential equations:

$$\begin{aligned} \frac{dq}{dt'} &= f - v, \\ \frac{dq}{dt'} &= \gamma q_n \exp(-q_0/q_n')[1-p], \qquad \text{for} \quad q_n' \geq 0, \text{ and} \\ \frac{dq}{dt'} &= 0 \qquad\qquad\qquad\qquad\quad \text{for} \quad q_n' > 0. \end{aligned}$$

The equations are numerically integrated, and n is incremented while p is reset back to zero once p exceeds a cutoff close to one (*e.g.* 0.996), representing completion of the transition from branch n to $n+1$. Figure A.13(a) shows results of such voltage

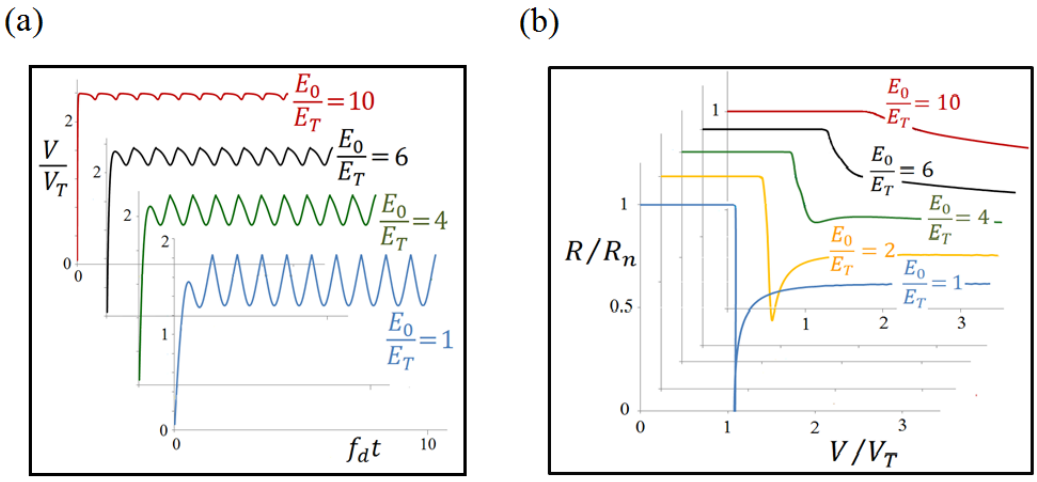

Figure A.13: (a) Computed voltage vs. time (f_d = drift or "washboard" frequency) using probabilities, showing coherent voltage oscillations for several values of $2q_0 = E_0/E_T$, where $\gamma = 4.2$ and $f = 1.2$. (b) Computed, using probabilities, differential resistance $R = dV/dI$ vs. V/V_T for several values of E_0/E_T, where E_T and V_T are the Coulomb blockade threshold field and voltage, respectively.

oscillation simulations for several values of $2q_0 = E_0/E_T$ ($\gamma = 4.2, f = 1.2$). The figure shows non-sinusoidal sawtooth behavior similar to that seen in certain CDW

systems under high magnetic fields, where the oscillation period is in the tens to hundreds of microsecond range. (We obtain forward sawtooths in the simulations when E_0/E_T is further reduced and γ and f are increased.) However, the voltage oscillations observed in $NbSe_3$ crystals, where the period is in the microsecond to sub-microsecond range, tend to be more rounded. The current-voltage characteristics are computed by averaging the voltage over several cycles in the plateau region. Figure A.13(b) shows examples of computed differential resistance dV/dI (normalized to R_n) vs. normalized voltage V/V_T for several values of E_0/E_T (for $\gamma = 4.2$). As E_0/E_T increases, the behavior evolves from that showing a sharply defined threshold and 'negative wings,' as reported for coherent, relatively pure samples of $NbSe_3$ [56]. One effect of γ is to determine the ratio of normal resistance to high-field resistance, and our studies suggest an empirical scaling law: $\frac{R_n}{R_\infty} \approx C_\gamma + 1$, where C is a constant.